Master thesis

Preparation of ultracold atomic sources towards ground state polar molecules

Supervisor: Associate Prof. Shin Inouye

February 2008

Department of applied physics, School of engineering

The University of Tokyo

66509 Kiyotaka Aikawa

Acknowledgements

First and foremost, I would like to thank my advisor Dr. Shin Inouye for allowing me various chances to learn what is important for an experimentalist and a physicist. His endless knowledge and clear way of thinking always help me to understand underlying physics. I feel very fortunate to have had the opportunity to study under such an excellent physicist.

I am also grateful to Dr. Tetsuo Kishimoto for his careful and unerring advises on experiments. Without his advises, I would have spent much more time in doing anything. I learned from him the importance of forecasting. I wish experiments at his new lab achieve significant results.

The post-docs in our lab have taught me a variety of new aspects of physics through repeated discussions. Dr. Jun Kobayashi has taught me how atoms interact with light in various situations. His intuitive explanation greatly helps my understanding. Dr. Daisuke Akamatsu has taught me the importance of interpreting every phenomenon with fundamental principles. It has been my pleasure to discuss with him about any scientific problem without any stereotype.

I also thank to the students in the lab, Kai Noda, Masahiro Hayshi, Yusuke Tanooka and Yousuke Fujikake for supporting researchl activities.

Dr. Masahito Ueda, who is the project leader of ERATO, has given me many advices and encouragements on research. I would like to be grateful for his insightful advices and also for financial supports. I also thank for Dr. Mikio Kozuma and Dr. Takashi Mukaiyama who have taught me what I could not learn from papers, that is, details and essences on various experiments. It has been my good experience to discuss with them.

Discussions with the post-docs of other groups have given me various knowledge which I would not know without them. I am grateful to Dr. Nobuyuki Takei, Dr. Makoto Takeuchi and Dr. Munekazu Horikoshi for teaching me details on their experiments. Thanks also go to the graduate students of our neighboring group, Yasuhisa Inada, Taizo Miyato and Shuta Nakajima. Talking with them has also given me insights on physics.

Finally, I would like to thank Dr. Atsushi Yamaguchi and Dr. Youichi Enomoto for advising on research and Mr. Toshihiko Sato, Ms. Minako Shioda and Ms. Ai Kouda for supporting office jobs.

Contents

Chapter 1 Introduction

1.1 Cold atoms

Since the first realization of Bose-Einstein condensation (BEC) of dilute atomic gases [1, 2, 3], atomic physics has been revealed variety of intriguing quantum behaviors of atomic gases. One of milestones among them is observation of a superfluid to a Mott insulator transition in a BEC trapped in optical lattices [4]. In their experiment, it is clearly shown that a superfluid phase appears at a small repulsive interaction regime while a Mott insulator phase appears at a large interaction regime. The observed critical point well coincides with that of theoretical prediction. The importance of their work lies in that they showed a general framework that trapped atomic gases is an ideal quantum matter to simulate a problem in condensed matter physics. In this point of view, observation of condensation of fermionic atomic pairs [5] is also remarkable. They developed a method to project fermionic atomic pairs to molecules taking advantage of Feshbach resonance. This novel technique enabled them to measure the momentum distribution of fermionic atom pairs and show condensation of fermionic atoms. Their work associated research on atomic gases with superconductivity. Now researches on fermionic atoms form a new field called BCS-BEC-crossover and are rapidly growing both in theoretical and experimental aspects.

To obtain cold atoms in a quantum degenerate regime, both laser cooling and evaporative cooling are required. Laser cooling slows atoms by using the light pressure on atoms to around 1mK while evaporative cooling eliminates only hot atoms to cool down atomic clouds below $1\,\mu$K. Both techniques have been established in the 90s and now they are routinely used in experiments.

What make experiments on atomic gases fascinating are techniques of optical lattices and Feshbach resonance: we can trap atoms in an ideal periodical potential made of light just as electrons are in condensed matters, while we can tune the strength of interaction between atoms by utilizing Feshbach resonance.

The technique of optical lattices has its origin in an old proposal [6]. The idea is simple: atoms could be confined in a standing wave by means of the dipole force arising from the light shift. It was first demonstrated in 1987 with Cs atoms [7]. However, experiments with optical lattices are not much investigated until the realization of BEC, since loading atoms to optical lattices with a high filling fraction requires a high atomic density. With quantum degenerate atomic gases, nearly unit filling fraction is easily attained. Now experiments with one dimensional and two dimensional as well as three dimensional lattices are used to study many body physics in periodic potentials.

Feshbach resonance is intuitively understood as follows: when colliding atom pairs is coupled to a molecular vibrational level by some interaction (spin-exchange interaction or magnetic dipole-dipole interaction in the case of alkali atoms), they behave as if they are virtually bounded and their scattering property varies. As is easily known from the second order perturbation theory, the change in the scattering property is most strongly affected when the atomic energy level is degenerate with the molecular level. Though Feshbach resonance was originally found in nuclear physics [8], it was theoretically predicted for atomic gases [9, 10, 11, 12, 13] and experimentally observed [14, 15, 16].

Current interest of this field mainly lies in fermionic superfluidity and ordered phase in optical lattices. Since they are too widespread to overview, here good reviews on these topics are quoted [17, 18].

1.2 Cold molecules

Cold molecules have been of great interest since they may reveal many novel physics not observable in atomic systems. For example, supersolid and checkerboard phases are predicted for the system of heteronuclear molecules trapped in optical lattices [19]. A crystal phase is predicted for cold heteronuclear molecules in a two dimensional trap [20]. Here tuning anisotropic dipole-dipole interaction between molecules with microwave

will give a novel tool to engineer strongly correlated quantum phases. An exotic chemical reaction based on bosonic stimulation is expected for the system of Bose-condensed atoms coupled to a diatomic molecular Bose gas [21]. Another possible application of cold molecules is to use their strong internal electric field to measure electron electric dipole moment (eEDM) [22]. The result is expected to help to select or justify fundamental theory of elementary particles. The application of cold molecules to quantum computation [23] is also fascinating since they are expected to enable us to perform 10^5 C-NOT gate operations simultaneously.

However, obtaining cold molecules is not straightforward. Laser cooling which is successful for atoms is not applicable to molecules due to their complicated rovibrational levels. Laser cooling requires a cycling transition which repeats absorption of cooling lasers and spontaneous emission. If you want to cool molecules with lasers, a few tens of extra repumping lasers would be necessary to avoid optical pumping to the rovibrational levels irrelevant to the cooling transition. Preparing such a large number of lasers is impractical.

Early works on cold molecules utilizes supersonic expansion to cool molecules vibrationally and rotationally [24]. In this method, a high pressures gas such as Ar with molecules undergoes a rapid adiabatic expansion from a small nozzle. During the expansion, rotational and vibrational motions of molecules are converted to translational motion of molecules. The resulting gas stream contains molecules with their rotational and vibrational temperature of around 10K [25]. Though this method is quite powerful to make absorption lines narrow in molecular spectroscopy, it is not suitable as a source for trapping molecules since it inevitably gives molecules a large translational velocity. To circumvent this problem and trap cold molecules in supersonic expansion, the Stark deceleration method is developed [26]. This method takes advantage of the fact that polar molecules strongly interact with an electric field and converts their translational velocity to the potential energy. With this method, 10^4 ND_3 molecules are successfully loaded in a electrostatic trap with a density of $10^7 cm^{-3}$ at a temperature of 1mK [27].

Another promising approach for cooling molecules is to use cryogenic technology. A helium gas cooled to around 300mK with a dilution refrigerator works as a coolant in this method. The kinetic energy of molecules is removed through elastic collisions to the coolant helium gas and their vibrational and rotational motions are quenched through inelastic collisions. So far trapping 10^8 CaH molecules with a density of $8\times10^7 cm^{-3}$ at a temperature of 400 ± 50mK had been demonstrated with this method [28].

An alternative approach to obtain cold molecules is to associate cold atoms. In this approach, laser cooled and even evaporatively cooled atoms are used as an initial source. They are associated by photoassociation or Feshbach resonance without heating. Thus it is easy to achieve a translational temperature well below 1mK with this method. Since collisions between cold atoms occur for low partial waves, the rotational temperature of formed molecules is already low. However, they are in their high vibrational levels. Though this approach is limited to molecules made of atomic species to which laser cooling is applicable, now it is regarded as the most promising way to achieve quantum degenerate molecular gases. Table 1.1 lists cold molecules obtained by association of cold atoms where PA means photoassociation and FR means Feshbach resonance. Here numbers and lifetimes of molecules are given only for trapped molecules. Note that lifetimes largely depend on density and trap depth and thus reference values are listed below.

Currently this approach has a problem that formed molecules have a short lifetime (1~100ms) and a small dipole moment (10^{-7}Debye [29]) due to their large molecular size. Efforts to transfer them to the lowest vibrational level which is expected to have a long lifetime and a large dipole moment are now under way. So far a small number of RbCs molecules are formed in their lowest vibrational level [30].

Table 1.1 Cold molecules obtained by association of cold atoms

Molecule	Method	Number	Temperature [μ K]	Lifetime [ms]	Reference
$^{133}Cs_2$	PA	NA	~300	NA	[31]
$^{23}Na^{133}Cs$	PA	NA	260±130	NA	[32, 33]
$^{39}K_2$	PA	NA	~300	NA	[34]
$^{85}Rb_2$, $^{87}Rb_2$	PA	NA	90±50	NA	[35]
$^{87}Rb_2$	PA	$\sim 10^5$	~0.10	0.10~0.45	[36]
$^{85}Rb_2$	FR	$\sim 10^3$	NA	0.1	[37]
$^{23}Na_2$	PA	NA	~500	NA	[38]
$^{6}Li_2$	FR	1.5×10^5	~0.14	10^3	[39]
$^{40}K_2$	FR	2.5×10^5	~0.15	1	[40]
$^{133}Cs_2$	FR	3×10^3	$(40\pm 3\pm 2)\times 10^{-3}$(v) $(2\pm 2\pm 3)\times 10^{-3}$ (h)	NA	[41]
$^{23}Na_2$	FR	10^5	~0.03	5	[42]
$^{39}K^{85}Rb$	PA	NA	~150	NA	[43]
$^{85}Rb^{133}Cs$	PA	NA	~100	NA	[44]
$^{133}Cs_4$	FR	10^4	0.25	NA	[45]
$^{7}Li^{133}Cs$	PA	NA	~100	NA	[46]
$^{40}K^{87}Rb$	FR	10^4	NA	20	[47]

1.3 This work

1.3.1 Our goal

We are going to produce a BEC of heteronuclear molecules in their lowest vibrational level. As explained above, association of cold atoms is a promising way for our purpose. A possible pathway to realize it is as follows: First two fermionic or bosonic atoms are cooled to quantum degeneracy with laser cooling and evaporative cooling. Then they are associated by Feshbach resonance to form loosely bound heteronuclear molecules. Finally they are transferred to the lowest vibrational level by means of stimulated Raman transition without heating.

Formation of heteronuclear molecules with Feshbach resonance has demonstrated before [47, 48]. The most uncertain process in the above procedure is what wavelength is the most suitable to transfer loosely bound molecules to the lowest vibrational level. Though Sage et al. [30] had performed the transfer process successfully, their operation is a pulsed one and therefore number of obtained molecules is limited. Thus the next important task is to demonstrate a transfer from loosely bound molecules to the lowest vibrational level with a high efficiency. Search for the optimum excited state and demonstration of the transfer process are going to be performed with molecules produced by photoassociation since formation of loosely bound molecules with photoassociation is simpler than that with Feshbach resonance. The resultant small number of molecules is detected by resonance enhanced multiphoton ionization (REMPI) which has been used for photoassociative spectroscopy as a sensitive detection tool.

Our target molecule is $^{41}K^{87}Rb$. $^{41}K^{87}Rb$ has several advantages over other alkali dimers:

1. There are many spectroscopic data on excited states. Scattering properties between ^{41}K and ^{87}Rb are also known precisely through experiments on a ^{40}K-^{87}Rb system [49, 50].

2. Preparation of ultracold atomic sources is relatively easy because the resonant laser frequencies are close to each other and both species can work with dispensers. It is also important that simultaneous condensation of

^{41}K and ^{87}Rb has already been demonstrated [51].

3. Photoassociation rate is high due to their large masses and a large van der Waals interaction between them [52].

4. Broad interspecies Feshbach resonances are predicted for the ^{41}K-^{87}Rb system [53].

1.3.2 Overview of past works on laser cooling of potassium atoms

Potassium is the last stable alkali atom to be successfully cooled and trapped in a MOT. The peculiar hyperfine structure in the excited states of bosonic potassium isotope ^{39}K and ^{41}K prevents a conventional approach for laser cooling, while extremely small natural abundance of fermionic isotope ^{40}K(~0.012%) makes it difficult to trap it. It was the first time that Williamson and Walker succeeded in a MOT of ^{39}K and ^{41}K in 1995 [54]. Cooling and trapping of ^{40}K was successfully done even later in 1998 [55].

The peculiarity of bosonic potassium isotopes lies in the relatively narrow hyperfine splitting of excited states due to their small nuclear magnetic moments. In the case of ^{39}K, the splitting between the F'=3 and F'=2 of $P_{3/2}$ manifold is 21 MHz, which is comparable to the natural linewidth of 6.2MHz, while in the case of ^{41}K the corresponding splitting is even narrower and is only 13MHz. If one employ a conventional approach for other alkali atoms which detune MOT lasers by about 20MHz to the red of F'=3, ground state F=2 atoms will experience a strong heating and optical pumping into F=1 state via excited F'=2 state of $P_{3/2}$. To avoid these effects, Williamson and Walker took a large detuning for both trapping and repumping beam. This led to a first MOT of potassium, though it required a relatively high intensity of around 500mW/cm^2. Here both trapping and repumping beam provided cooling and trapping forces and a large capture velocity of 30 m/s was obtained.

There are a few reports on further investigations on laser cooling of bosonic potassium. Wang et al. reported a dark SPOT of ^{39}K to increase the density of MOT by one order, which enabled them to observe photoassociation spectra of $^{39}K_2$ in a vapor cell [56]. Dark SPOT is originally developed for sodium [57] and then extended for ^{87}Rb [58], ^{133}Cs [59] and ^{39}K [56], but not for other species. It suppresses repulsion forces between atoms due to repeated absorption and emission of resonant photons by reducing the intensity of repumping beam at the center of the MOT. Atoms in the center of the MOT fall into F=1 dark state and do not feel any optical force. This results in an increase in density by two orders. Another approach for a high density MOT is a compressed MOT (C-MOT) which changes the condition of MOT temporally and was first reported for ^{87}Rb [60]. This method utilizes the fact that a condition for a large number of atoms and that of a high density is different: first atoms are collected in a large number condition and then compressed and cooled in another condition. A C-MOT of potassium was successfully performed by Prevedelli et al. for both ^{39}K and ^{41}K [61]. They observed significant decrease in temperature from a few mK to around 150 μ K when the detuning of both trapping and repumping light is decreased to hit around F'=0. However, the density after C-MOT remained low compared with that of other alkali species by nearly two orders. A detailed experimental and theoretical investigation on the cooling mechanism in a ^{39}K MOT is given by [62]. They performed numerical simulations of the optical Bloch equation and showed that a large detuning required to collect atoms significantly decreases a friction force at the MOT, which leads to a high temperature and a low density. They also showed that a sub-Doppler feature appears at small detuning and low intensity regime, where an attainable minimum temperature was estimated to be 20 μ K.

1.3.3 Outline of this thesis

First basics on laser cooling are presented in chapter 2.1. Interaction between a two level atom and light is discussed by means of the optical Bloch equations. Two kind of forces exerted on atoms by light are derived. Mechanism of the Doppler cooling is briefly explained by using derived formulae. An explanation on magneto-optical trapping, which is an actual implementation of the Doppler cooling, is also given here. In chapter 2.2, important topics on diatomic molecules are explained. The notion of potential energy between two atoms is given. Coupling between various angular momenta is explained. Interaction between molecules and light is reviewed. Then numerical examples are presented to clarify what theoretical calculations can predict. Here calculated potential energy curves of KLi are shown since we had been planning to produce $^{40}K^{6}Li$ molecules.

Next our experimental apparatuses are overviewed in chapter 3. Details on our laser system are given. Structure and operation of external cavity diode laser, slave laser, DFB laser and tapered amplifier are explained. Our vacuum chambers are briefly explained. Methods to estimate number, temperature and density of atoms are shown. Then principle and actual operation to detect atoms and molecules with multiphoton ionization is reviewed.

In chapter 4, our main results are presented. First, laser cooling of ^{39}K atoms are studied. More than 10^{9} atoms are trapped in a MOT. We found that number of atoms is enhanced when trapping and repumping lasers satisfy a Raman condition. Then properties of a double MOT system are investigated. Longitudinal and transverse velocities of pushed atoms are measured. We show that almost all atoms could be trapped in the 2nd MOT. Second, laser cooling of ^{41}K is studied in detail. With absorption imaging, we found that temperature of atomic cloud is quite high (~10mK) and density is low (~$10^{9}/cm^{3}$) at the Raman condition where the largest number is obtained. Even if this condition is avoided, still temperature is high and density is low. We found that time dependent MOT could overcome this difficulty. Finally phase space density of 10^{-6} is obtained after the whole laser cooling processes. Lastly, we give our latest results on detection of atoms and molecules with multiphoton ionization. A time-of-flight mass spectroscopy shows that we have certainly detected K^{+}, Rb^{+} and Rb_2^{+}. We give qualitative arguments on how atoms and molecules are ionized based on the observed signals.

Chapter 2 Theoretical background

2.1. Laser Cooling

In this section, theory of laser cooling is briefly reviewed. Only the most important topics are covered here since our purpose is not to present a thorough theory, but to provide some basic concepts which is necessary to understand the experimental results. First, basic quantum mechanical description of a two level system interacting with light is presented in 2.1.1 based on [63]. The subsequent section 2.1.2 explains the basic principle of Doppler cooling with which a laser light cools atoms down to a sub-mK temperature based on a simple model.

2.1.1 Optical force on atoms

We consider the force F exerted on atoms by light in a semiclassical approach. We assume that force on atoms is expressed as a time-derivative of the expectation value of momentum operator based on the analogy to classical mechanics:

$$\left\langle \hat{F} \right\rangle = \frac{d}{dt}\left\langle \hat{p} \right\rangle \tag{2.1}$$

According to the Ehrenfest theorem, we can rewrite this expression as

$$\left\langle \hat{F} \right\rangle = \frac{i}{\hbar}\left\langle \left[\hat{H}, \hat{p}\right] \right\rangle + \left\langle \frac{\partial \hat{p}}{\partial t} \right\rangle \tag{2.2}$$

where H is written as a sum of kinetic energy and interaction with light:

$$\hat{H} = \frac{\hat{p}^2}{2m} + \hat{H}_{light} \tag{2.3}$$

Here the second term in (2.2) vanishes since p does not depend on time. We use the usual expression on the momentum operator $\hat{p} = -i\hbar\nabla$ to modify (2.2):

$$\left\langle \hat{F} \right\rangle = \frac{i}{\hbar}\left\langle \left[\hat{H}_{light}, \hat{p}\right] \right\rangle = \left\langle \hat{H}_{light}\nabla - \nabla\hat{H}_{light} \right\rangle \tag{2.4}$$

Noting that the second term in the bracket in (2.4) means that

$$\nabla\hat{H}_{light} = \left(\nabla\hat{H}_{light}\right) + \hat{H}_{light}\nabla \tag{2.5}$$

(2.4) becomes

$$\left\langle \hat{F} \right\rangle = -\left\langle \nabla\hat{H}_{light} \right\rangle \tag{2.6}$$

which says the force exerted on atoms by light is the negative gradient of the potential made by light. If we assume that the spatial variation of electric field is sufficiently large compared to the atom, (2.6) is simplified:

$$\left\langle \hat{F} \right\rangle = -\nabla\left\langle \hat{H}_{light} \right\rangle \tag{2.7}$$

We write down the Hamiltonian of the electromagnetic field under the electric dipole approximation as

$$\hat{H}_{light} = -e\mathbf{r}\cdot\mathbf{E} \tag{2.8}$$

where $\mathbf{r}$ is the electron coordinate, e is charge of electron. $\mathbf{E}$ is electric field defined as

$$\mathbf{E} = E_0\mathbf{e}$$

where E_0 is the amplitude of light field and $\mathbf{e}$ is a unit vector containing spatial and time variation of electric field.

Here we introduce the assumption that the atom is described as a two level system. Then we can define the Rabi frequency as

$$\Omega = \frac{-eE_0}{\hbar}\left\langle \Psi_e \left| r \right| \Psi_g \right\rangle \tag{2.9}$$

where $\Psi_{g,e}$ denotes the electronic ground and excited wavefunction. In this notation, the integral on the electron coordinate in (2.7) is expressed in terms of Ω and (2.7) becomes

$$\left\langle \hat{F} \right\rangle = -\hbar\nabla\left\langle \Omega \mathrm{e}(\mathbf{r},t) \right\rangle \equiv -\hbar\nabla\left\langle \Omega' \right\rangle \tag{2.10}$$

where **r** is the atomic coordinate and $\mathrm{e} = |\mathbf{e}|$. To calculate this integral, we introduce the density matrix

$$\hat{\rho} = \left|\Psi\right\rangle\left\langle\Psi\right| \tag{2.11}$$

where the atomic wavefunction Ψ satisfies the Schrodinger equation

$$i\hbar\frac{\partial}{\partial t}\left|\Psi\right\rangle = \hat{H}\left|\Psi\right\rangle \tag{2.12}$$

Since ρ is a 2*2 matrix, we define the four components as

$$\rho = \begin{pmatrix} \rho_{gg} & \rho_{eg} \\ \rho_{ge} & \rho_{ee} \end{pmatrix} \tag{2.13}$$

Then (2.10) is written with the density matrix as

$$\left\langle \hat{F} \right\rangle = \hbar\left(\rho_{eg}^{*}\nabla\Omega' + \rho_{eg}\nabla\Omega'^{*}\right) \tag{2.14}$$

since the expectation value of an operator A is obtained with

$$\left\langle A \right\rangle = Tr\left(\rho A\right) \tag{2.15}$$

and there are no diagonal terms in (2.10). Here we used rotating wave approximation (RWA) to neglect the high frequency terms.

Next we split the derivative of Ω' into its real and imaginary part as

$$\nabla\Omega' = \left(\mathbf{q}_r + i\mathbf{q}_i\right)\Omega' \tag{2.16}$$

Then (2.14) is expressed as a sum of two terms:

$$\left\langle \hat{F} \right\rangle = \hbar\mathbf{q}_r\left(\Omega'\rho_{eg}^{*} + \Omega'^{*}\rho_{eg}\right) + i\hbar\mathbf{q}_i\left(\Omega'\rho_{eg}^{*} - \Omega'^{*}\rho_{eg}\right) \tag{2.17}$$

To express this force with frequency and intensity of light, we have to obtain the explicit form of the density matrix. The time dependence of the density matrix is derived from (2.1) as

$$i\hbar\frac{\partial}{\partial t}\hat{\rho} = i\hbar\left[\left(\frac{\partial}{\partial t}\left|\Psi\right\rangle\right)\left\langle\Psi\right| + \left(\frac{\partial}{\partial t}\left\langle\Psi\right|\right)\left|\Psi\right\rangle\right] = \hat{H}\hat{\rho} - \hat{\rho}\hat{H} = \left[\hat{H},\hat{\rho}\right] \tag{2.18}$$

where $H = H^{\dagger}$ is used. Taking account into the fact that the atom is a two level system and there is spontaneous emission with a constant rate $\Gamma/2$, we obtain the optical Bloch equations (OBE) which describes the time dependence of a two level atom interacting with light:

$$\begin{aligned}
\frac{d\rho_{gg}}{dt} &= \Gamma\rho_{ee} + \frac{i}{2}\left(\Omega^*\rho_{eg} - \Omega\rho_{ge}\right)e^{-i(\omega_l-\omega_a)t} \\
\frac{d\rho_{ee}}{dt} &= -\Gamma\rho_{ee} + \frac{i}{2}\left(\Omega\rho_{ge} - \Omega^*\rho_{eg}\right)e^{-i(\omega_l-\omega_a)t} \\
\frac{d\rho_{ge}}{dt} &= -\frac{\Gamma}{2}\rho_{ge} + \frac{i}{2}\Omega^*\left(\rho_{ee} - \rho_{gg}\right)e^{i(\omega_l-\omega_a)t} \\
\frac{d\rho_{ge}}{dt} &= -\frac{\Gamma}{2}\rho_{eg} + \frac{i}{2}\Omega\left(\rho_{gg} - \rho_{ee}\right)e^{i(\omega_l-\omega_a)t}
\end{aligned} \tag{2.19}$$

where ω_l and ω_a denotes the frequency of light and atomic resonance, respectively. If we define the population difference between the ground and excited states as

$$w = \rho_{gg} - \rho_{ee}$$

and use the optical coherence

$$\rho_{ge} = \rho_{eg}^*$$

the OBE (2.19) is simplified to a set of equations

$$\begin{aligned}
\frac{d\rho_{eg}}{dt} &= -\left(\frac{\Gamma}{2} - i\Delta\right)\rho_{eg} + \frac{iw\Omega}{2} \\
\frac{dw}{dt} &= -\Gamma w - i\left(\Omega\rho_{eg}^* - \Omega^*\rho_{eg}\right) + \Gamma
\end{aligned} \tag{2.20}$$

where $\Delta \equiv \omega_l - \omega_a$ denotes the detuning from the resonance. The steady state solutions of the OBE are obtained by setting the time derivatives of w and ρ_{eg} to zero in (2.20):

$$\begin{aligned}
w &= \frac{1}{1+s} \\
\rho_{eg} &= \frac{i\Omega}{2\left(\Gamma/2 - i\Delta\right)\left(1+s\right)}
\end{aligned} \tag{2.21}$$

where

$$s = \frac{\left|\Omega\right|^2/2}{\Delta^2 + \Gamma^2/4} \equiv \frac{s_0}{1 + \left(2\Delta/\Gamma\right)^2} \tag{2.22}$$

is the saturation parameter. Here s_0 is the on-resonance saturation parameter:

$$s_0 \equiv \frac{2\Omega^2}{\Gamma^2} = \frac{I}{I_s} \tag{2.23}$$

where I_s is the saturation intensity defined as

$$I_s \equiv \frac{\pi hc\Gamma}{3\lambda^3} \tag{2.24}$$

and depends on atomic species.

The population of the excited state is easily obtained as

$$\rho_{ee} = \frac{1-w}{2} = \frac{1}{2}\frac{I/I_s}{1+I/I_s+(2\Delta/\Gamma)^2} \tag{2.25}$$

An important expression for the scattering rate of light by atoms is obtained here. The population in the excited state decays with the rate

$$\Gamma\rho_{ee} = \frac{\Gamma}{2}\frac{I/I_s}{1+I/I_s+(2\Delta/\Gamma)^2} \tag{2.26}$$

which is equal to the excitation rate in the steady state. Thus we can see that an atom scatters photons with the rate (2.26).

Substituting (2.21) to (2.17), we obtain an explicit expression for the force exerted on atoms by light as a sum of two kinds of forces [64]:

$$\left\langle \hat{F} \right\rangle = \frac{I/I_s}{1+I/I_s+(2\Delta/\Gamma)^2}\left(-\mathbf{q}_r\hbar\Delta + \mathbf{q}_i\frac{\hbar\Gamma}{2}\right) \tag{2.27}$$

The first term is called the dipole force and the second term is called the scattering force or the dissipative force. The dipole force arises when there is a gradient in the amplitude of the electric field while the scattering force arises when there is a gradient in the phase of the electric field. The specific cases where these two forces exist are a standing wave and a traveling wave. For a traveling wave with the electric field

$$\mathbf{E}(\mathbf{r},t) = \mathbf{e}E_0\cos(\omega t - \mathbf{kr}) \tag{2.28}$$

$\mathbf{q}_{r,i}$ of (2.16) is written as

$$\mathbf{q}_r = 0, \mathbf{q}_i = \mathbf{k} \tag{2.29}$$

Here we used RWA to neglect a high frequency term. Substituting (2.29) to (2.27), only the scattering force is remaining:

$$\left\langle \hat{F} \right\rangle = \frac{\Gamma}{2}\frac{I/I_s}{1+I/I_s+(2\Delta/\Gamma)^2}\hbar\mathbf{k} \tag{2.30}$$

This expression is interpreted intuitively as momentum of an absorbed photon $\hbar\mathbf{k}$ exerts a force on atoms with the scattering rate (2.26). Since this force is dissipative, it is possible to cool atoms with it. In contrast, for a standing wave made by two counterpropagating lasers with the electric field

$$\mathbf{E}(\mathbf{r},t) = \mathbf{e}E_0\cos\mathbf{kr}\cos\omega t \tag{2.31}$$

$\mathbf{q}_{r,i}$ of (2.16) is written as

$$\mathbf{q}_r = -\mathbf{k}\tan\mathbf{kr}, \mathbf{q}_i = 0 \tag{2.32}$$

which means that only the dipole force arises in this case. Substituting (2.32) to (2.27) and taking into account the spatial modulation of I/I_s, the only remaining term is the dipole force written as

$$\left\langle \hat{F} \right\rangle = \hbar\mathbf{k}\Delta\frac{2I/I_s\sin 2\mathbf{kr}}{1+I/I_s\cos^2\mathbf{kr}+(2\Delta/\Gamma)^2} \tag{2.33}$$

This force is also exerted by momentum of a photon but here absorption from one laser and stimulated emission to the other laser occur at the same time. Thus the dipole force is conservative and can be used to trap atoms but cannot be used to cool atoms.

2.1.2 Doppler cooling

When an atom is moving with velocity v in the two counterpropagating lasers with the same intensity an the opposite polarization, they feel the scattering force of the form (2.30) from both beams independently. The forces exerted by both laser depend on the velocity of atoms due to the Doppler shift and written as

$$F_{\pm}(v) = \pm\hbar k \frac{\Gamma}{2} \frac{I/I_s}{1 + I/I_s + \left[2(\Delta \mp kv)/\Gamma\right]^2} \tag{2.34}$$

where the upper/lower sign indicate the left/right laser. The total force felt by the atom is expressed as

$$F(v) = \hbar k \frac{\Gamma I/I_s}{2} \left[\frac{1}{1 + I/I_s + \left[2(\Delta - kv)/\Gamma\right]^2} - \frac{1}{1 + I/I_s + \left[2(\Delta + kv)/\Gamma\right]^2} \right] \tag{2.35}$$

If velocity is small compared to Δ, Γ this force is approximated to be

$$F(v) \cong \frac{8\hbar k^2 \Delta I/I_s}{\Gamma\left[1 + I/I_s + (2\Delta/\Gamma)^2\right]^2} v \tag{2.36}$$

This dependence of the force on velocity means that it works as a damping force for a negative detuning. This is also confirmed from figure 2.1 which plot (2.35) against velocity. Atoms in this configuration are cooled in the lasers as if they are moving in molasses. Thus this technique is called optical molasses. However, optical molasses is effective only for atoms with small velocity. We can see from figure 2.1 that the damping force exists only for a limited velocity range:

$$|v| < \frac{\Gamma}{k} \equiv v_c \quad \text{for} \quad I/I_s \le 1, \Delta = -\Gamma/2 \tag{2.37}$$

Here we introduced a new parameter, capture velocity v_c. Only atoms with velocity smaller than v_c are cooled in the optical molasses. In most cases, v_c is ranged in 10~30m/s. This is much smaller than the velocity of room temperature atoms. Thus collecting atoms with optical molasses from room temperature gases is not efficient. Note that the capture velocity depends on the intensity and detuning: higher intensity and larger detuning lead to a larger capture velocity, though both of them makes cooling of atoms less effective due to a high photon scattering rate as explained below.

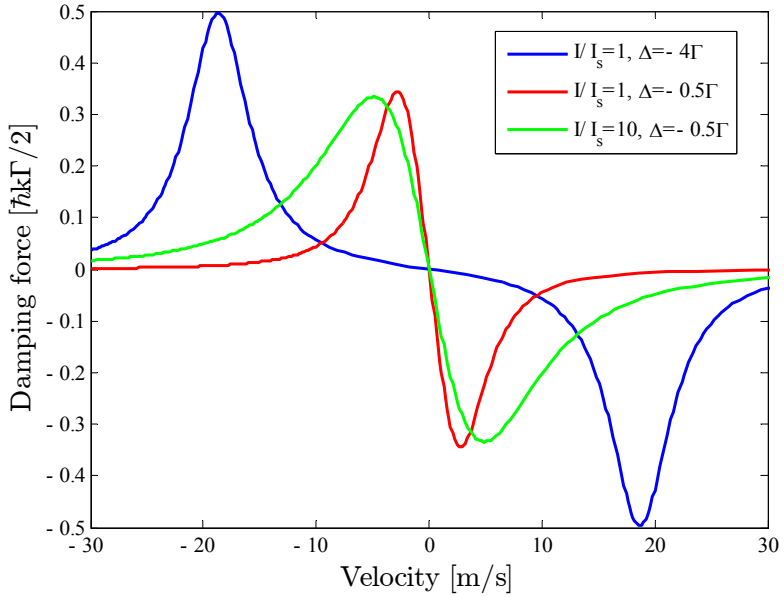

Fig.2.1 Velocity dependence of the damping force for one dimensional optical molasses.
Here $\Gamma/2\pi$ =6.09MHz and $k/2\pi$ =767nm are assumed. Theses values correspond to the case of potassium atom.

The temperature obtained in the optical molasses is, of course, not zero. There are two limitations. First, atoms cannot have a smaller energy than the energy of a photon since cooling are performed by absorption and emission of photons. Second, spontaneous emissions in random directions cause heating of atoms. The first limitation is often represented as the recoil temperature

$$T_r = \frac{\hbar^2 k^2}{k_B M} \tag{2.38}$$

where k is wavenumber of a photon, M is mass of atom and k_B is the Boltzmann constant. The recoil temperature is the lowest temperature obtained with optical transition except for a few cases such as Raman cooling. The expression for the second limitation is obtained by setting the sum of cooling and heating rate is zero at the steady state. Cooling rate is obviously

$$Fv = \frac{8\hbar k^2 \Delta I/I_s}{\Gamma\left[1 + I/I_s + (2\Delta/\Gamma)^2\right]^2} v^2 \tag{2.39}$$

while heating rate is

$$4\frac{\hbar^2 k^2}{2m}\frac{\Gamma}{2}\frac{I/I_s}{1 + I/I_s + (2\Delta/\Gamma)^2} \tag{2.40}$$

Here the first numerical factor 4 means that there are two beams and an atom is kicked twice at each scattering by absorption and emission of photons. Thus temperature at the steady state is written as

$$T = \frac{\hbar}{4}\frac{1 + I/I_s + (2\Delta/\Gamma)^2}{2|\Delta|/\Gamma} \tag{2.41}$$

We can see that high intensity and large detuning cause heating. The minimum temperature at sufficiently low intensity is obtained by setting $\Delta = -\Gamma/2$ in (2.41):

$$T_D = \frac{\hbar\Gamma}{2} \tag{2.42}$$

which is called the Doppler temperature and the lower limit obtained with the Doppler cooling.

2.1.3 Magneto optical trapping

Though optical molasses can slow atoms, it cannot confine atoms since there is no restoring force in optical molasses. It is possible to yield a restoring force by adding magnetic field gradient to the optical molasses if there are magnetic sublevels in the excited states. This configuration is called magneto optical trap (MOT) and nowadays widely used to cool and trap atoms.

The mechanism of magneto optical trap is easily understood by adding a position dependent term due to the Zeeman shift of magnetic sublevels to (2.35):

$$F(v,z) = \hbar k \frac{\Gamma I/I_s}{2}\left[\frac{1}{1 + I/I_s + \left[2(\Delta - kv + \mu' B' z/\hbar)/\Gamma\right]^2} - \frac{1}{1 + I/I_s + \left[2(\Delta + kv - \mu' B' z/\hbar)/\Gamma\right]^2}\right] \tag{2.43}$$

where B' is a magnetic field gradient at the center of magnetic field, z is distance from the center of magnetic field and $\mu' = (g_e M_e - g_g M_g)\mu_B$ is the difference of magnetic moments between ground and excited magnetic sublevels. When the Doppler and Zeeman shifts are small compared to the detuning, (2.43) is approximated to be

$$F = -\alpha z - \beta v \tag{2.44}$$

The second term contributes to cool atoms as in optical molasses, whereas the first position dependent term works as a restoring force which confines atoms to the center of the magnetic field.

Note that dependence of the restoring force on position has a similar shape to figure 2.1: there is a finite capture range in which atoms feel confining forces. This capture range is easily estimated from the capture

velocity as

$$z_c \approx \frac{\hbar k v_c}{\mu' B'} \tag{2.45}$$

which is usually ranged in 2~20mm. The radius of the MOT never exceeds the capture range. The capture range is important since it determines the trap depth of MOT through

$$W = \frac{1}{2}\alpha z_c^2 \tag{2.46}$$

which is typically around a few K. Heating processes such as fine structure changing collision easily exceed the trap depth and lead to loss of atoms. The actual size of the MOT is approximately related to the typical velocity of atoms v based on the virial theorem:

$$\frac{1}{2}\alpha z^2 = \frac{1}{2}mv^2$$

where z is the typical radius of the atomic cloud. Since density and temperature of a MOT is limited by the nature of atoms and light, these relations indicate that maximum number captured in a MOT is also limited to around the usual value 10^9~10^{10}.

In reality, MOT is performed with a three dimensional configuration shown in figure 2.2. The anti-Helmholtz coils produce a magnetic field gradient in all directions. Six laser beams are irradiated to produce three dimensional confining forces. Here all beams are circularly polarized to manipulate magnetic sublevels of excited states separately.

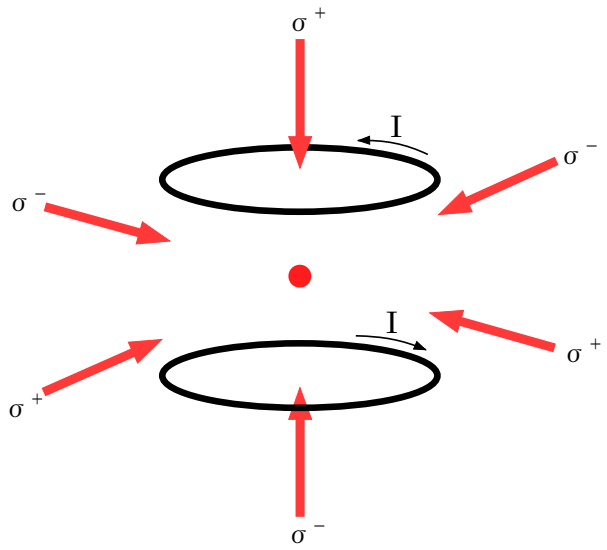

Fig.2.2 Configuration of MOT

Six circularly polarized lights are incident on the vacuum chamber. Anti-Helmholtz coils make a magnetic field gradient at the middle of two coils.

2.2 Molecules

When atoms are bonded to form a molecule, rich new natures appear which is not originally contained in the constituent atoms. Since our research goals is to form ultracold polar molecules, it is necessary to take into account these new features in our discussions. Molecular physics is also important to treat interactions between atoms in the physics of collisions between cold atoms. In this chapter, basics of molecular physics are presented

briefly. Though there are huge background works on the molecular physics, most of them are not necessarily closely related to our case. Therefore here we restrict our focus on the selected topics which are quite important to understand the behavior of *ultracold alkali diatomic molecules*.

2.2.1 Internal structure

The main difference of a molecule from an atom lies in its internal structure: vibration and rotation. These motions are based on the fact that interaction between its constituent atoms are not strong enough to constraint them completely; if it is, there will be no novel behaviors compared to an atom. A moderate interaction between atoms enables molecules to have a wide variety of observable behaviors. For example, molecules can transit from one rovibrational state to another rovibrational state by collisions or emission of microwave without any change in the electronic configuration. There are of course many excited states as in the case of atoms, which are accessible with optical transitions.

To dealing with these behaviors simply, we adopt Born-Oppenheimer approximation: the motions of electrons in a molecule is fast enough to neglect the motion of the molecule itself. This is usually a good approximation for cold atoms and molecules. However, Born-Oppenheimer breakdown (BOB) effects become the problem in the case of a light atom. This consists of the next two factors: the isotopic difference in the electronic potential energy and non-adiabatic coupling of electronic motion to nuclear motion [65, and references therein]. Though the latter could be neglected for cold atoms and molecules since it is proportional to a rotational energy, the former might become a problem for light atoms even in the case of cold atoms and molecules: for example, the isotopic difference in the potential depth of the order of $0.1\mathrm{cm}^{-1}$ is reported for Li_2 [66]. For heavy atoms with mass number of A, the isotopic difference is expected to scale as A^{-2} and thus negligible.

Most of the molecular properties are explained with the potential energy between its constituent atoms which is expressed as a function of the interatomic distance. An example of the calculated potential energy curve (PEC) for the alkali dimer KLi is shown in figure 2.3. Labeling to these states are performed as follows. First the ground state is labeled X. The states with the same spin multiplicity as X is labeled in alphabetical order with capital letters from the energetically lowest state except X to higher states. The states with the different spin multiplicity from X are labeled in alphabetical order with lower case letters from the energetically lowest state to higher states. These alphabetical labeling is followed by a Greek alphabet indicating the projection of the orbital angular momentum to the interatomic axis. Σ, Π and Δ corresponds to L=0, 1 and 2, respectively. A superior figure between the two letters denotes the spin multiplicity: 1 means singlet, while 3 means triplet. It is noteworthy that another letter g or u is added after the Greek letters to indicate the symmetry of the state in the case of a homonuclear molecule. Though this type of labeling is easily comprehensible, there is another type of labeling where the first alphabet is replaced by the number in parentheses which indicate the order of the state in the same symmetry and spin multiplicity.

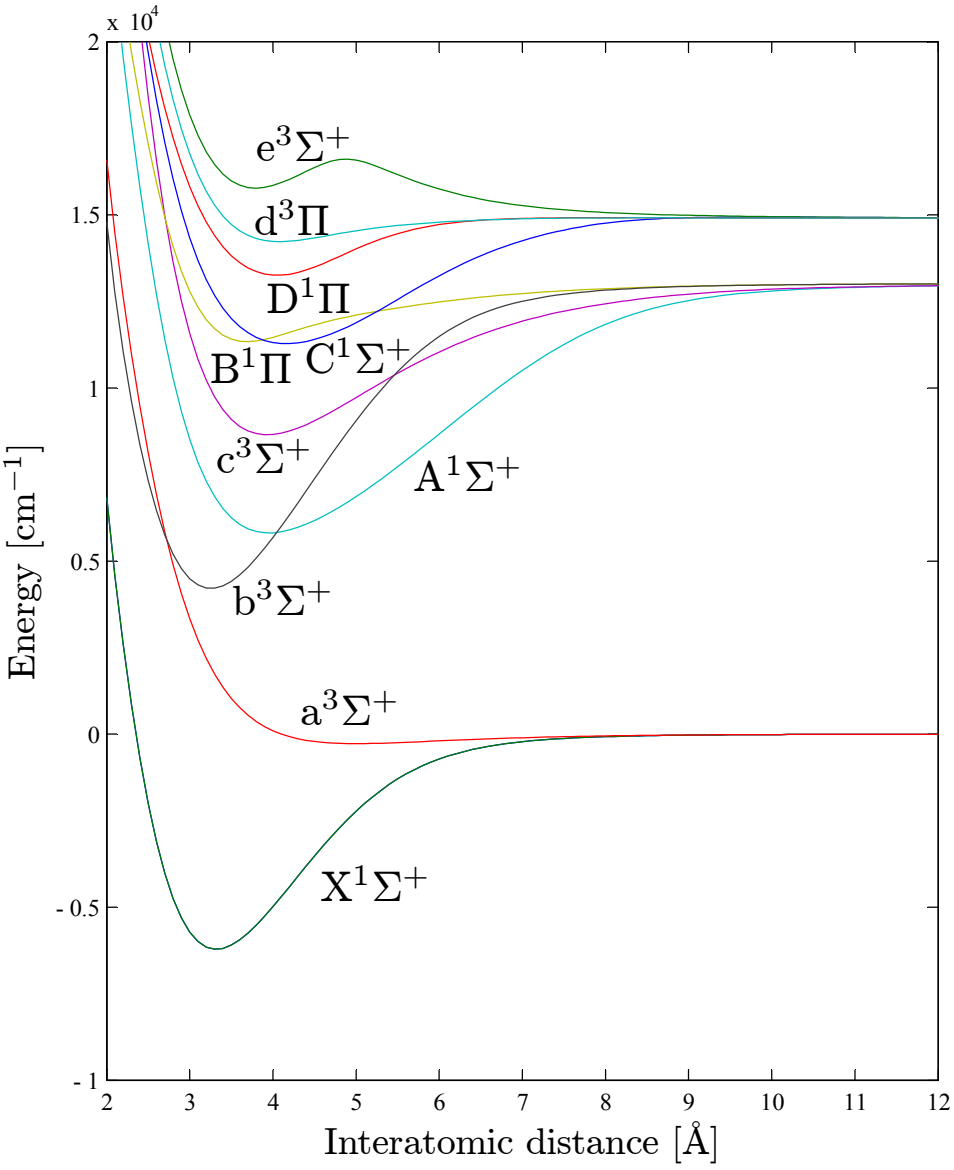

Fig.2.3 Potential energy curve of KLi calculated with MOLPRO

As is easily known from the analogy to the harmonic oscillator, there are many bound states in this potential. Classically we can interpret these states as follows. When two atoms in the particular state of the molecule become close to each other, they feel a large repulsive force due to the overlap of electrons in the atoms and their motion is slowed. Finally they are reflected at the distance where their energy is equal to the potential energy. The same motion occurs when their distance becomes large, because the van der Waals force between two atoms becomes small at a large interatomic distance. Thus two atoms in a particular bound state are oscillating in the region determined by their energy and the PEC. This is a vibrational motion of molecule. Actually we can consider it quantum mechanically. The motion is described by a corresponding wavefunction as the probability distribution over the internuclear distance. We cannot observe two atoms located in a particular distance without using a very fast optical process which can resolve the motion of electrons.

There is another motion in a molecule: rotation. It is quite easy to understand classically since it is only rotating against an axis vertical to the interatomic axis. However, the rotational motion is also interpreted

quantum mechanically as a bound state of the combined potential of the centrifugal term and the electronic potential energy term. In practice we can consider the rotational levels as attached to each vibrational level, since the level spacing between rotational levels is much smaller than that of vibrational levels. The vibrational spacing is smaller for heavier molecules, which is easily understood as follows: If we assume that the potential is approximated to be a harmonic oscillator near the bottom and written as

$$V(x) = \frac{1}{2}kx^2$$

Then the vibrational level spacing is described as

$$\hbar\sqrt{\frac{k}{\mu}}$$

where μ is the reduced mass of constituent atoms.

In the case of room temperature molecule, there is a thermal distribution over rovibrational levels. Most of the molecules are in the lowest vibrational state of the potential well except for a heavy molecule which has a small vibrational level spacing, whereas most of the molecules are in the high rotational level since a rotational level spacing is much smaller than the thermal energy of the room temperature. It is noteworthy that a particular rotational state of rotational angular momentum J has multiplicity 2J+1. This leads to a thermal distribution

$$(2J+1)\exp\left(-\frac{BJ(J+1)}{k_B T}\right)$$

which has a peak around

$$J = \sqrt{\frac{k_B T}{2B}} - \frac{1}{2}$$

where B is a rotational constant and defined as

$$B = \frac{\hbar^2}{2\mu}\left\langle \Psi(R)\left|\frac{1}{R^2}\right|\Psi(R)\right\rangle$$

A thermal distribution over vibrational levels obeys the usual Maxwell-Boltzmann distribution and thus has a peak at the lowest energy level.

You can see several examples on how the PEC is useful. The depth of the ground state potential represents the stability of chemical bonding between two atoms. If it is much higher than the thermal energy of a particular temperature, then the molecule is stable under the temperature. The size of the room temperature molecule is easily estimated by reading the equilibrium distance where the potential is minimum. Information on the excited states enables us to predict which states are accessible from the ground state molecule and what is the wavelength of that transition.

Here the analytic form of the potential energy is reviewed. The origin of the potential energy between two atoms is usually explained as follows. For a small interatomic distance, overlapped electrons of atoms yield a large repulsive force, while there is an attractive force for a long interatomic distance due to dipole-dipole interaction caused by an instantaneous polarization in the electrons of atoms. However, there is a large force in a real molecule: spin exchange interaction caused by the electronic spins of atoms. The necessity that the electronic wavefunction must be antisymmetric under exchange of electrons lower the energy of the singlet states and higher that of the triplet states. This interaction exists whenever both two constituent atoms have electronic spins. Thus the analytical representation of the PEC is generally written as

$$V(R) = -\frac{C_{n_1}}{R^{n_1}} - \frac{C_{n_2}}{R^{n_2}} - \frac{C_{n_3}}{R^{n_3}} \pm AR^a \exp(-bR)$$

where R denotes the interatomic distance. The upper/lower sign refers to triplet/singlet potentials.

The first three terms account for the van der Waals interaction at long range and the repulsion at short range, while the fourth term represents the exchange interaction of the outermost electrons. It is easily known that the sum of singlet and triplet potentials represents the van der Waals interaction, while their difference indicates the exchange interaction. The integer values n_i (i=1,2,3) depend on the state of two atoms. In the case of ground state alkali dimers, n_1=6, n_2=8 and n_3=10. The r-dependency of the van der Waals terms is readily comprehensive: the terms with C_6, C_8 and C_{10} represents dipole-dipole, dipole-quadrupole and quadrupole-quadrupole interaction between two atoms, respectively. The accurate values of the dispersion coefficients have been obtained by ab initio calculations [67, 68, 69, 70, 71, 72, 73, 74], which are usually used without any modification. The derivation of the above mentioned analytical form of the exchange interaction is given in [75]. They showed that the values of a and b are written using the ionization energy of constituent atoms, I1 and I2, as

$$a = \frac{2}{\sqrt{2I_1}} + \frac{2}{\sqrt{2I_2}} - \frac{1}{2(I_1 + I_2)} - 1$$

$$b = \sqrt{2I_1} + \sqrt{2I_2}$$

The value of A in the above expression is usually obtained by fitting the above function to an experimental results to assure accuracy, though an analytical expression and calculated values are reported for several alkali dimers [75, 76]. The above expression of the exchange interaction well coincides with experimentally attained potentials for various alkali dimers [77].

Note that the above expression is accurate near the dissociation limit of the potential. Thus it gives accurate results for the calculations of a long rage molecule, but not for a deeply bound molecule. If you have to deal with a deeply bound state theoretically, it is necessary to fit the experimentally obtained potential to a complicated function. Several accurate analytic functions have been developed, part of which is shown here [78]:

1. Generalized Morse Oscillator (GMO)

$$V_{GMO}(R) = D_e\left[1 - e^{-\beta_{\mathrm{GMO}}(R)(R - R_e)}\right]^2$$

$$\beta_{\mathrm{GMO}}(R) = \beta_0^{\mathrm{GMO}} + \beta_1^{\mathrm{GMO}}(R - R_e) + \beta_2^{\mathrm{GMO}}(R - R_e)^2 + \cdots$$

2. Extended Morse Oscillator (EMO)

$$V_{\mathrm{EMO}}(R) = D_e\left[1 - e^{-\beta_{\mathrm{EMO}}(z)(R - R_e)}\right]^2$$

$$\beta_{\mathrm{EMO}}(z) = \beta_0^{\mathrm{EMO}} + \beta_1^{\mathrm{EMO}} z + \beta_2^{\mathrm{EMO}} z^2 + \cdots$$

3. Modified Lennard-Jones Oscillator (MLJ)

$$V_{\mathrm{MLJ}}(R) = D_e\left[1 - \left(\frac{R_e}{R}\right)^n e^{-\beta_{\mathrm{MLJ}}(z)z}\right]^2$$

$$\beta_{\mathrm{MLJ}}(R) = \beta_0^{\mathrm{MLJ}} + \beta_1^{\mathrm{MLJ}} z + \beta_2^{\mathrm{MLJ}} z^2 + \cdots$$

where $z \equiv (R - R_e)/(R + R_e)$.

It is important to recognize that all ‘analytic’ forms given here are not obtained by theoretical calculation but

solely by fitting to the experimental results for the calculations of molecular properties such as transition strength. In most cases, fitting procedure should be carried out with great care to reproduce experimental results correctly changing the parameters one by one.

Next we would like to see details on experimentally obtainable potentials. As you can see from the previous discussion, we cannot directly measure the potential energy itself since the wavefunction of a molecule in a particular state has a form of the probability distribution over the interatomic distance. What we can observe are only the energy levels of bound states in the potential. Thus a conversion process is required to acquire the PEC from experimental results.

Now the most widely used procedure for this purpose is Rydberg-Klein-Rees (RKR) method [79, 80, 81, 82]. Based on a first order semiclassical approximation, it derives two key equations from the vibrational energy levels $G(v)$ and rotational constants $B(v)$

$$R_2(v) - R_1(v) = \frac{2}{\beta}\int_{v_{\min}}^{v} \frac{dv'}{\sqrt{G(v) - G(v')}} \equiv 2f$$

$$\frac{1}{R_1(v)} - \frac{1}{R_2(v)} = \frac{1}{2\pi\beta}\int_{v_{\min}}^{v} \frac{B(v')dv'}{\sqrt{G(v) - G(v')}} \equiv 2g$$

Here R_1 and R_2 denote the inner and outer classical turning points and v represents vibrational quantum number in the semiclassical approach. β is a numerical constant. These two equations give the expression for R_1 and R_2 as

$$R_1(v) = \sqrt{f^2 + f/g} - f$$

$$R_2(v) = \sqrt{f^2 + f/g} + f$$

Repeating this procedure for observed vibrational levels yields a potential energy function against the interatomic distance. Now a reliable program package RKR1 is available for the whole calculations presented above [83].

Tthere are two different methods to express experimentally obtained energy levels: Dunham Expansions and Near Dissociation Expansions (NDE's). Based on the behavior of harmonic oscillator and rigid rotor, Dunham expansions expresses the vibrational energy levels $G(v)$ and the rotational constants $B(v)$ as

$$G(v) = \sum_{l=1} Y_{l,0}(v+1/2)^l = \omega_e(v+1/2) - \omega_e x_e(v+1/2)^2 + \omega_e y_e(v+1/2)^3 + \cdots$$

$$B(v) = \sum_{l=1} Y_{l,1}(v+1/2)^l = B_e - \alpha_e(v+1/2) + \gamma_e(v+1/2)^2 + \cdots$$

The coefficients $Y_{l,m}$ are used for the above calculations in RKR1.

NDE's are based on the theoretically known behavior of simple inverse-power potential

$$V(R) = D_e - \frac{C_n}{R^n}$$

where the integer value n depends on the problem and C_n is the dispersion coefficient which is already mentioned above. It was proved [84, 85] that the vibrational levels and rotational constants in this form of potential are expressed as

$$G(v) = D_e - K_0(v)$$

$$B(v) = K_1(v)$$

$$K_m(v) = \overline{X}_m(n)\left[\mu^n C_n^2\right]^{1/2-n}(v_D - v)^{2n/n-2-2m}$$

where v_D denotes the non-integer effective vibrational number at dissociation and $\overline{X}_m(n)$ is a known numerical constant depending on the physical constants and *n*. This type of representation of the energy levels near the dissociation is particularly useful for dealing with the problem of cold atoms and molecules since all parameters except effective vibrational number v_D is known from theoretical calculations and thus analysis of spectra in this region is easily carried out with (2.2).

The use of Dunham expansion is appropriate near the potential minimum, while NDE's should be used near the dissociation limit. In the code RKR1, both types of calculation are available.

Though the RKR method gives an accurate potential enough to estimate most of the molecular properties correctly, the vibrational energy levels calculated from the RKR potential typically differs from the original experimental values by around 0.1cm^{-1} due to the semiclassical approximation mentioned above. To obtain a more accurate potential, an Inverse Perturbation Analysis (IPA) approach was developed [86]. Its basic idea is as follows.

Consider the Schrodinger equation

$$\left[-\frac{\hbar^2}{2\mu}\nabla^2 + V(R)\right]\psi_n = E_n\psi_n$$

where μ is the reduced mass, V is the unknown real potential and En is an experimentally obtained eigenenergy. On the other hand, the inaccurate approximate potential V_0 gives a different eigenenergy En0 according to the corresponding Schrodinger equation

$$\left[-\frac{\hbar^2}{2\mu}\nabla^2 + V^0(R)\right]\psi_n^0 = E_n^0\psi_n^0$$

The difference in eigenenergy $\Delta E_n = E_n - E_n^0$ is due to the difference in the potential $\Delta V(R) = V(R) - V^0(R)$. A first order perturbation theory enables us to equate

$$\Delta E_n = \left\langle \psi_n^0 \middle| \Delta V(R) \middle| \psi_n^0 \right\rangle$$

If you expand the difference potential $\Delta V(R)$ in a set of appropriate basis functions $g_i(R)$, the equation becomes

$$\Delta E_n = \sum_i c_i \left\langle \psi_n^0 \middle| g_i(R) \middle| \psi_n^0 \right\rangle$$

This set of linear equations for the unknown expansion coefficients c_i is solved to construct a new potential and the whole procedure is repeated until the convergence criteria is satisfied. In this approach the RKR potential is usually used as a first approximate potential and gives an improvement of the accuracy by one order.

The RKR and IPA potential are sufficiently accurate for many purposes, but they are usually available only for limited states and only in the energy range near the potential minimum. The reason is obvious: they are obtained with spectroscopy on the ground state molecules, which means that we can know the potential with the levels accessible from the ground state molecules with optical transitions.

For the first estimate of the shape and depth of the potential for every state and in every energy range, it is

useful to utilize the results of *ab initio* calculations. It gives purely numerical solutions of the Schrodinger (or Dirac) equation of many electron systems. Since ab initio calculation of molecular potentials which is often called computer chemistry itself is a tremendous research field, here we do not give a detailed description of it. A numerical example for KLi molecule calculated with the program package MOLPRO [87] is presented later in the section 2.2.4 with experimental and past works. In most cases, the potential obtained with ab initio calculation differs from experimental results by 20 to 200 cm^{-1} depending on the calculation method and the atomic basis functions.

2.2.2 Angular momenta in a molecule

In a real molecule, many kinds of angular momenta are coupled with each other in various ways depending on the energy scale of each angular momentum. There are four important angular momenta in a molecule: electronic orbital angular momentum, rotational angular momentum, electronic spin and nuclear spin. Coupling between them makes the observed spectra complicated. For correct understanding of the experimental results, it is necessary to recognize which angular momenta are strongly coupled and which angular momenta are nearly uncoupled in the current problem. Here the coupling schemes based on the Hund's classification are given. There are five coupling cases, (a) to (e), but the important ones are (a) and (c) in the case of cold atoms and molecules. in most cases.

Hund's case (a) is the most frequently encountered case in molecular physics. Here the energy of electronic interaction mentioned in the section 2.2.1 is the largest and then spin-orbit interaction and rotational energy follows. Hyperfine interaction due to nuclear spins is omitted here since it is much smaller than other angular momenta. If you deal with a deeply bound molecule, then it corresponds to the case (a). The energy scale of each term is of the order of $1000cm^{-1}$, $100cm^{-1}$ and $0.1cm^{-1}$, respectively. In this case, states are labeled with orbital angular momentum and spin multiplicity as mentioned in the section 2.2.1.

Hund's case (c) is a relatively rare case compared to case (a), but important in the treatment of cold atoms and molecules. Here the energy of spin-orbit interaction is the largest and that of electronic interaction and hyperfine interaction follows. Rotational angular momentum is neglected here. The molecule in an excited state formed by photoassociation corresponds to the case (c). In this case, the energy scale of each term is of the order of $100cm^{-1}$, $10cm^{-1}$ and $0.1cm^{-1}$, respectively. Rotational energy in case (c) is much smaller than in case (a) because the size of the molecule near dissociation limit is large. The labeling of states is performed with Ω which denotes the projection of the sum of orbital angular momentum and electronic spin to the molecular axis.

Both of the two coupling schemes are illustrated in figure 2.4. Transition from case (a) molecule to case (c) molecule occurs around the internuclear distance of 20 Å as shown in figure 2.5. More detailed discussions on the various coupling schemes between angular momenta are found in [88].

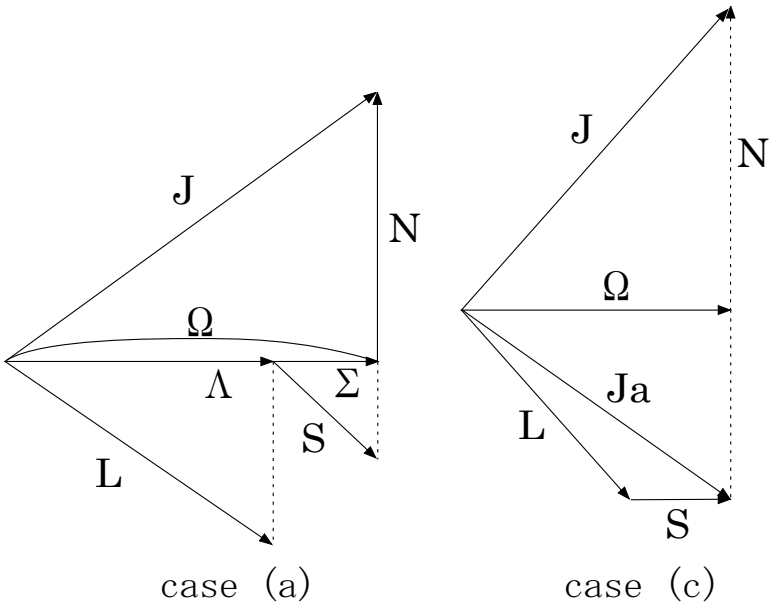

Fig.2.4 Coupling of angular momenta in case (a) and case (c)

L is orbital angular momentum, S is spin, J is total angular momentum and N is rotational angular momentum. Λ and Σ are projection of L and S to molecular axis, respectively. Ω is a sum of Λ and Σ.

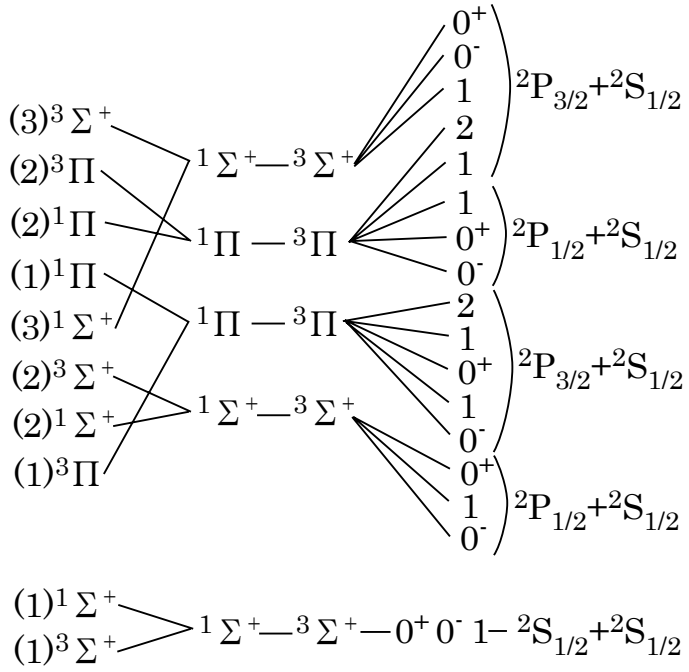

Fig.2.5 Transition between case (a) and case (c) for alkali dimmers

Interatomic distance increases from left to right. As internuclear distance increases, the electronic binding energy becomes smaller and spin-orbit interaction dominates.

Here we would like to see a particularly useful example of coupling between orbital, spin and rotational angular momenta: loosely bound alkali diatomic molecules of excited states dissociating to S+P limit. This situation frequently becomes problem in the experiments on cold atoms and molecules since atoms are excited to these states by photoassociation. The molecular Hamiltonian for this problem is described here based on the arguments in [89]. We do not argue detailed derivations on it and omit hyperfine interaction for simplicity.

Molecular Hamiltonian in the excited states without hyperfine interaction is written as

$$H = H_K + H_V(R) + H_{rot}(R)$$

where each term represents kinetic energy, potential energy including spin-orbit interaction and rotational energy, respectively. We have to obtain the specific form of H_V and H_{rot} to solve the problem. We take the basis in case (a) for writing these Hamiltonians for convenience. Then H_V is written in a block diagonal form where each block corresponds to Ω=0,1,2 as follows:

$$H_V^{\Omega=0^+}(R) = \begin{matrix} {}^1\Sigma_0^+ \\ {}^3\Pi_0 \end{matrix} \begin{pmatrix} V_{^1\Sigma}(R) & -\sqrt{2}\Delta_2(R) \\ -\sqrt{2}\Delta_2(R) & V_{^3\Pi}(R) - \Delta_1(R) \end{pmatrix}$$

$$H_V^{\Omega=0^-}(R) = \begin{matrix} {}^3\Sigma_0^+ \\ {}^3\Pi_0 \end{matrix} \begin{pmatrix} V_{^3\Sigma}(R) & \sqrt{2}\Delta_3(R) \\ \sqrt{2}\Delta_3(R) & V_{^3\Pi}(R) - \Delta_1(R) \end{pmatrix}$$

$$H_V^{|\Omega|=1}(R) = \begin{matrix} {}^3\Sigma_0^+ \\ {}^1\Pi \\ {}^3\Pi_1 \end{matrix} \begin{pmatrix} V_{^3\Sigma}(R) & \Delta_3(R) & \Delta_3(R) \\ \Delta_3(R) & V_{^1\Pi}(R) & -\Delta_3(R) \\ \Delta_3(R) & -\Delta_3(R) & V_{^3\Pi}(R) \end{pmatrix}$$

$$H_V^{|\Omega|=2}(R) = V_{^3\Pi}(R) + \Delta_1(R)$$

where V denotes case (a) potential energy and Δ_i denotes a spin-orbit interaction function.

The rotational part is written as

$$\frac{H_{rot}(R)}{B(R)} = \begin{pmatrix} x+2 & 0 & 0 & -2\sqrt{x} & 0 & 0 & 0 \\ 0 & x+4 & 2\sqrt{2} & 0 & -2\sqrt{x} & -2\sqrt{x} & 0 \\ 0 & 2\sqrt{2} & x+2 & 0 & \pm\sqrt{2x} & -\sqrt{2x} & 0 \\ -2\sqrt{x} & 0 & 0 & x & 0 & 0 & 0 \\ 0 & -2\sqrt{x} & \pm\sqrt{2x} & 0 & x+2 & 2 & -\sqrt{2(x-2)} \\ 0 & -2\sqrt{x} & -\sqrt{2x} & 0 & 2 & x+2 & -\sqrt{2(x-2)} \\ 0 & 0 & 0 & 0 & -\sqrt{2(x-2)} & -\sqrt{2(x-2)} & x-2 \end{pmatrix}$$

where $x = J(J+1)$ and J denotes the total angular momentum. The upper/lower sign indicates *e*/*f* parity levels (*e* and *f* parity means that total parity is equal to $(-1)^J$ and $(-1)^{J+1}$, respectively). Here ${}^1\Sigma^+$ appears only for *e* parity while ${}^3\Sigma_0^+$ appears only for *f* parity.

There are three notable points in this Hamiltonian:

1. The problem is a coupled channel Schrodinger equation. Though originally it became problem in the theory of atomic structure [90], now it appears in various fields of atomic, molecular and nuclear physics. In our case, it is well-known that the theory of cold collisions includes this type of Hamiltonian in general. To solve it, a special care should be taken as presented later in the section 2.2.4.
2. Spin-orbit interaction depends on the interatomic distance. For a large interatomic distance, it should be asymptotically equal to the atomic fine structure constant. However, recent works have been elucidated that it has a significant dip at a small interatomic distance due to the reduced fraction of the excited P state in the molecular wavefunction [91, 92, 93, 89, 94, 95, 96, 97, 98]. This behavior is also confirmed for KLi in the ab initio calculation with MOLPRO which is shown later in the section 2.2.4.
3. Rotational angular momentum mixes blocks with different Ω. The Hamiltonian associates two channels for J=0 while five channels for J=1 and six channels for J>1.

More detailed discussions on the coupling between angular momenta are found in [99].

2.2.3 Interactions with light

Manipulation of molecules is in most cases performed with light. In our case, molecules are formed by a photoassociation laser from atoms and detected by photoionization with an intense pulse laser. Analysis of experimentally obtained spectra needs the knowledge on which transition is involved in the specific case. Thus it is important to know how molecules interact with light. In this section, the most important topics related to the optical transitions in a molecule are given.

First we see the selection rules for various cases. An optical transition occurs in the limited cases due to restrictions on the angular momentum: it can be interpreted as a composition of the angular momenta of a molecule and light. Here we focus only on electric dipole transitions since other transitions such as electric quadrupole or magnetic dipole transitions are relatively small. There is a general rule for the quantum number J of the total angular momentum

$$\Delta J = 0,\pm 1 \quad \text{with the restriction that} \quad J = 0 \leftrightarrow J = 0 \quad \text{is forbidden}$$

In addition, there are restrictions on the symmetry of molecule:

$$+ \leftrightarrow - \quad \text{is allowed but} \quad + \leftrightarrow +, - \leftrightarrow - \quad \text{are forbidden}$$

where +/- means that the sign of the total molecular wavefunction is changed/unchanged against spatial inversion. For homonuclear molecules, an additional rule holds:

$$g \leftrightarrow u \quad \text{is allowed but} \quad g \leftrightarrow g, u \leftrightarrow u \quad \text{are forbidden}$$

Apart from these rules there are several rules which depend on how angular momenta are coupled in a molecule, that is, case (a) or (c). In case (a), the quantum number Λ should satisfy

$$\Delta\Lambda = 0,\pm 1$$

which means that Σ-Σ, Σ-Π transitions are allowed but transitions such as Σ-Δ are forbidden. Another restriction comes from the electronic spin component:

$$\Delta\Sigma = 0$$

which says singlet-singlet and triple-triplet transitions are allowed but singlet-triplet transitions are forbidden.

In case (c), there is a restriction for Ω as

$$\Delta\Omega = 0,\pm 1$$

and also a rule for Ω=0 states

$$0^+ \leftrightarrow 0^+, 0^- \leftrightarrow 0^- \quad \text{are allowed but} \quad 0^+ \leftrightarrow 0^- \quad \text{is forbidden}$$

holds. More detailed arguments on these topics are found in [88].

Note that the above rules for each case do not hold exactly in a real molecule since there are usually small perturbation effects such as spin-orbit interaction in case (a) or rotation in case (c). Thus some of transitions forbidden in case (a) or (c) are allowed in a real molecule. This fact enables us to convert a singlet molecule to a triplet molecule or vice versa with optical transitions via mixed excited states.

Though the above arguments on selection rules result from the angular parts of molecular wavefunction, there is a kind of selection rule for the radial parts of the wavefunction. The rule is based on the Franck-Condon principle, which says the electronic transition caused by light is so fast that the distance between two atoms does not change during the transition. Then we can describe a selection rule for the radial parts of wavefunction as follows: a transition occurs only when ground and excited state molecule has nearly the same size. In the quantum mechanical language, this rule is interpreted as follows: there should be a significant overlap between ground and excited wavefunctions for the transition to occur. The rule is readily confirmed by considering the transition dipole moment of the corresponding transition with quantum mechanics. Here the transition dipole moments involve all electrons in the molecule. We can write the total electric dipole in the molecule as a sum of dipole induced by electrons and nuclei

$$\vec{\mu} = \sum_s e_s \mathbf{r}_s \tag{2.47}$$

where e_s and $\mathbf{r}_s$ indicates the charge and position of electrons and nuclei, respectively. The total wavefunctions for both ground and excited states are written as products of electronic wavefunction and rovibrational molecular wavefunction under the Born-Oppenheimer approximation

$$\Psi_{tot}^{g,e}(\mathbf{r}) = \psi_{el}^{g,e}(\mathbf{r};R)\psi_{mol}^{g,e}(\mathbf{R})$$

where $R = |\mathbf{R}|$ and **r** and **R** denotes electronic and molecular coordinate, respectively. Here the Born-Oppenheimer approximation corresponds to the approximation introduced above which says electronic transition is fast enough to neglect atomic motions. Note that the electronic wavefunction depends only on the interatomic separation in the case of diatomic molecule. Taking account the expression of the dipole moment (2.47), the transition dipole moment between ground and excited molecular states is expressed as

$$\mathbf{d} = \left\langle \Psi_{tot}^{e} \left| \vec{\mu} \right| \Psi_{tot}^{g} \right\rangle = \left\langle \Psi_{mol}^{e}(\mathbf{R}) \left| \left\langle \psi_{el}^{e}(\mathbf{r};R) \left| \sum_s e_s \mathbf{r}_s \right| \psi_{el}^{g}(\mathbf{r};R) \right\rangle \right| \Psi_{mol}^{g}(\mathbf{R}) \right\rangle \tag{2.48}$$

Here we define the transition dipole moment at a particular molecular coordinate **R** as

$$\mathbf{M}(R) = \left\langle \psi_{el}^{e}(\mathbf{r};R) \left| \sum_s e_s \mathbf{r}_s \right| \psi_{el}^{g}(\mathbf{r};R) \right\rangle$$

Then we can rewrite (2.48) in a simple form:

$$\mathbf{d} = \left\langle \Psi_{mol}^{e}(\mathbf{R}) \left| \mathbf{M}(\mathbf{R}) \right| \Psi_{mol}^{g}(\mathbf{R}) \right\rangle$$

It is noteworthy that **M**(**R**) can be written as a product of radial and angular part

$$\mathbf{M}(\mathbf{R}) = M(R)\mathbf{e}(\theta,\varphi)$$

where **e** is a unit vector and determined by the relation between orientation of molecule and polarization of light. $M(R)$ is not a measurable value but obtained from theoretical calculations as shown later in the section 2.2.4. Thus we can see that a transition rate between the ground and excited molecular states is proportional to the product of radial and angular part

$$|\mathbf{d}|^2 = \left| \left\langle \Psi_{mol}^{e}(R) \left| M(R) \right| \Psi_{mol}^{g}(R) \right\rangle \right|^2 \left| \left\langle \Psi_{mol}^{e}(\theta,\varphi) \left| \mathbf{e}(\theta,\varphi) \right| \Psi_{mol}^{g}(\theta,\varphi) \right\rangle \right|^2 \tag{2.49}$$

If we assume that $M(R)$ does not depend on **R** significantly and its typical value is M_0, we can write the integral in (2.49) in a simpler form:

$$|\mathbf{d}|^2 = M_0^2 \left| \left\langle \Psi_{mol}^{e}(R) \left| \Psi_{mol}^{g}(R) \right\rangle \right|^2 \left| \left\langle \Psi_{mol}^{e}(\theta,\varphi) \left| \mathbf{e}(\theta,\varphi) \right| \Psi_{mol}^{g}(\theta,\varphi) \right\rangle \right|^2$$

The factor

$$\left| \left\langle \Psi_{mol}^{e}(R) \left| \Psi_{mol}^{g}(R) \right\rangle \right|^2$$

is called the Franck-Condon factor and represents an overlap between ground and excited molecular states. As is clear from the above expression, the Franck-Condon factor does not contain any information on the electronic structure of atoms and reflects only the radial size of ground and excited molecule. Note that selection rules on the angular parts mentioned above are included in the transition dipole moment: M_0 has a finite value only for an allowed transition.

In the end we can formulate the selection rule for the radial parts as follows: a transition occurs when the Franck-Condon factor is close to unity. However, any transition with small but non-zero Franck-Condon factor is possible in reality just as in the case of the selection rules for the angular part. In most cases, there are many transitions between ground and excited rovibrational levels.

Though knowledge on the Franck-Condon factor is quite useful to estimate transition strength, calculation of the Franck-Condon factor is not so straightforward. Now an established program package LEVEL to calculate the Franck-Condon factors as well as vibrational levels is available [100]. An example of calculated Franck-Condon factors for various transitions is presented later in the section 2.2.4.

2.2.4 Numerical investigations

In this section, molecular properties mentioned above are numerically calculated for a specific case. First we see an example of *ab initio* calculation of the PEC of KLi molecule. Calculated potentials are compared with experimental results to show accuracy of the calculations. Next variation of transition dipole moments against interatomic distance is investigated for KLi. In the end, we studied an optimum transition to convert molecules in a high vibrational level of the ground X state into the lowest vibrational level of the X state for $^{41}K^{87}Rb$.

In figure 2.6 calculated PECs of KLi already given in figure 2.3 are shown with experimentally obtained potentials. We can see that calculations are in good agreement with experiments. However, there is always a finite difference between them due to approximations made in the calculations to reduce computational tasks. The deviations of the present calculations from experiments are explicitly plotted against energy levels in figure 2.7. Here bound states are calculated with LEVEL [101]. The deviations of the present calculations are ranged in $\pm 20 cm^{-1}$. This value is reasonable compared to other published works and regarded as the limit of the current calculation method.

To see the accuracy of the present work from another point of view, the Franck-Condon factors between the calculated excited state energy levels and the experimental ground state energy level are compared in figure 2.8. Though there are deviations, they are in good agreement with each other. Since the Franck-Condon factors reflect the transition strength, this kind of calculations is very useful to interpret experimental results. Our conclusion is that experiments are necessary to know exact energy levels but calculations are quite useful for analysis of the observed spectra.

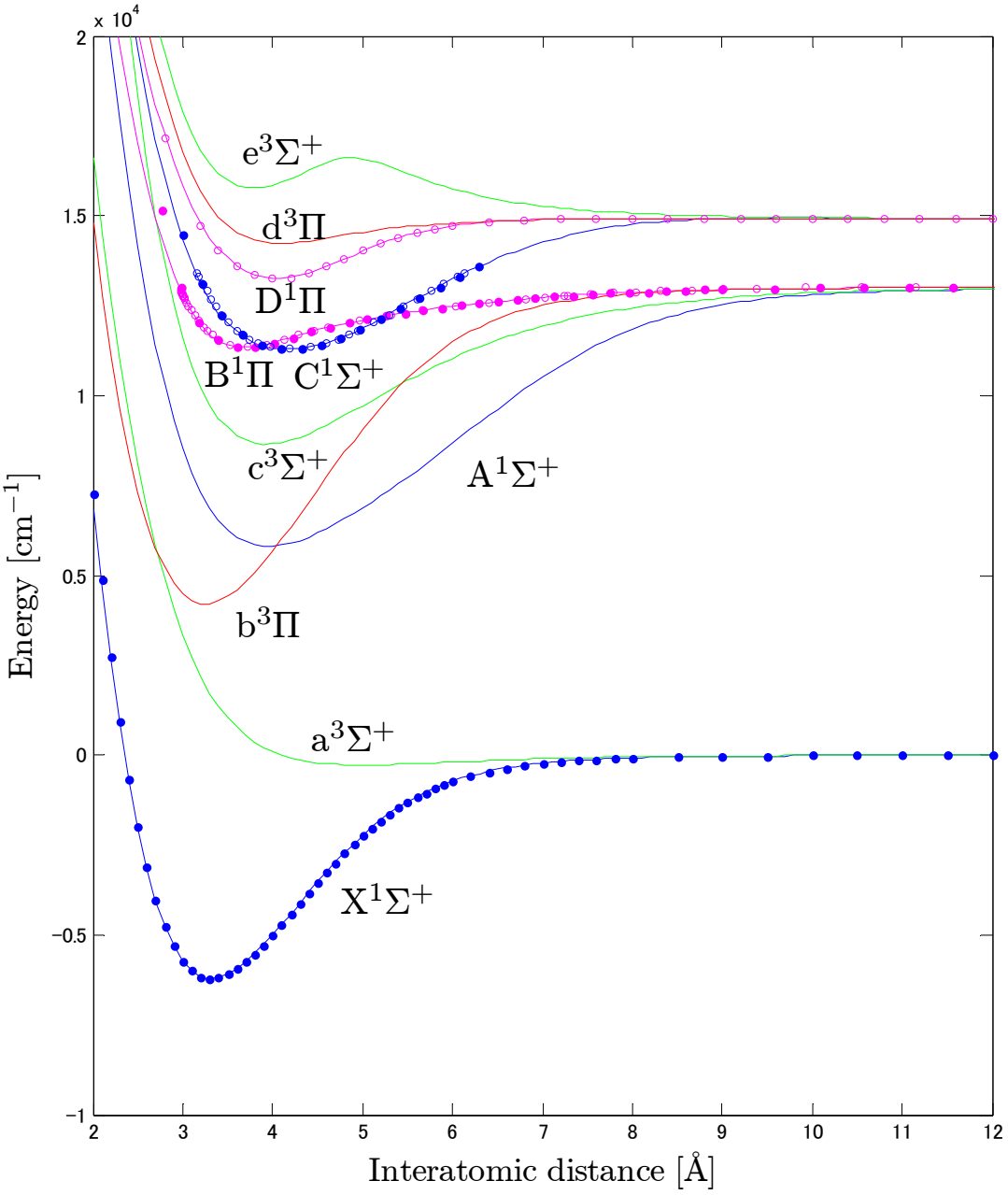

Fig.2.6 PEC of KLi

Blue, green, purple and red lines indicate $^1\Sigma^+$, $^3\Sigma^+$, $^1\Pi$ and $^3\Pi$, respectively. Solid circles are RKR data, while open circles are IPA data. The references of the presented experimental data are following: X [102], B IPA [103], B RKR [104], C IPA [103], C RKR [104], D IPA [105].

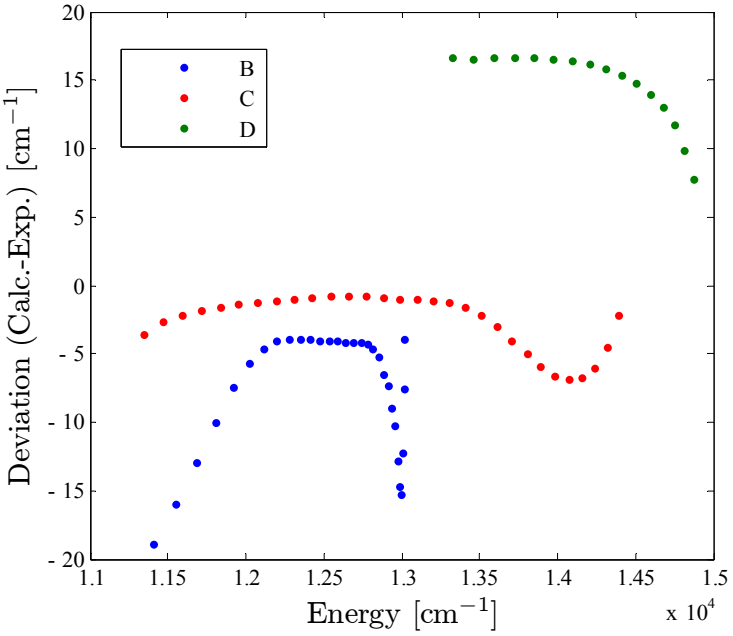

Fig.2.7 Deviations of calculated levels from experimentally obtained levels
Each point indicates a bound state. Here atomic masses are assumed to be 40u for K and 6u for Li where u is the atomic mass unit.

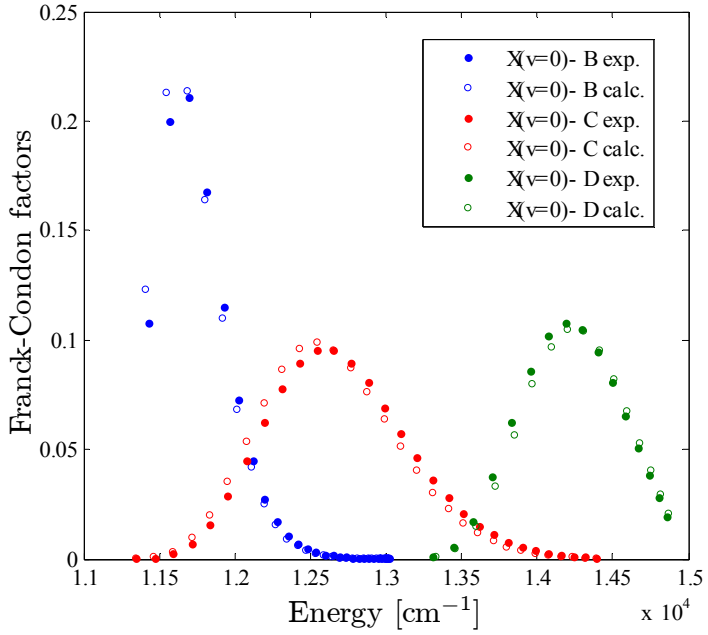

Fig.2.8 Franck-Condon factors between ground state (experiments) and excited state (calculations)
Here atomic masses are again assumed to be 40u for K and 6u for Li.

Next we investigated variations of transition dipole moments against interatomic distance for KLi molecule. The expectation values of the corresponding operator are calculated with the molecular wavefunctions obtained in the previous calculations on the potential energy. Figure 2.9 shows dependence of transition dipole moments.

For sufficiently large interatomic distance, the transition dipole moments well coincides with the corresponding atomic transition dipole moments. This means that transitions between loosely bound molecules can be treated with atomic transition dipole moments. However, transition between molecules with an interatomic distance smaller than 10Å is no more than approximated to be an atomic dipole moment.

Note that spin-orbit interactions are not taken into account in this calculation. In actual cases, spin-orbit interactions mix case (a) sates and thus transition dipole moments show a more complicated variation against interatomic distance [29].

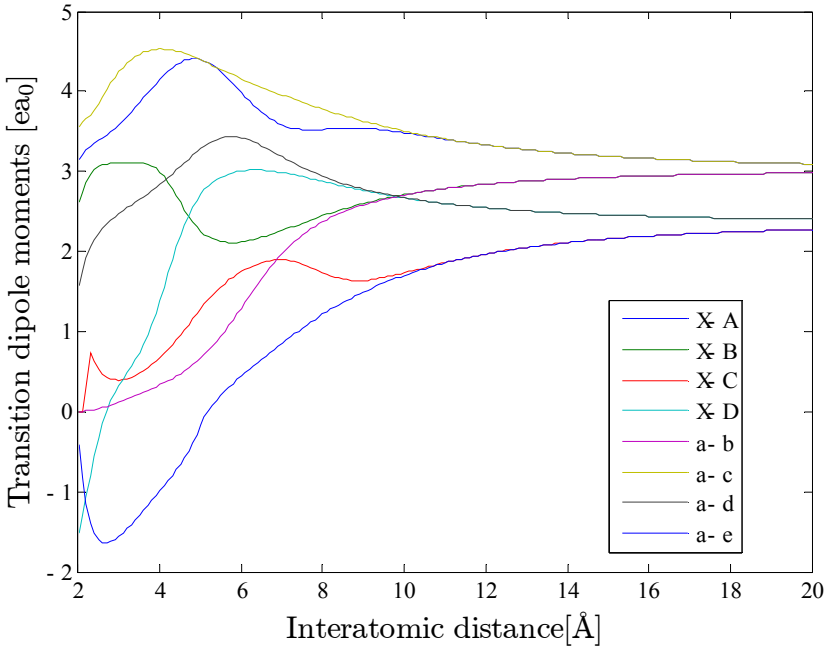

Fig.2.9 Calculated transition dipole moments of KLi
A, B, b and c states are dissociating to K(4P)+Li(2S) limit while C, D, d and e states are dissociating to K(4s)+Li(2P) limit. Here atomic transition dipole moments are $2.92ea_0$ for K(4P) and $2.35ea_0$ for Li(2P).

In the end, we give a consideration on the optimum transition to carry out a stimulated Raman transition for $^{41}K^{87}Rb$. Our goal is to form molecules in the lowest vibrational states (v=0) from loosely bound singlet molecules.

The most important point in a transfer between two molecular states is that the pump and dump should have nearly the same Rabi frequency. If the transition dipole moments for pump and dump transitions are nearly the same, the intensity needed for an efficient transfer between two ground states are also expected to be the same. However, if one of the two transitions has quite a small transition dipole moment, the intensity for that weak transition should be fairly large. This leads to unwanted excitations to closely lying excited sates and reduces the overall transfer efficiency. Note that the effective Rabi frequency for the overall transition is a product of the two Rabi frequencies but increasing the intensity of the strong transition also leads to unwanted excitations. Thus the transition dipole moments between the excited levels and the two vibrational levels in the ground states should be large.

As a first approximation, we can consider that the transition dipole moments are proportional to the Franck-Condon factors as mentioned above. Thus we can estimate the transition strength with the Franck Condon factors. For precise estimations, we have to take into account variation of the transition dipole moments against interatomic distance. Based on these arguments, we can find out the optimum transition where both pump and dump transitions have large Franck-Condon factors. Figure 2.10 shows calculated Franck-Condon factors between the vibrational levels of X state and four singlet excited states A, B, C and D.

It is clear that the C state is the most suitable for our purpose since crossing between blue and other dots occurs at comparatively large Franck-Condon factors. If we select v=90 molecules (green dots) as a starting point, the optimum transition is found to be 868nm for pump and 637nm for dump. With this transition, the

Franck-Condo factor of 0.01 for pump and that of 0.015 for dump is expected.

We note that the following two points:

1. In this argument, singlet-triplet mixing due to spin-orbit interaction is neglected. This effect is expected to be large for KRb since Rb has a large spin-orbit interaction and vibrational level spacing is small. If the mixing effect between excited singlet and triplet states is taken into account, it is possible to convert triplet molecules to singlet molecules. There is a possibility that triplet molecule is more suitable for a starting point as proposed in [106] and demonstrated for RbCs [30].
2. The loosely bound molecule with a binding energy of 0.01cm^{-1} (v=100) has fairly small Franck-Condon factors. Even when the X-C transition is used, the Franck-Condon factor at the optimum transition is around 10^{-5} which is much smaller than that of v=90 molecules. This case is particularly important since molecules formed by Feshbach resonance have typically a similar binding energy. Though we do not know whether the Franck-Condon factor of 10^{-5} is sufficient to achieve a high transfer efficiency, transfer of Feshbach molecules to the lowest vibrational level might require two or three steps.

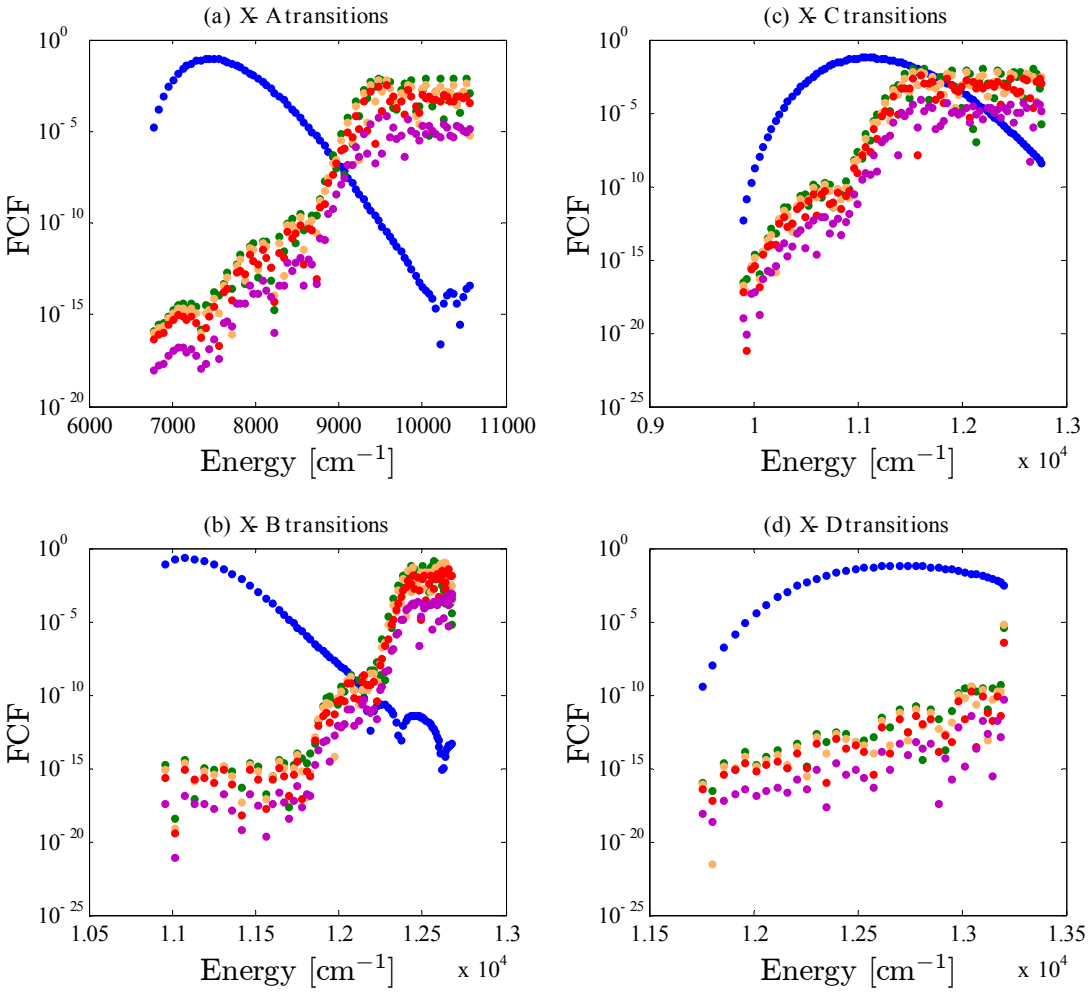

Fig.2.10 Calculated Franck-Condon factors (FCF) of KRb singlet transitions

The Franck Condon factors between the vibrational levels in the ground X states and various excited states are plotted against energy levels of the excited states. Here ab initio Potentials from [107] are used. Blue, green, orange, red and purple indicate v=0, 90, 92, 95 and 100, respectively. Formation of the v=0 molecule is our goal while the loosely bound v=90~100 molecules are expected to be formed by photoassociation. Here v=90, 92, 95 and 100 molecules are bounded by 17.12, 9.10, 2.54 and 0.01cm^{-1}, respectively.

Chapter 3 Experimental methods

Experiments on cold atoms and molecules need a large amount of apparatus. Most of the time is spent to make them and set them up. In this chapter, details on apparatuses used in our experiments are described. First, we see our laser system to manipulate potassium and rubidium atoms. Then the design and operation of vacuum chamber system is overviewed. In 3.3, a computer control system realized with a LabView program developed by Dr. T.Mukaiyama is shown.

3.1 Laser system

Here a whole laser system used in our experiments is presented. A home made external cavity diode laser (ECDL) locked to an atomic D2 line is used as a frequency stabilized light source. A portion of this master laser (~0.5mW) injects slave lasers and is amplified by around 20 times. Then a tapered amplifier (TA) amplifies the slave laser to obtain a high power around 0.6W.

3.1.1 ECDL

ECDL is a low cost tunable narrow band laser source and is widely used for experiments on atomic physics. It utilizes the fact that a semiconductor laser has a wide gain spectrum and therefore its oscillation wavelength is determined only by the length of cavity. Usually the front facet of a semiconductor laser has a reflectivity of about 3% while the back facet has nearly unit reflectivity, and thus these two facets are making up a cavity to oscillate in a single frequency. A part of photons in the cavity is emitted from the front facet. However, if you put another mirror in front of the front facet, the oscillation frequency is determined by the length of cavity made of a new mirror and the back facet when the reflectivity of the mirror is higher than that of the original facet. Thus it becomes possible to tune the oscillation frequency to the atomic absorption line by adjusting the position of the external mirror with a piezo electric actuator.

This is the basic principle of ECDL, but it does not suffice for the use of atomic experiments as the linewidth of a usual semiconductor laser (a few GHz) is much broader than the natural linewidth of atoms (typically a few MHz). It is necessary to select the oscillation wavelength. For that purpose, usually a grating is used as an external mirror: a diffracted light is feed backed to the laser diode, whereas a reflected light is used for experiments. Selection of wavelength is realized with the fact that the diffraction angle depends on wavelength. By adjusting the angle of the grating, the wavelength of feed backed light can be tuned, which means that oscillation wavelength can also be tuned. Tuning of wavelength is also possible by adjusting the position of the grating since it means that the cavity length is changed. For more detailed information on these topics, there are good reviews [108, 109].

In general, there are two types of ECDL: Littrow configuration and Littman configuration. Schematics of these two configurations are shown in Fig.3.1. The main difference lies in the output power and the linewidth. In Littrow configuration, the feed backed light is diffracted one time. This leads to a high output power and broad linewidth. In contrast, the feed backed light is diffracted two times and thus the output power is low and the linewidth tends to be narrow in Littman configuration. However, a linewidth of 1MHz is easily obtained in both configurations. In our case, a high power is required to trap many atoms. Thus we have decided to make ECDL in a Littrow configuration.

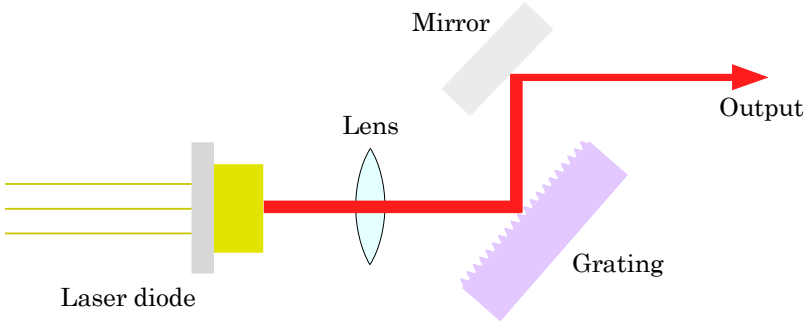

(a) Littrow configuration

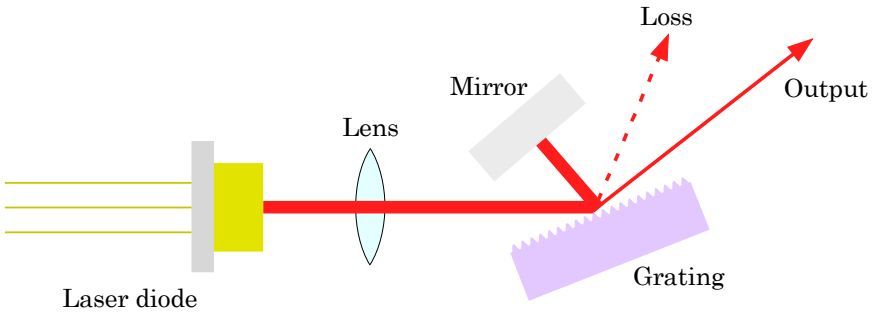

(b) Littman configuration

Fig3.1 Littrow and Littman configuration

In the Littrow configuration, the diffracted light is directly feed backed to the laser diode. In contrast, in the Littman configuration the diffracted light is reflected at a mirror and then again diffracted at the grating and return to the laser diode. Since a part of power is lost in the Littman configuration, the output power of the Littman configuration is lower than that of the Littrow configuration.

Schematics of our ECDL are shown in figure 3.2, which is a slightly modified version of [110]. A mirror is added after the grating to compensate the change in the grating angle. With this modification, an optical path after ECDL remains unchanged if the grating angle is changed. In this type of ECDL, the diffraction angle is used as a rough tuning knob, while the position of the grating works as a fine tuning knob.

Our standard grating for near-infrared light is a gold coated 1800 lines/mm holographic grating for UV range. Here we employ a grating for UV light to suppress the diffraction efficiency and obtain high output power. The diffraction efficiency at the grating is 3 or 5% for a S polarized light which depends on the direction of the grating, though it is much higher (more than 20%) for a P polarized light.

We use an antireflection coated laser diode to suppress reflection at the front facet of the laser diode and ensures stable operation, though it seems to have a difficulty that its lifetime is limited (1~1.5 year) compared with an ordinary laser diode. The temperature control of laser diode is inevitable to obtain stable operation as the length of laser diode and the gain characteristics depends on the temperature. In our design, the temperature of the whole mirror mount including a laser diode is stabilized with a peltier module under the mirror mount. We use a commercial thermo electric controller (TEC) and laser diode current controller.

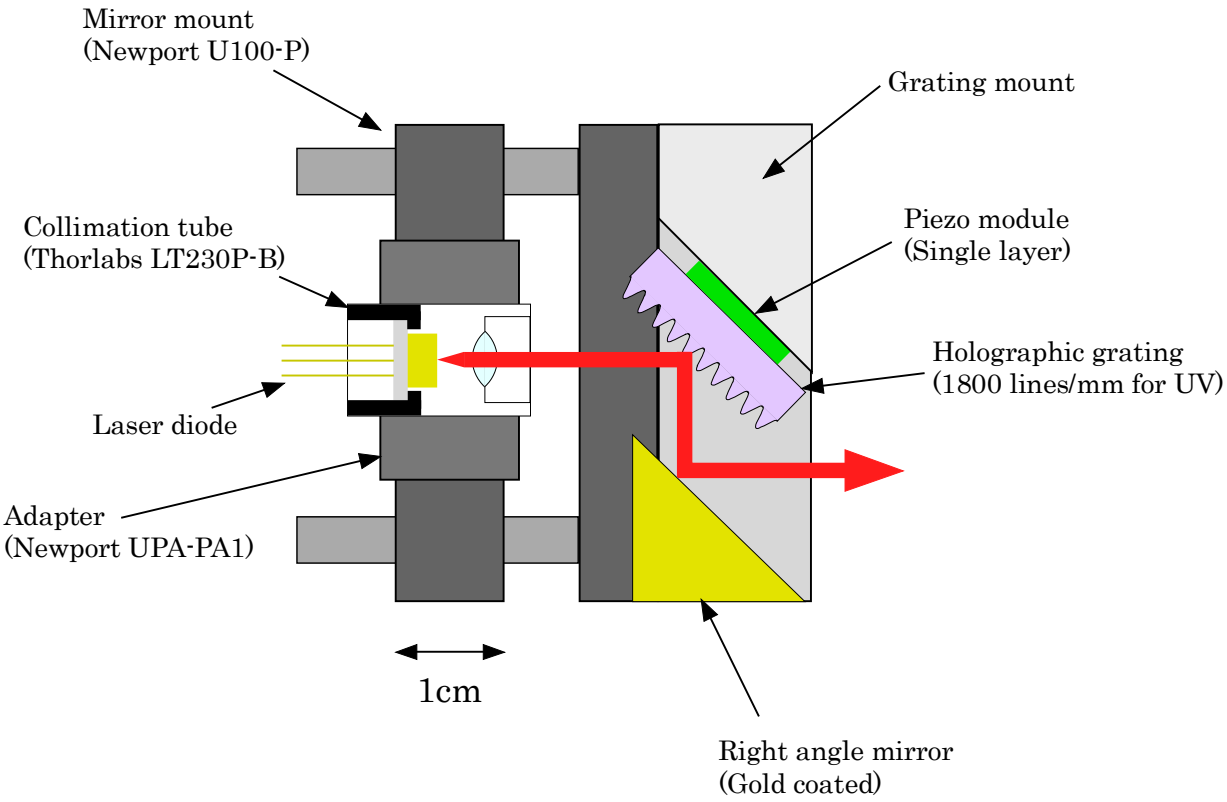

Fig.3.2 (a) Design of our ECDL

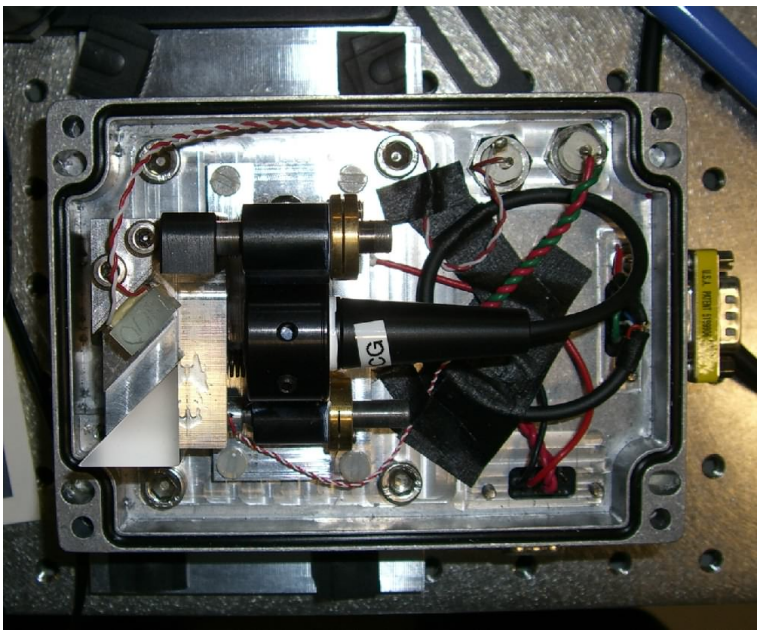

Fig.3.2 (b) Image of our ECDL

The black package is a commercial laser diode socket which contains a protection circuit (Thorlabs SR9B).

The procedure to tune this ECDL is as follows.

First the temperature should be set to a correct value: if the center wavelength of the laser diode at room temperature is different from the wavelength you want by a few nm or more, the temperature of the laser diode should be changed such that the center wavelength lies within 1 nm from the value you want. Usually the center wavelength shifts about +0.2nm per Kelvin.

Then the current to the laser diode is set to a value at which you want to use, which is recommended to be smaller than an operation current (not max current) stated on the data sheet of the laser diode to have a longer lifetime.

After these preparations the mirror mount angle is adjusted so that diffracted light goes back to the laser diode. If you put a white paper with a pin hole just in front of the laser diode, the diffracted light which passed through the pin hole will be seen on the paper near the pin hole. You have only to adjust the mirror mount so that this diffracted light is incident on the pin hole. The pin hole should be placed at the center of the light emitted from laser diode. Putting away the paper, the power after the grating will be much higher than the original spontaneous emission if the diffracted light is correctly feed backed to the laser diode.

Next the wavelength is tuned within a few GHz from what you want by adjusting the horizontal angle of mirror mount monitoring it with a wavemeter. It is usually impossible to match the wavelength to exact value you want in this stage because the mirror mount is very sensitive.

At this stage the vertical angle of the mirror mount is adjusted so that operation should be stable. This is carried out by lowering the threshold current as much as you can. When the power is monitored on an oscilloscope and the current is modulated near the threshold current, you can see the threshold current where the power begins to rise. By adjusting the vertical angle, you can obtain the lowest threshold current. This ensures that the laser oscillation is the most stable at this wavelength.

The last stage is to set the wavelength to an exact value you want with adjusting the voltage applied to the piezo electric module behind the grating.

The mode hop free range of this ECDL is around 5GHz. Its linewidth averaged for about 1s is 1MHz, which is estimated with the width of the beat note of two independent ECDL. The linewidth is probably limited by mechanical vibration of mirror mount and fluctuation in the refractive index of air in the cavity due to convection.

3.1.2 Slave laser

Since the role of a slave laser is only to amplify the master ECDL, it has a very simple structure as shown in figure 3.3. The collimation tube containing a laser diode and a collimation lens is mounted on a aluminum jig whose temperature is stabilized with a inexpensive home made TEC. Usually laser diode used in a slave laser is the same as that of maser ECDL.

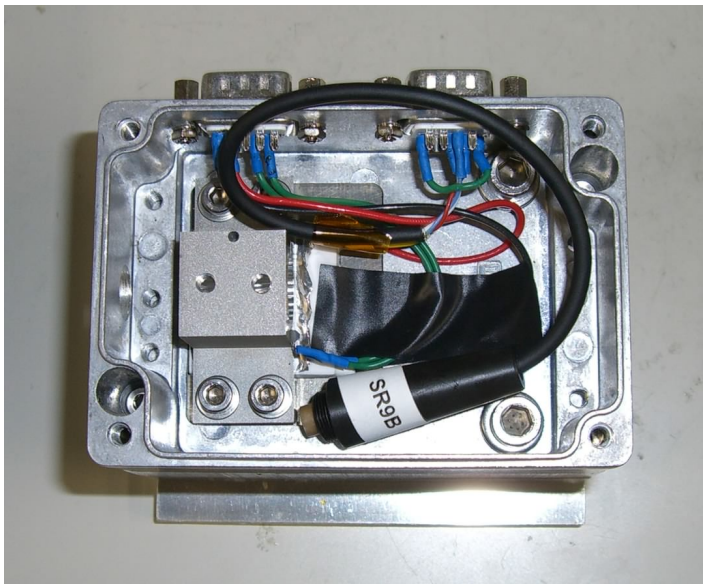

Fig.3.3 Image of our slave laser (top view)

Injection locking to a slave laser is carried out in the configuration shown in figure 3.4. When a part of master ECDL light is incident on the slave laser diode, it induces stimulated emission and the original seed light is amplified. The gain depends on the current. A faraday rotator is necessary to separate the seed light and the amplified light; otherwise the amplified light will only go back to the maser laser.

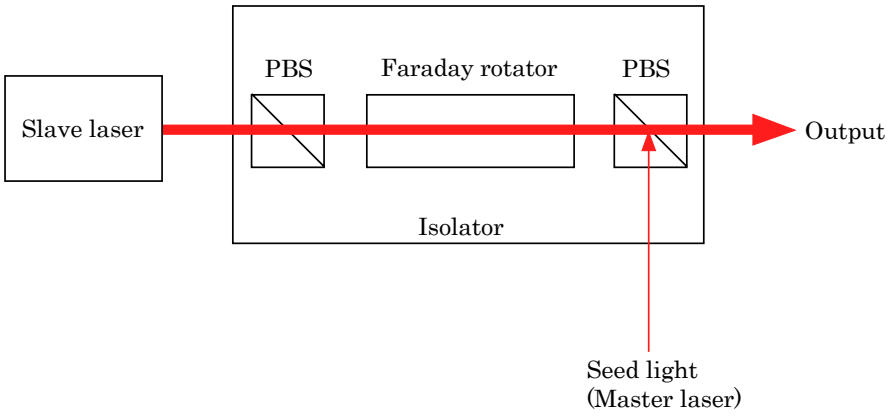

Fig.3.4 Injection locking
The seed light which originates from a master laser is amplified at the slave laser.

Although operation of a slave laser is very simple, there is a problem always you have to note. The output power is expected to increase as you raise the current, but actually there is a bad point where the output power abruptly decrease as shown in figure 3.5. At around this current, the oscillation of the slave laser is unstable and amplified spontaneous emission (ASE) increases. Thus you have to pay attention to the relation between current and power whenever you start up the laser: sometimes the power may *increase* as you *decrease* the current, which means that the output light contains undesirable ASE.

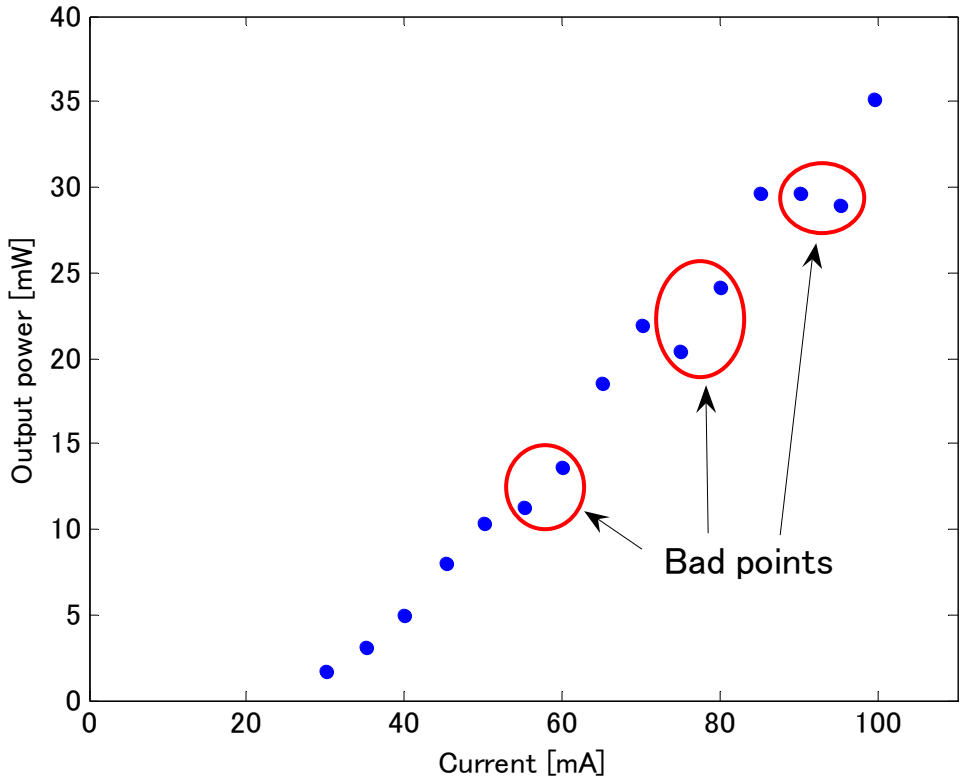

Fig.3.5 Output power of slave laser against current

3.1.3 Tapered amplifier

Tapered amplifier is another kind of semiconductor laser. The main difference from an ordinary laser diode lies in its tapered structure and both facets are antireflection coated. This enables us to obtain high power around 1W from the front facet when a seed light is incident on the back facet. In the case of an ordinary single mode laser diode, maximum attainable power is limited by the fact that high optical power more than 300mW breaks down the front facet.

The role of a tapered amplifier is also to amplify the seed light as a slave laser does, but a situation is quite different: the heat released from a slave laser diode is less than 0.2W, whereas that from a tapered amplifier usually exceeds 3W. Thus you have to take care of the released heat to be transferred effectively to some heat sink. We usually buy only a tapered amplifier chip and mount it on a home made jig made of copper. Figure 3.6 shows our design of a mount for a tapered amplifier devised by Dr. T.Kishimoto. In this design, collimation lenses are fixed to the copper heat sink which is cooled by a peltier module under the heat sink. The whole of these parts are placed in a box to avoid dusts attaching to the tapered amplifier chip.

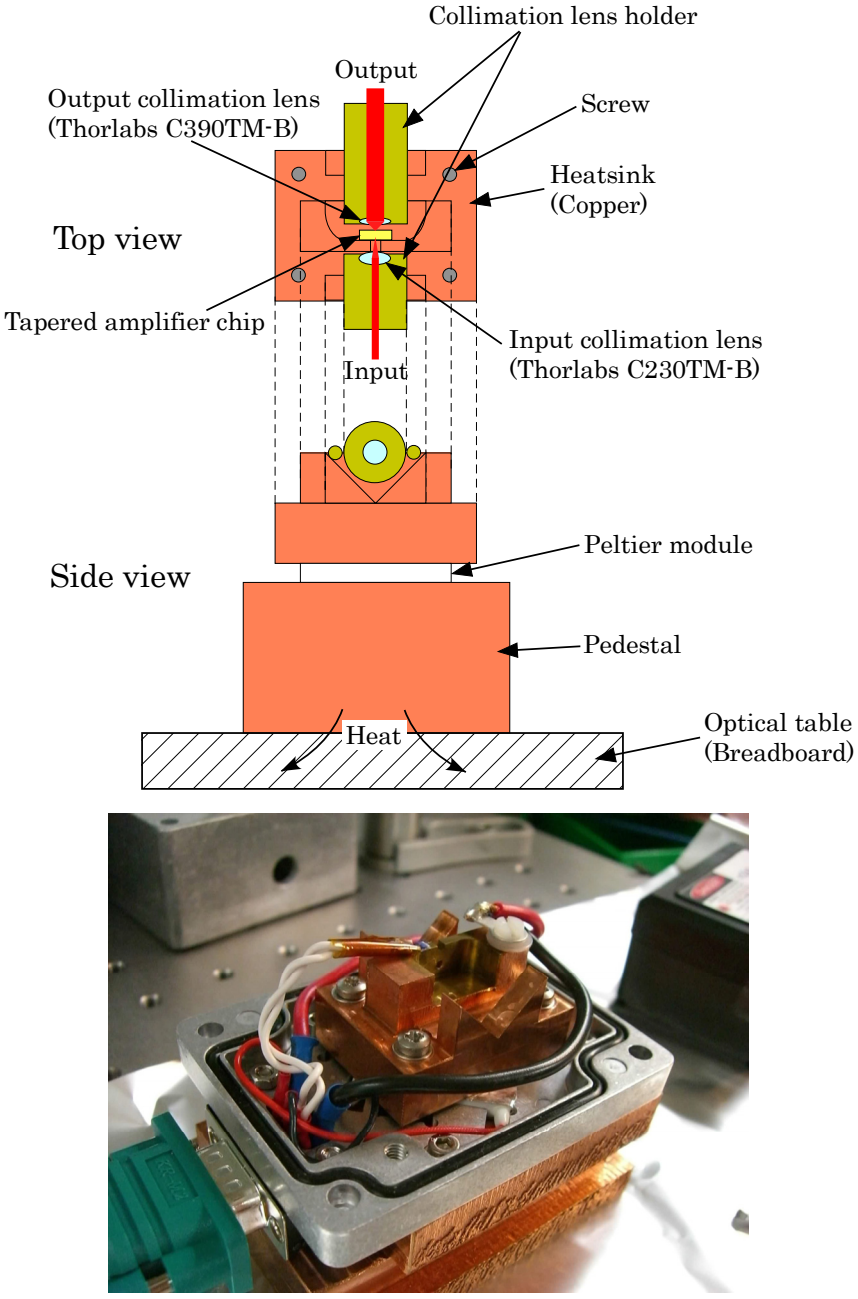

Fig.3.6 Tapered amplifier design and assembled image

A graphite sheet and aluminum foils are used to compensate roughness of the surface of the heat sink and obtain high thermal conductivity. We did not use thermal grease for this purpose as it might have a chemical damage to antireflection coating of tapered amplifier.

Temperature of the heat sink is stabilized with a home made TEC which is a slightly modified version of the one used for a slave laser. We usually set the temperature nearby the tapered amplifier around 20 degrees Celsius. Longer lifetime is expected for lower temperature, though too low temperature leads to condensation which may destroy the chip.

Alignment of collimation lenses are carried out with a mirror mount as illustrated in figure 3.7. Here a mirror mount acts as a stage. It is possible to move the collimation lens in any direction by adjusting the three knob of the mirror mount. Another cylindrical lens is required for the output beam as the beam divergence is different for horizontal and vertical direction.

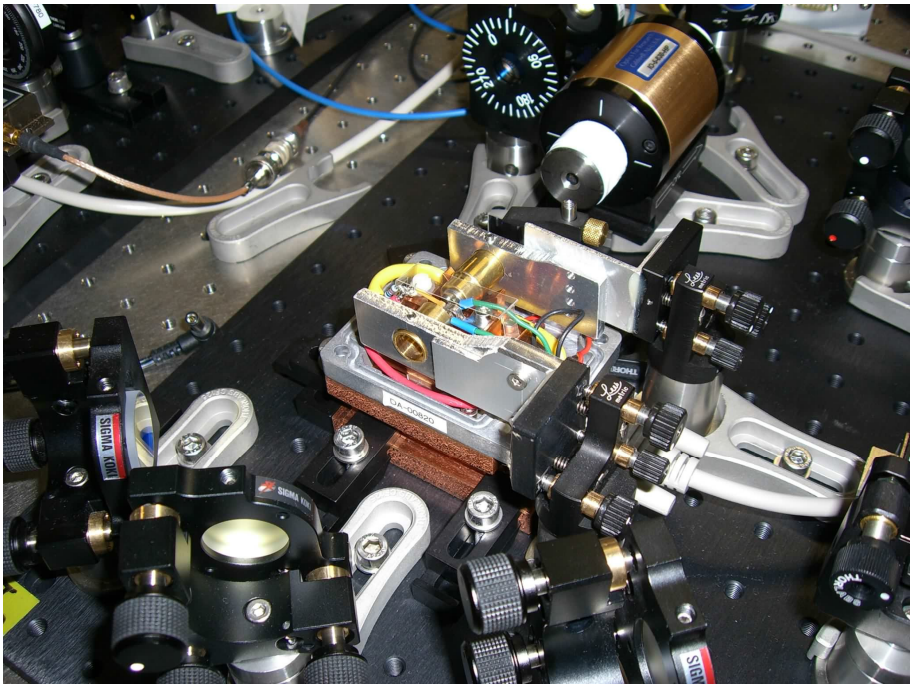

Fig.3.7 Alignment of collimation lenses

Three knobs of a mirror mount enable us to tune a collimation lens holder in any direction precisely. The input lens is adjusted to obtain a maximum output power. The output lens is adjusted such that the output beam is colinear in the vertical direction. The horizontal beam divergence is compensated at the cylindrical lens just after the output collimation lens (see figure 3.9).

Typical characteristics on the power of tapered amplifier are shown in figure 3.8. You can see from these figures that higher power is obtained both by raising the current and with higher power of seed light. If it is possible, the latter way is recommended because the heat generated at the chip is lower for the latter than the former. We usually use about 10mW of seed light and 2.0A of current for 1W tapered amplifier, thus obtaining 600mW after an isolator.

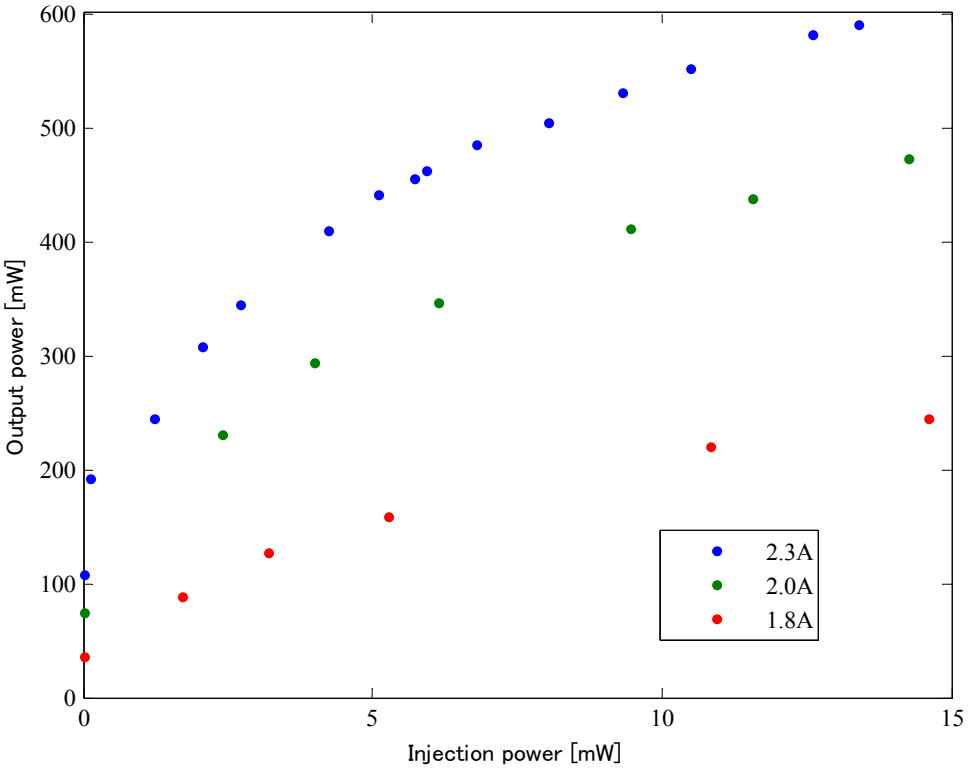

Fig.3.8 (a) Output power of tapered amplifier against injection power

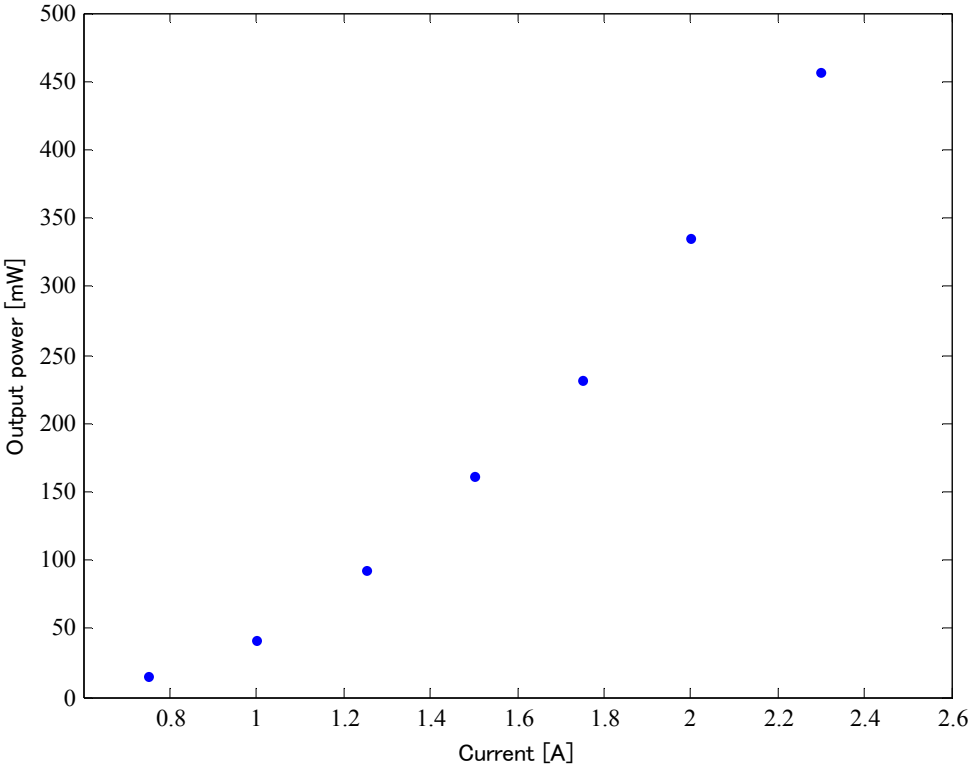

Fig.3.8 (b) Output power of tapered amplifier against current

We construct an amplifying system on a small bread board whose input seed light is supplied with a polarization maintaining single mode (PMSM) fiber and output is coupled to a PMSM fiber, as shown in figure 3.9. Connecting a fiber from a slave laser to this system, you can obtain a mode shaped amplified light from the output fiber. Here acoustic optic module (AOM) serves as a fast switch of light. The diffraction efficiency at AOM is typically 80%. Efficiency of coupling to the output PMSM fiber is limited to around 65% due to a bad spatial mode of the output beam. Thus we can usually use about 200~300mW for experiments.

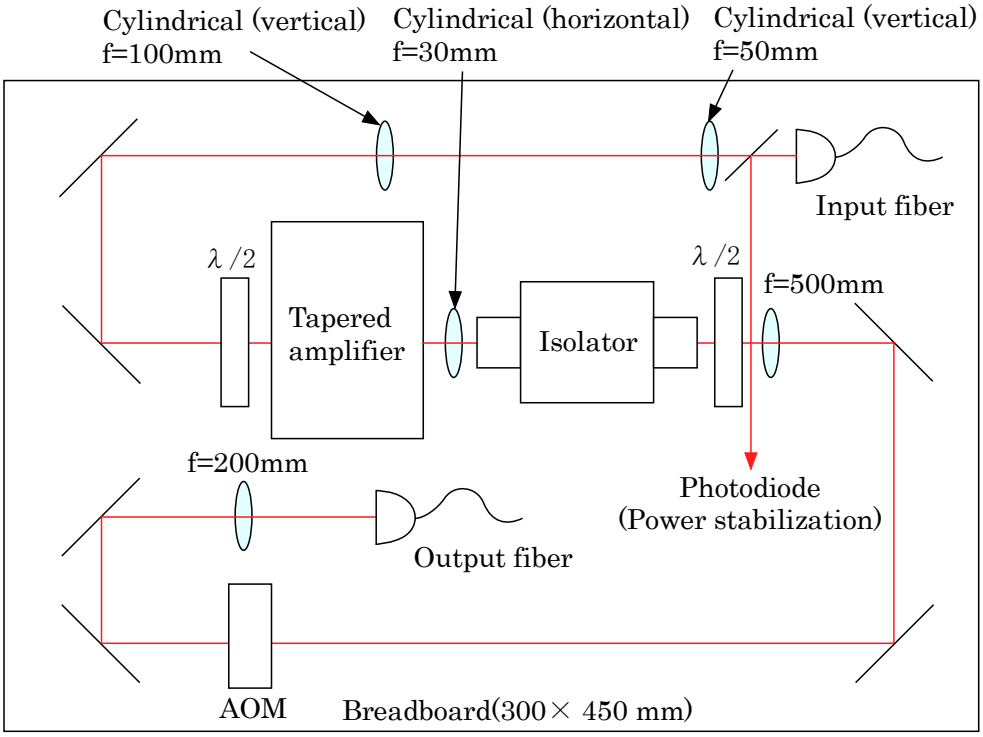

Fig.3.9 Schematics of amplifying system

The two cylindrical lenses after the input fiber match the mode of the input beam to that of the tapered amplifier. The waveplate before the tapered amplifier is adjusted to obtain a maximum output power. The cylindrical lens after the tapered amplifier compensates the horizontal beam divergence. The waveplate after the isolator is used to compensate the polarization rotated at the isolator.

3.1.4 Distributed Feed Back laser

Distributed Feed Back (DFB) laser is a kind of semiconductor laser. Though it appears the same as an ordinary laser diode, it has subtle difference in its internal structure: the width of light emitting semiconductor layer is periodically modulated. This structure works as a grating and select the oscillation wavelength just as done in ECDL. Thus DFB laser itself has a very narrow linewidth (typically around a few Hz) compared to an ordinary laser diode (a few GHz). It means that DFB laser alone can be used for atomic experiments as ECDL; however, the largest advantage of DFB laser lies in a large mode hop free range of 500~1000GHz, which is larger than ECDL by two orders. We use this DFB laser for photoassociation spectroscopy which typically needs tuning wavelength over a few hundred GHz.

Wavelength can be tuned both with current modulation and with temperature modulation. Typical change in wavelength is 25GHz/K and 1GHz/mA. As easily know from these values, stability of temperature and current is necessary to utilize it for spectroscopy. We used commercial TEC unit and current source to ensure these conditions.

Figure 3.10 shows wavelength characteristics of our DFB laser against temperature and current. A large mode hop free range is clearly seen. Figure 3.11 shows saturated absorption spectroscopy of Rb D1 lines with our DFB laser. It shows that the linewidth is narrow enough to carry out spectroscopy.

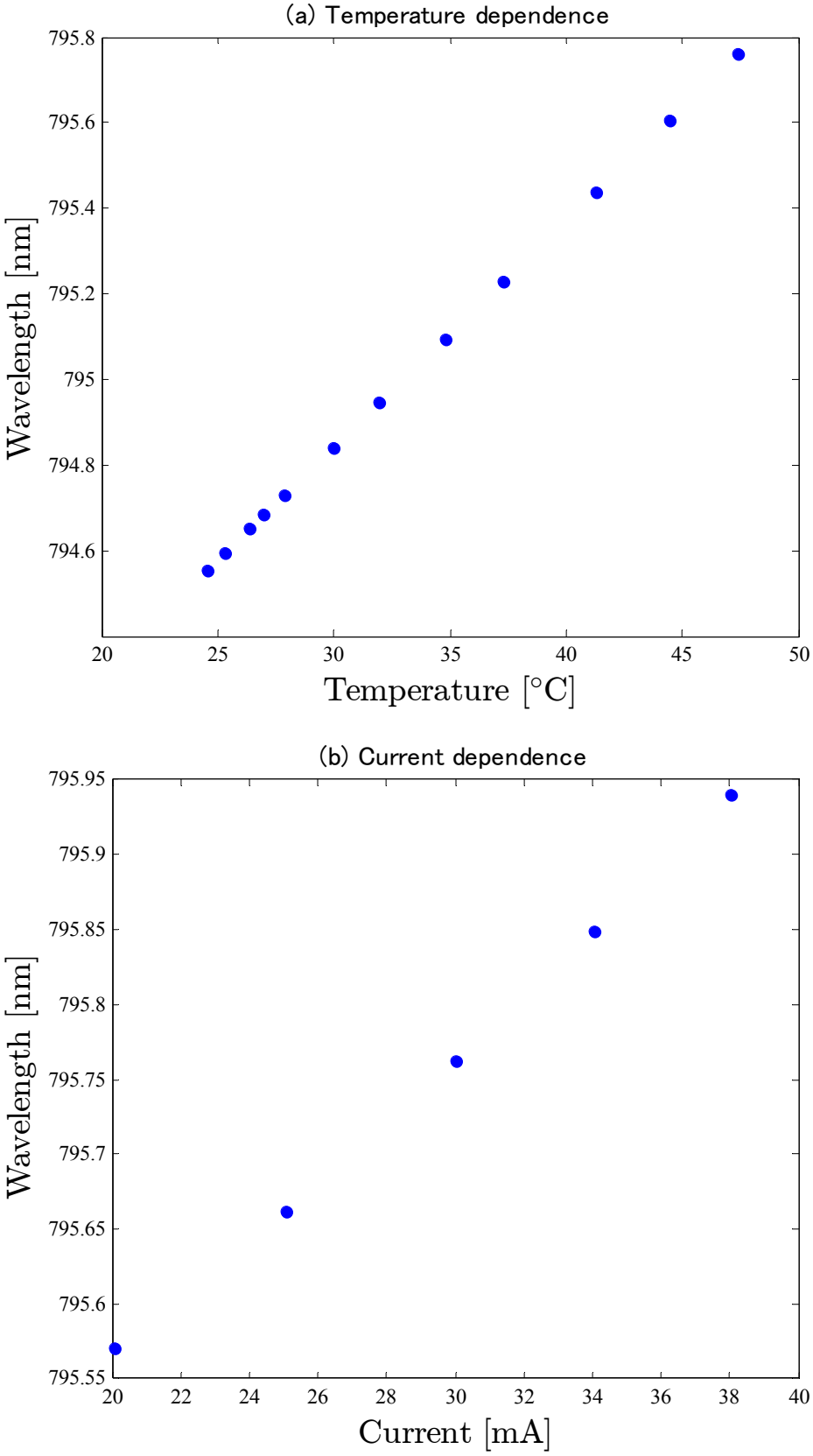

Fig.3.10 Wavelength of DFB laser against (a) temperature and (b) current

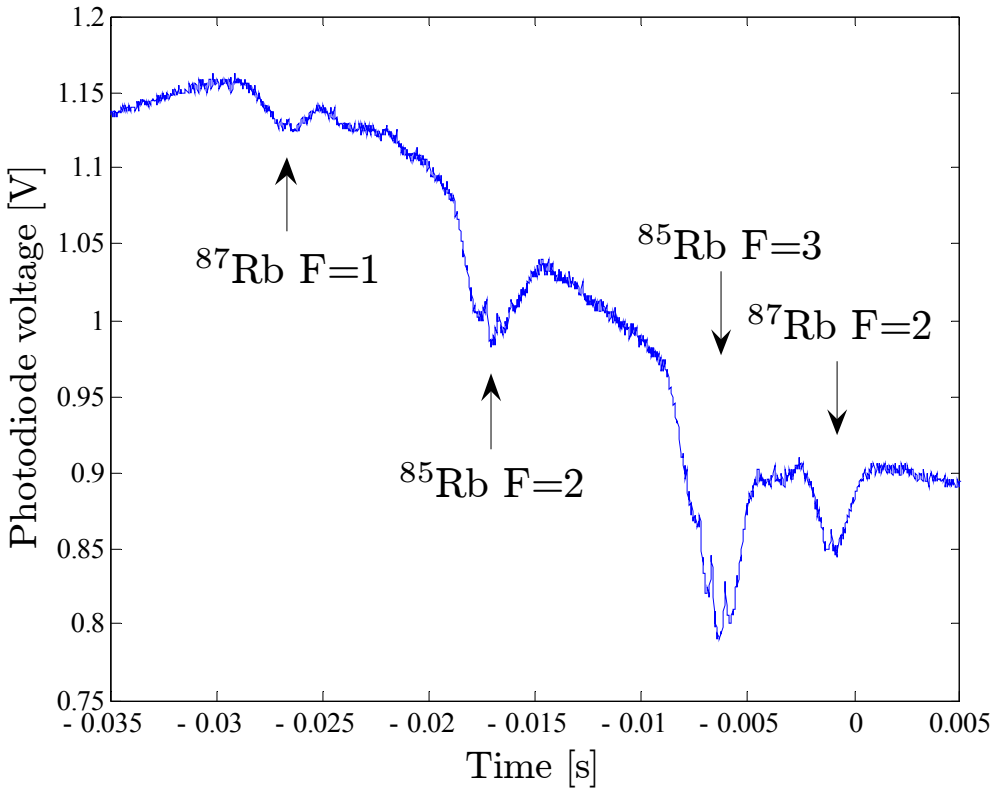

Fig3.11 Saturated absorption spectrum of Rb D1 line observed with the DFB laser
This spectrum is taken by modulating the current. Here 10ms corresponds to around 2.7GHz.

3.1.5 FM sideband locking

To manipulate atoms with light, the light should have long term stability in frequency as well as a narrow linewidth. An ECDL alone does not meet this demand. Thus it is necessary to lock the wavelength of ECDL to an atomic absorption line actively. There are several methods to realize it. Here our standard scheme based on [111] is described.

Figure 3.12 shows our scheme to lock ECDL to an atomic absorption line. The original saturated absorption signal is differentiated with frequency modulation and lock-in and then sent to a servo loop which feed back the difference between current point and set point to piezo voltage and laser current. Fluctuation in the laser frequency locked in this way is typically less than 2MHz. This is sufficiently lower than the natural linewidth of alkali atoms.

For both K and Rb, we heated gas cells to around 70 degrees Celsius to obtain large saturated absorption signals.

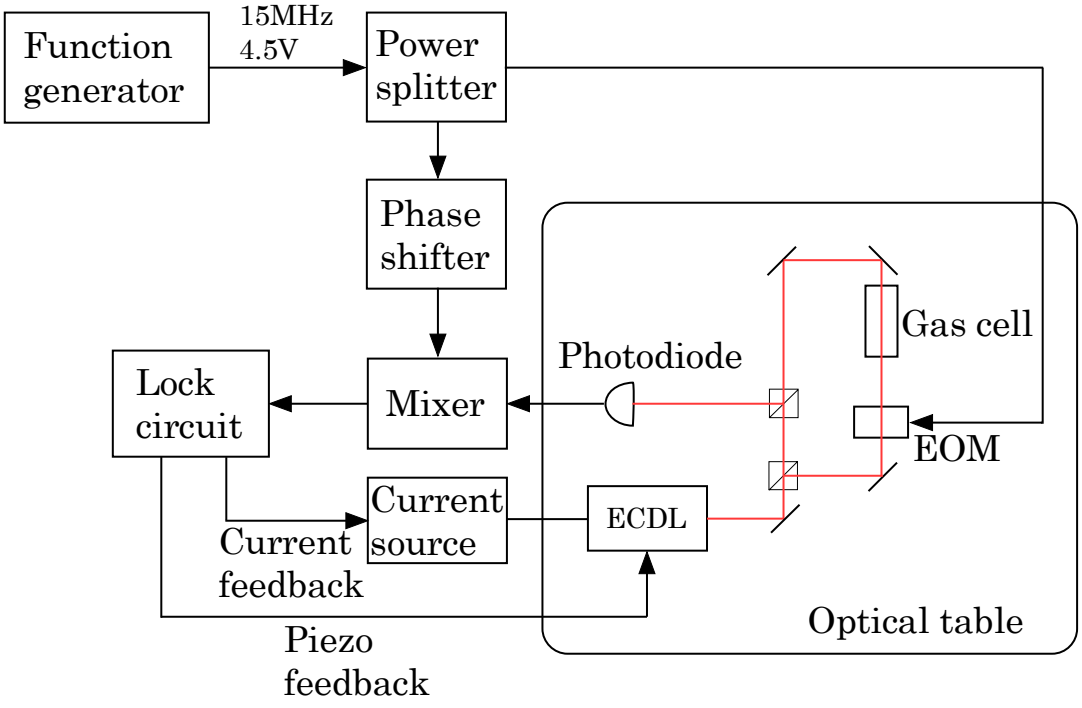

Fig.3.12 Schematics of FM sideband locking

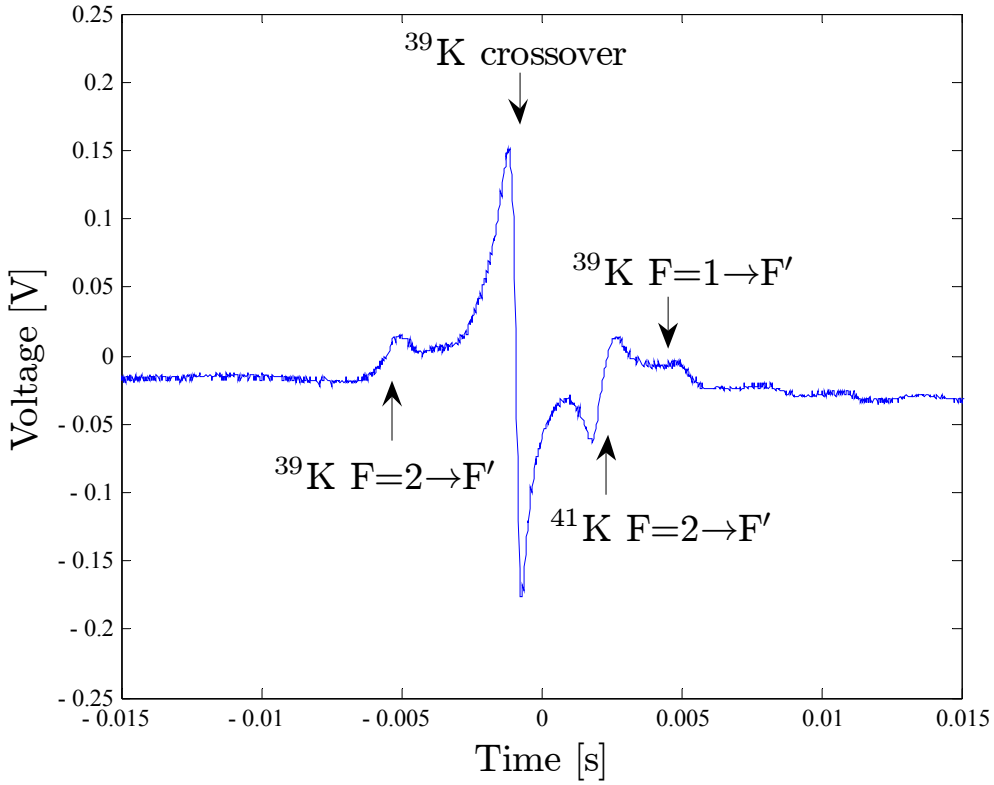

Fig.3.13 Differentiated saturated absorption signal of potassium

The central sharp edge is the differentiated signal of ^{39}K crossover used for our locking. Note that the hyperfine structure in the excited states is quenched in the above peaks.

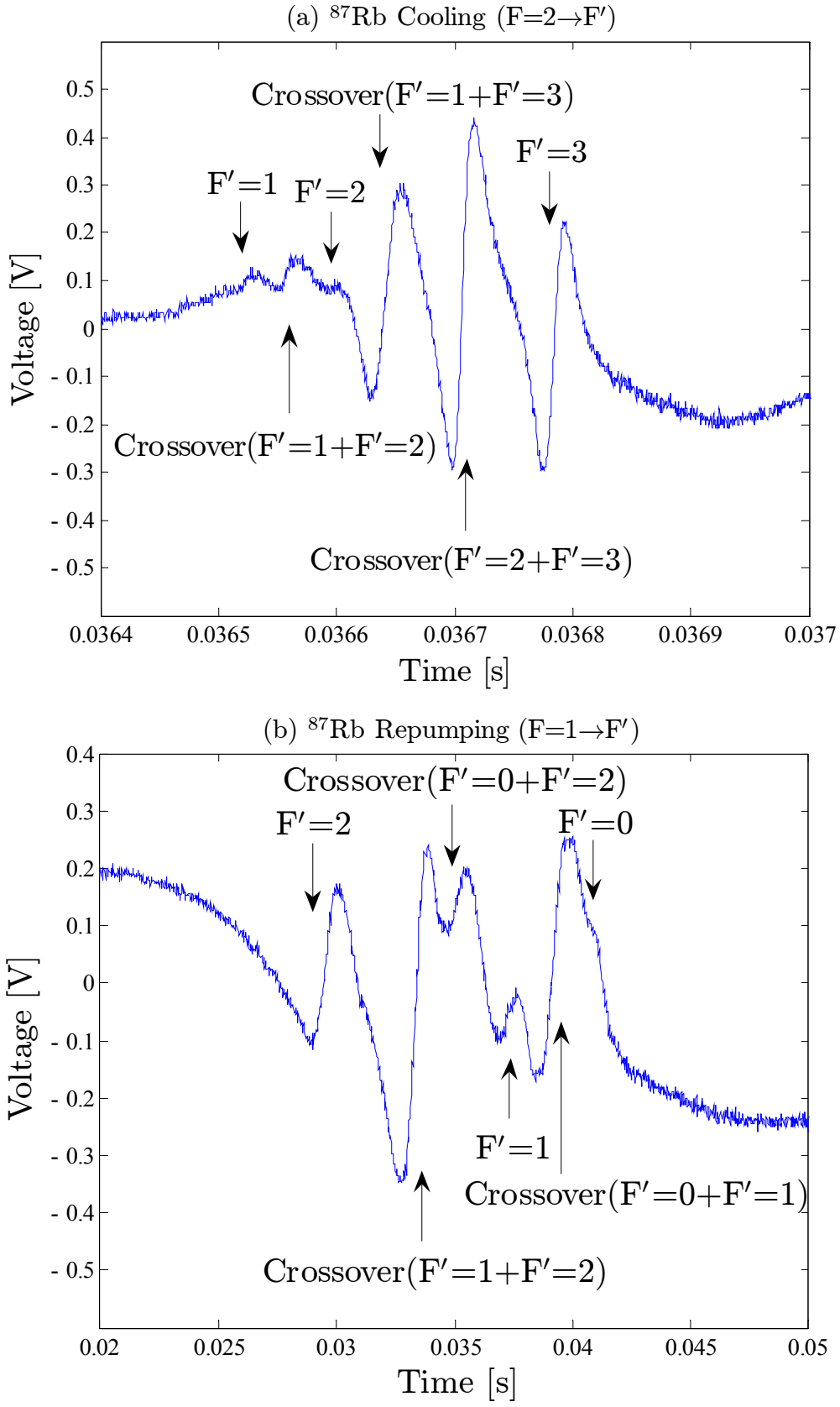

Fig.3.14 Differentiated saturated absorption signal of rubidium of (a) cooling and (b) repumping Cooling is locked to the crossover of F=2→F'=2 and F=2→F'=3 transitions while repumping is locked to the crossover of F=1→F'=2 and F=1→F'=1 transitions.

3.1.6 Pulse laser

A pulse laser is not used for trapping and cooling atoms, but for ionization: its high intensity enables direct multiphoton ionization of atoms and molecules. Resulting ions are detected with microchannel plates, whose detailed description will be given in 3.6.

A dye laser pumped by a 532nm doubled Nd:YAG laser is directly shone to atomic clouds with a diameter of around 1mm. The intensity of the dye laser is easily controlled by a Q-Switch delay of the Nd:YAG laser as shown in figure 3.15. Though the maximum output energy of our dye laser is 30~100mJ depending on the wavelength, we usually set the pulse energy to around 1mJ to avoid an undesirable ionization of atoms attached to the surface of the chamber.

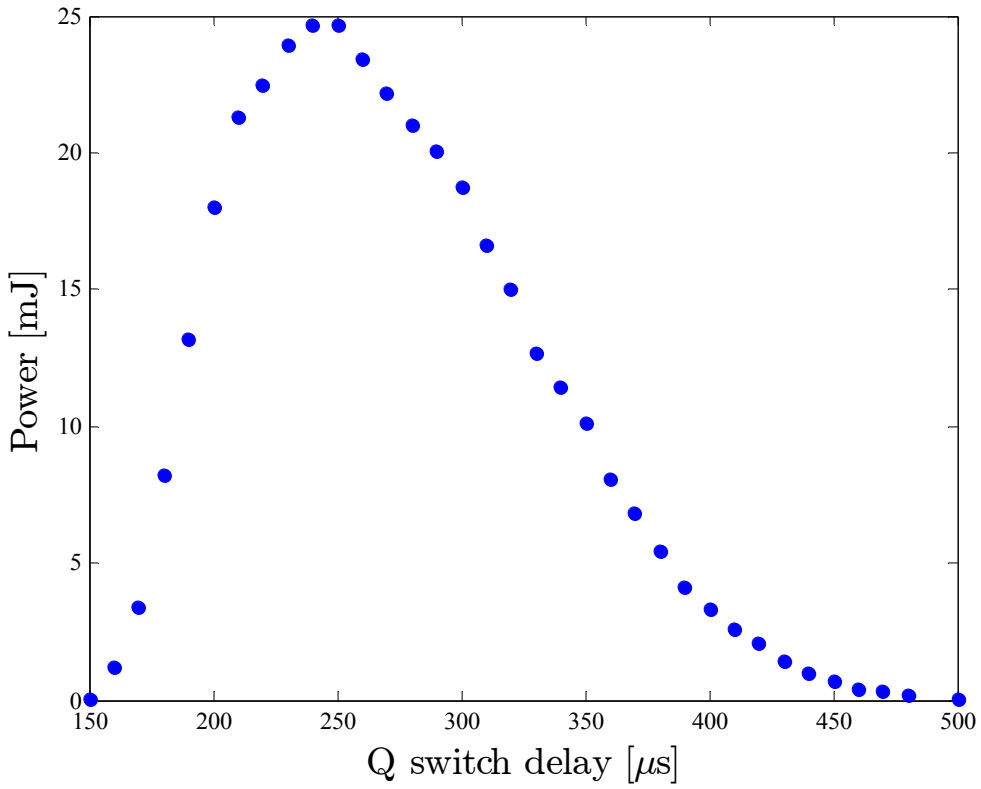

Fig.3.15 Power of doubled Nd:YAG laser against Q-switch delay

3.1.7 Optics

Experiments on cold atoms need many kinds of laser. Here our setup on optics is briefly explained.

In general, we have two optical tables for one experiment: one prepares lasers and the other has a vacuum chamber on it. All lasers are carried with polarization maintaining single mode fibers between the two tables. Figure 3.16 and 3.17 shows optical setup of E1 and E2 experiments, respectively. All MOT beams are first expanded to the diameter of around 25mm and then divided to provide 6 beams which are incident on the chamber. Cooling and repumping beams are overlapped after they are expanded.

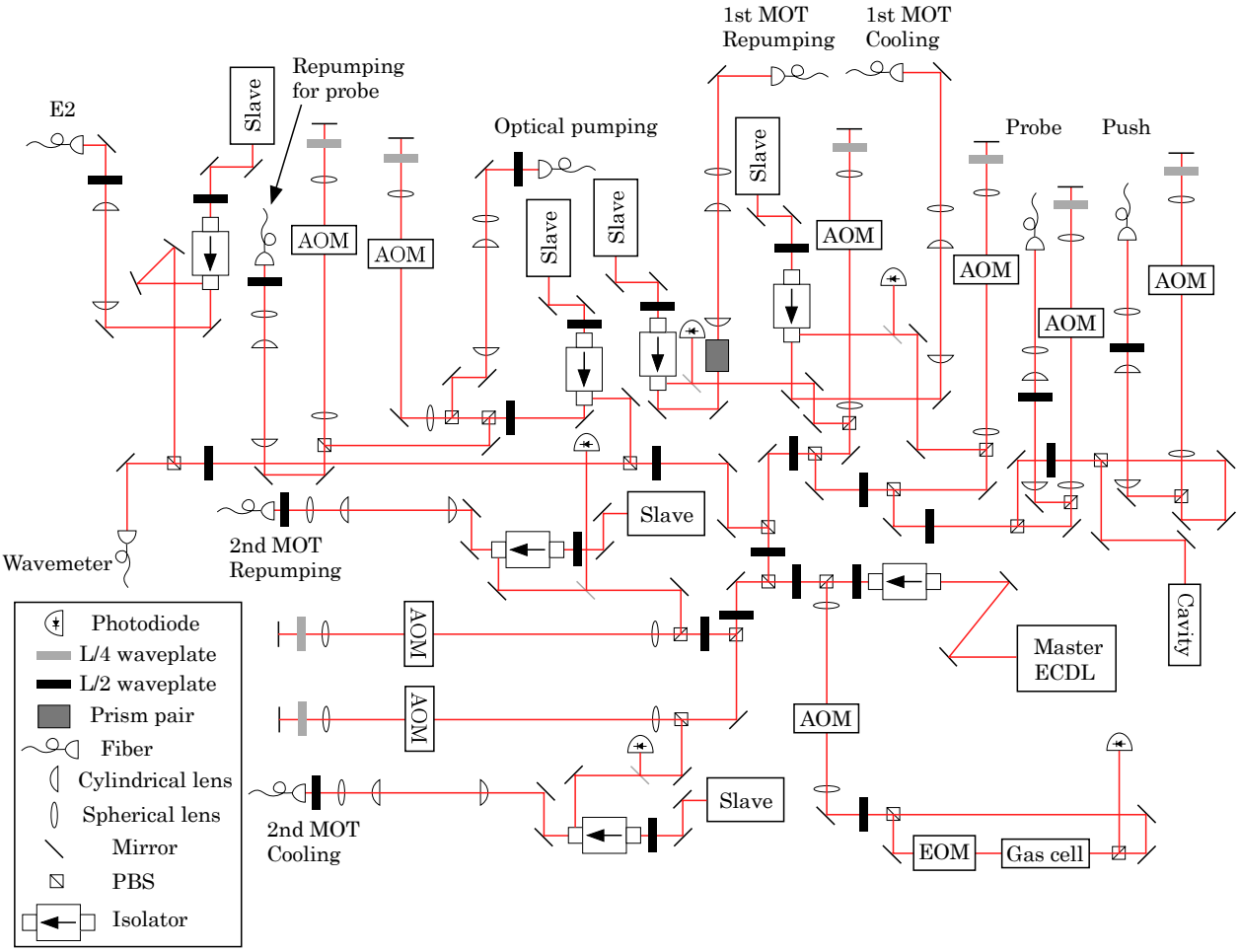

Figure 3.16 E1 optical layout of the potassium lock table

All lights are coupled to fibers and carried to the chamber table. Four MOT lights are amplified by tapered amplifiers at the chamber table. A part of master laser is amplified by a slave laser and carried to the E2 optical table (see figure 3.15). A set of cylindrical lenses are used for compensating an aspect ratio and the difference in the beam divergence.

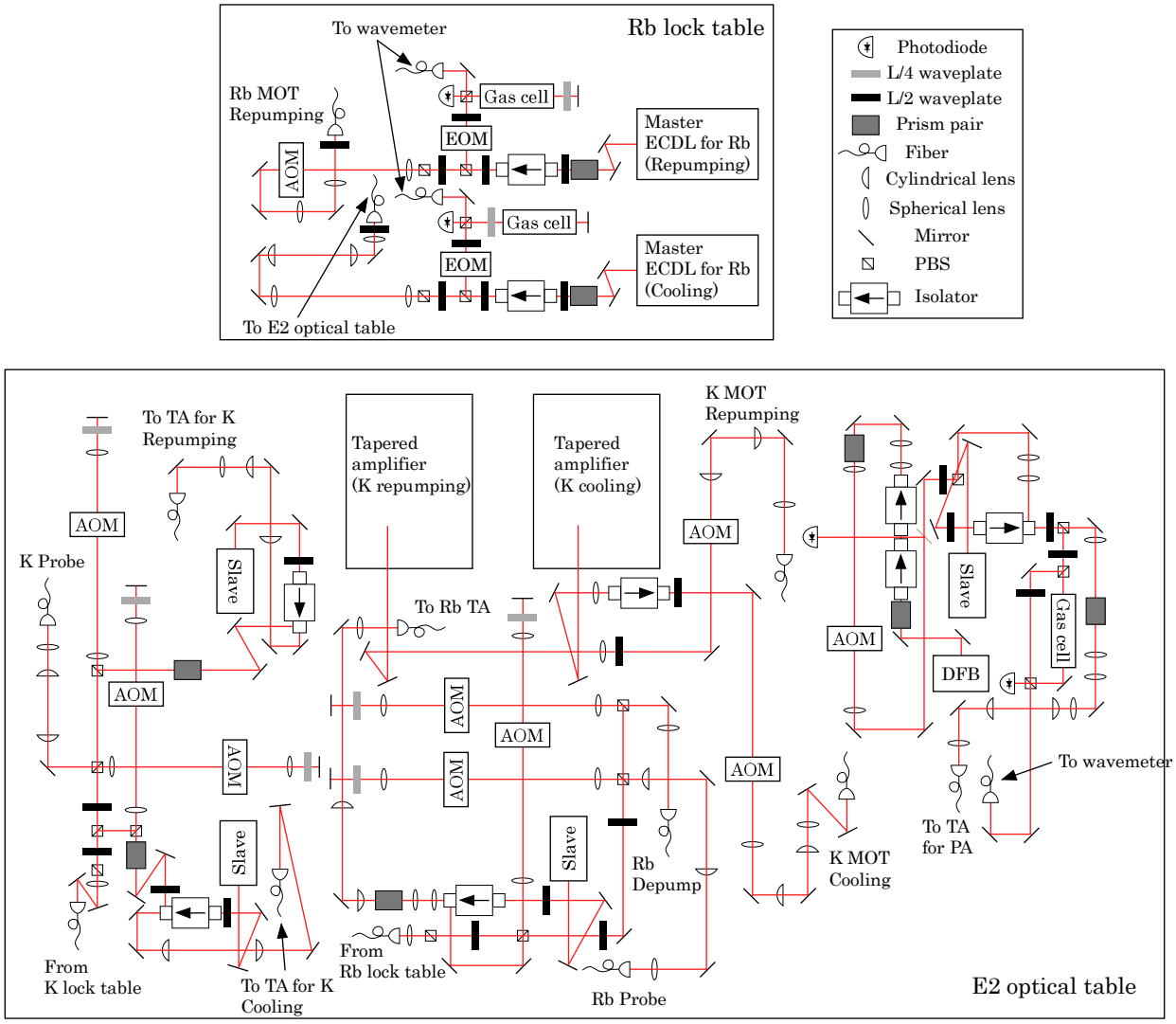

Figure 3.17 E2 optical layouts
The cooling light for rubidium is carried from the rubidium lock table.

E1 experiment adopts a double MOT system. Here the first MOT at the low vacuum side serves as an atomic source while the second MOT at the high vacuum side collects atoms from the first MOT. A push beam which is a slightly blue detuned light is focused to the center of the first MOT, which pushes atoms towards the second MOT.

E2 experiment needs lasers for two atomic species, K and Rb. These two lasers are overlapped with dichroic mirrors. As the resonant frequencies of these two atoms are close to each other, waveplates for one frequency are shared.

3.2 Vacuum chamber

Laser cooling and trapping of atoms are carried out under ultrahigh vacuum environment to avoid collisions between cooled atoms and room temperature hot atoms. Thus construction of a vacuum chamber which can reach a vacuum of 10^{-9} Torr or higher is an important task.

The vacuum chamber of E1 experiment is an assembly of commercial vacuum components. It has two cells where MOT is carried out and they are connected by metal components. Two ion pumps and a titanium sublimation pump is utilized to obtain ultrahigh vacuum of the order of 10^{-11} Torr. The E2 chamber is based on a custom-made metal chamber. Only one ion pump is sufficient to obtain ultrahigh vacuum of the order of 10^{-9} Torr. Schematics of these two chambers are shown in figure 3.18.

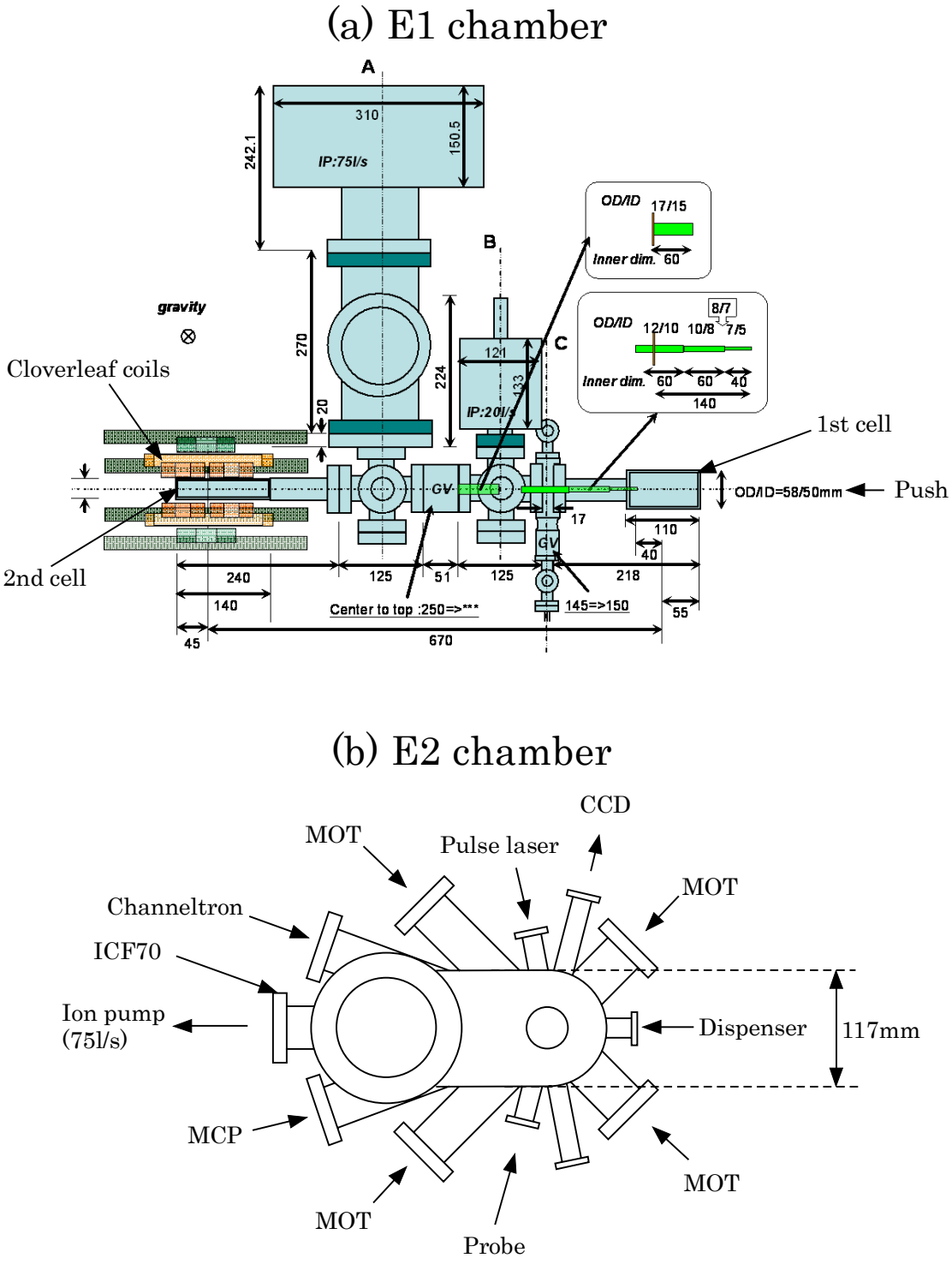

Fg.3.18 Schematics of the vacuum chambers of (a) E1 and (b) E2

These figures omit a pumping station which is a combination of a turbo pump and a scroll pump. A pumping station is connected to the angle valve shown in the above figure and evacuate the chamber to 10^{-7} Torr before an ion pump is turned on. If an ion pump begins to operate, the angle valve is closed and the pumping station is separated as the vibration of scroll pump and turbo pump affects the experiments.

Usually we have to bake the chambers to reach an ultrahigh vacuum regime. The basic mechanism of this operation is simple: if you heat the chamber and keep on drawing a vacuum with a pumping station, background atoms attached to the surface of the chamber fall off the chamber by the heat and eventually drawn into a pumping station. The temperature of the chamber is monitored and kept constant around 200 degrees Celsius. This operation removes background gases such as hydrogen, oxygen and nitrogen from the chamber. An ion pump is turned on after baking. A few days of baking is sufficient for 10^{-10} Torr with an ion pump, though a titanium sublimation pump is necessary to reach 10^{-11} Torr.

Both E1 and E2 chambers have dispensers as an atomic source in them. A dispenser emits atoms through a chemical reaction when it is heated via a current flowed to it. It is easy to control the amount of yield with the current. As it is based on a chemical reaction, there is a threshold current at which atoms begin to yield. We use a commercial dispenser for Rb and ^{39}K atoms, while home made ones based on [112] are used for ^{41}K atoms.

3.3 Computer control

Manipulation of atoms is carried out with a digital and analog control of many apparatuses within a short time. It is impossible to do this with a manual operation, which means that a computer control system is required for all experiments. We use a LabView code developed by Dr.T.Mukaiyama. An example of timing control on a computer is shown in figure 3.19.

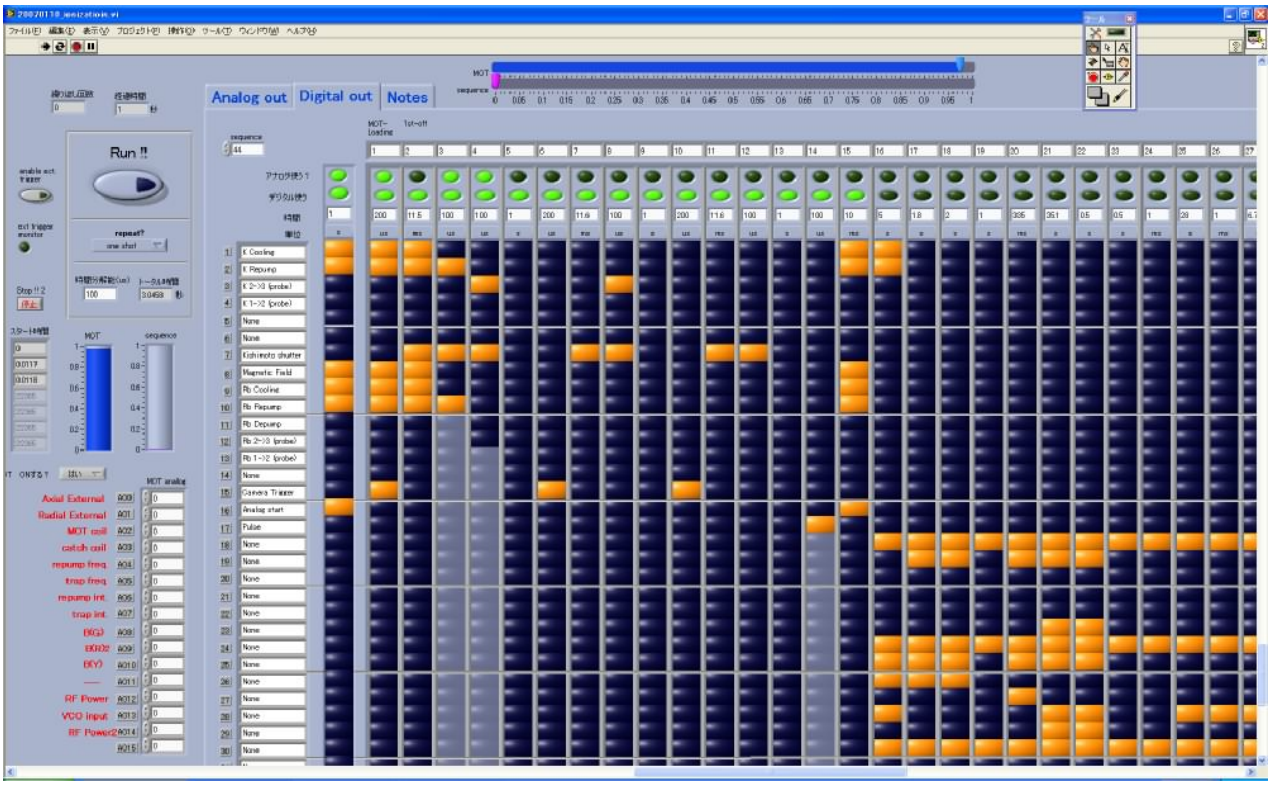

Fig.3.19 Image of LabView program

3.4 Estimation of number of atoms with fluorescence

It is important to know number of atoms in a MOT as it reflects conditions on MOT light and the abundance of trapped atoms and background junk atoms in the chamber. In the case of condensate experiments, estimation of number of atoms is also important because it is closely related to whether you can obtain a condensate from the laser cooled atoms or not.

The most simple and reliable way to estimate number of atoms in a MOT is to count number of photons scattered by the atomic cloud with a photodiode. An atom in a MOT always scatters MOT light to any direction with a rate

$$\frac{\Gamma}{2}\frac{I/I_s}{1+I/I_s+(2\Delta/\Gamma)^2} \tag{3.1}$$

where Γ denotes the natural linewidth of atoms, I denotes the intensity of MOT light at the atomic cloud, I_s denotes a saturation intensity of the atom and Δ denotes the detuning of MOT light from resonance. Thus a MOT containing N atoms emits photos with a rate

$$\frac{N\Gamma}{2}\frac{I/I_s}{1+I/I_s+(2\Delta/\Gamma)^2} \tag{3.2}$$

Now consider a configuration to count number of photons emitted from a MOT as shown in figure 3.20. A part of photons are collected by a lens and focused to a photodiode. Multiplying the solid angle Ω to the expression (3.2), number of photons incident on the photodiode within a unit time is expressed as

$$\frac{N\Gamma\Omega}{2}\frac{I/I_s}{1+I/I_s+(2\Delta/\Gamma)^2} \tag{3.3}$$

On the other hand, you can know number of photons incident on the photodiode from the current flowed to the resistance illustrated in figure 3.18. If the sensitivity of the photodiode at the wavelength of photons is written as S in units of A/W, number of photons incident on the photodiode per unit time is described as

$$\frac{V}{RSh\nu} \tag{3.4}$$

where $h\nu$ is energy of a photon, V is the measured voltage and R is the output load. The value of S is measured at the corresponding wavelength as it largely depends on the wavelength. Equating (3.3) and (3.4) yields the expression for number of atoms in the MOT

$$N=\frac{2V}{\Omega RSh\nu\Gamma}\frac{1+I/I_s+(2\Delta/\Gamma)^2}{I/I_s}$$

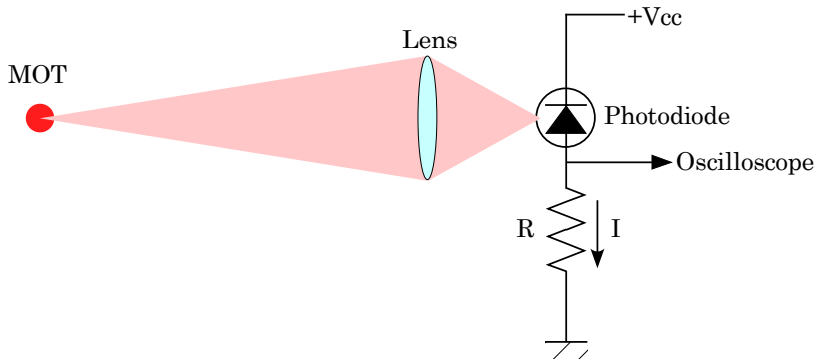

Fig.3.20 Counting number of atoms in a MOT with the fluorescence
The photodiode should have a larger area than the focused image of MOT.

Though number of atoms can also be estimated from an absorption imaging as explained in 3.5, estimation with fluorescence from a MOT is more reliable: absorption imaging suffers from the maximum amount of absorption that can be detected with CCD as well as depends on the relation between the polarization of probe light and the bias magnetic field. On the contrary, there is no unclear factor in the fluorescence method, and thus it gives a reliable estimate.

The above model is correct only for a two level system. It is a good approximation to deal with the optical transition between particular hyperfine states for most of alkali atoms, but not for ^{39}K and ^{41}K. We used a 6 level model which takes into account the effect of other hyperfine states for correct estimation of number of atoms [113]. Compared to the 6 level model, we did not observe significant difference from the model that F=2-F'=3 transition for the trapping light and F=1-F'=2 transition for the repumping light are separately closed transitions.

3.5 Absorption imaging

Experimental results are obtained by taking images of atoms with CCD camera. The amount of absorption at an atomic cloud is measured by irradiating a resonant probe beam to the atoms. Three images, one with atoms and a probe light, one without atoms and with a probe light and one without atoms and a probe light, are taken in each run and yield an image of optical density (OD) which shows the amount of absorption. Fitting to this image gives the size and density of atomic cloud, which are used to deduce total number of atoms. Temperature of atoms is known by taking a several images changing the time of flight: the speed of spread of an atomic cloud reflects its temperature. Here we briefly see how a temperature of atoms is derived from the measured size of an atomic cloud. First we assume that the spatial distribution of trapped atoms has a Gaussian shape:

$$f_0(\mathbf{r}) = (2\pi)^{-3/2}(\sigma_x\sigma_y\sigma_z)^{-1}\exp\left(-x^2/2\sigma_x^2 - y^2/2\sigma_y^2 - z^2/2\sigma_z^2\right) \tag{3.5}$$

We also assume that atoms obey the Maxwell-Boltzmann distribution

$$f_{MB}(\mathbf{v}) = \left(\frac{2\pi k_B}{m}\right)^{-3/2}(T_xT_yT_z)^{-1/2}\exp\left[-\frac{m}{2k_B}\left(\frac{v_x^2}{T_x}+\frac{v_y^2}{T_y}+\frac{v_z^2}{T_z}\right)\right]$$

This distribution means that the probability that atoms located at the origin at $t = 0$ are found at $\mathbf{r}$ after a time of flight of t is

$$f_{MB}(\mathbf{r},t) = \left(\frac{2\pi k_B t^2}{m}\right)^{-3/2}(T_xT_yT_z)^{-1/2}\exp\left[-\frac{m}{2k_Bt^2}\left(\frac{x^2}{T_x}+\frac{y^2}{T_y}+\frac{z^2}{T_z}\right)\right] \tag{3.6}$$

Taking a convolution of (3.5) and (3.6), we obtain the spatial distribution of atoms after time of flight of t:

$$f(\mathbf{r},t) = \int dx'dy'dz' f_0(\mathbf{r}')f_{MB}(\mathbf{r}-\mathbf{r}',t) \tag{3.7}$$

As is easily known from the form of (3.5) and (3.6), (3.7) is written as a product of x, y and z components. Here we only deal with calculations for the x component in detail. The y and z components are also calculated in a similar manner. Carrying out an integral on x' of (3.7), we obtain an expression for the distribution in the x direction:

$$f_x(x,t) = \left[2\pi\left(\sigma_x^2+\frac{k_BT_xt^2}{m}\right)\right]^{-1/2}\exp\left(-\frac{x^2}{2\sigma_x^2+2k_BT_xt^2/m}\right) \tag{3.8}$$

If we assume that the measured atomic distribution after a time of flight of t has a similar form to (3.5), the measured width of atomic cloud σ is related to the temperature T as

$$\sigma_i^2(t) = \sigma_i^2 + \frac{k_B T_i}{m} t^2 \tag{3.9}$$

where $i = x, y$ and z. The expression (3.9) is used to derive a temperature of atoms in the whole experiments.

Typical arrangement of the optical layout for an absorption imaging is shown in figure 3.21. The image of atomic clouds is focused onto the CCD. It is noteworthy that the fluorescence scattered by atoms is also focused to the CCD when the imaging is successful. It reduces OD of the atomic clouds when the MOT light is not completely turned off at the time of the imaging. Thus it is important to reduce the fluorescence as far as you can. We pay attention to the next two points. First, the first lens should be placed far from a MOT. This contributes to reduce the amount of the fluorescence on the CCD quadratically as the distance between the MOT and the lens increases. Second, an iris should be inserted at the focus of the probe beam. The probe beam which has information on the OD of atomic clouds can pass through this iris, whereas most of the fluorescence is cut off at this iris.

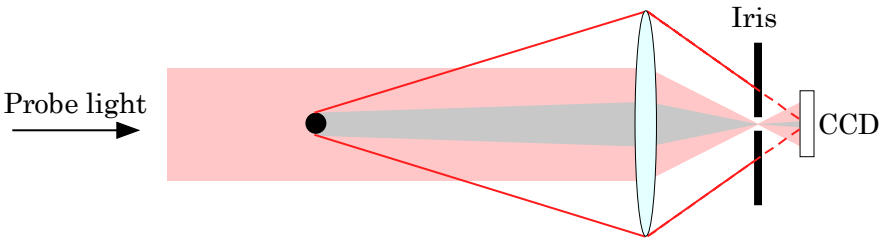

Fig.3.21 Absorption imaging with an iris
The shadow of the atomic cloud is cast on the CCD. The probe light passes through the iris, while most of the MOT fluorescence indicated in the red line is blocked by the iris. Note that the shadow is also focused at the CCD and not at the iris.

In actual experiments, we always have to note the value of OD: if it exceeds 3, then it might be not correct. It is easily understood by considering the actual value recorded on the CCD. If you use 16 bit CCD, the recorded value of the probe beam without atoms is kept around 10000. In the case of imaging of OD 4, the recorded value of the transmitted light is $10000/e^4$ which is around 180. This value is close to the value of background noise. Thus too high OD causes a saturation of the absorption image. If OD seems to be too high, it is necessary to detune the probe beam from the resonance. In that case, the actual OD is easily obtained by multiplying the following factor:

$$1 + \left(\frac{2\Delta}{\Gamma} \right)^2$$

which is derived from (3.1) for sufficiently low intensity light.

3.6 Ion counting with a microchannel plate (MCP)

Ion counting offers a sensitive tool for detecting atomic and molecular ions. Even one atom or molecule can be detected with an electron multiplier tube just as in the case of photon counting. Here its principle and basic operation are briefly described.

An MCP has a lot of channels which work as electron multipliers independently. Figure 3.22 shows the mechanism of detecting ions with an MCP. First ions are accelerated by an electric field applied between MCP and the ground. They collide to MCP to generate secondary electrons with a quantum efficiency of around 50% [114]. These electrons are further multiplied by repeating collision to the surface of MCP and generation of secondary electrons. Finally a single ion generates 10^5~10^6 secondary electrons in each tube which are collected to an anode. The resulting signal is sent through a low pass filter to suppress fast noises and then amplified with a home made preamplifier [115] and acquired by a computer.

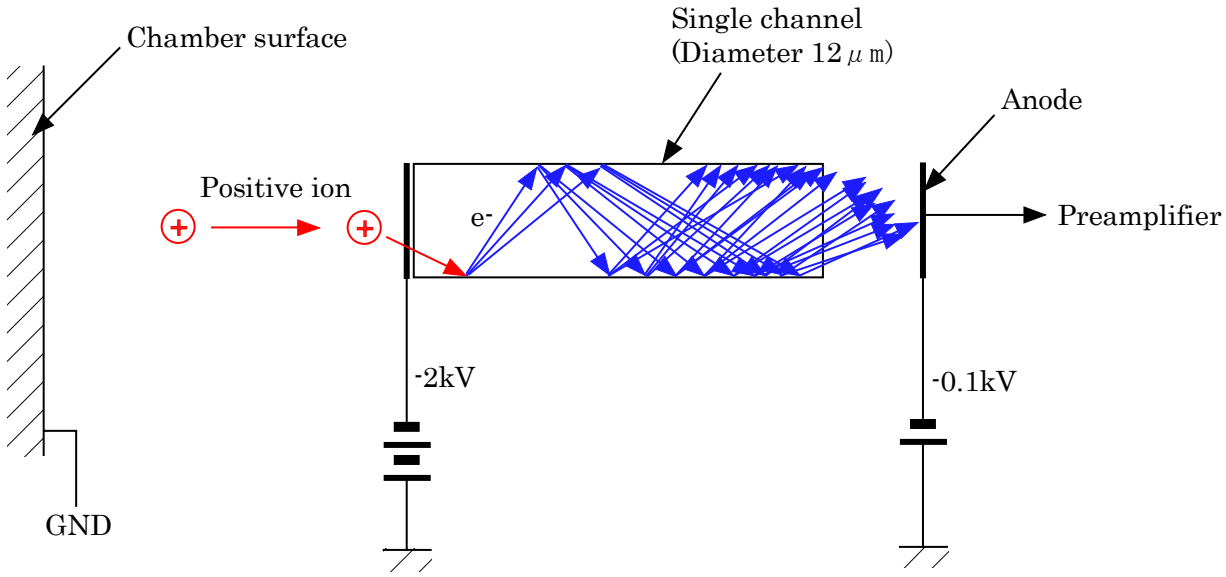

Fig.3.22 Detection of positive ions with an MCP
Here only one channel is shown. Actually there are many channels in an MCP.

Note that the output voltage of MCP is determined by a capacitance of MCP in a pulsed operation. When a charge Q is generated at a single shot, the output voltage V from MCP which has a capacitance of C is written as

$$V = \frac{Q}{C}$$

and does not depend on an output load. This is not the case for a continuous operation: MCP works as a constant current source in that case and the output voltage of MCP is determined by the resistance connected to the anode.

Chapter 4 Results and analysis

Since I was engaged in the two experiments, E1 and E2, here the results obtained at each experiment are described separately. In 5.1, the result of the first experiment on potassium at our lab is presented. We tried magneto-optical trapping of ^{39}K as a first step and evaluated its properties. Especially we studied the efficiency of a double MOT system of ^{39}K, where atoms are first collected from dispensers at 1st MOT and then transferred to the second MOT by a resonant laser to be recaptured and used for subsequent experiments, because there are a few reports on the double MOT system for potassium. We showed that a continuous double MOT system is also efficient for ^{39}K as rubidium atoms.

Section 4.2 presents our main results on the laser cooling of ^{41}K atoms. More detailed investigations on the properties of a ^{41}K MOT is carried out with absorption imaging than that of ^{39}K. We confirmed that laser cooling of ^{41}K is quite less efficient than other alkali atoms, as is already reported. At a particular condition that trapping and repumping light induces a Raman transition between two ground state hyperfine levels, we saw that number of atoms in a MOT is quite large while density is low and temperature is high, where the phase space density is quite low compared with other alkali atoms. However, it is found out that a time dependent MOT can improve the phase space density of the original continuous MOT by three orders.

Section 5.3 describes the first result at E2 experiments. We have characterized a dual species MOT of ^{41}K and ^{87}Rb. Atoms and molecules are ionized by a doubled pulsed Nd:YAG laser and then detected with a MCP. Utilizing this method, we performed photoassociation spectroscopy of ^{41}K^{87}Rb molecules.

4.1 Laser cooling of ^{39}K at E1

4.1.1 Number of atoms measured with fluorescence

As there is little information on laser cooling of ^{39}K, first we measured number of atoms with fluorescence from the MOT as a function of intensity and detuning of the MOT light. Figure 4.1 and 4.2 shows the respective results.

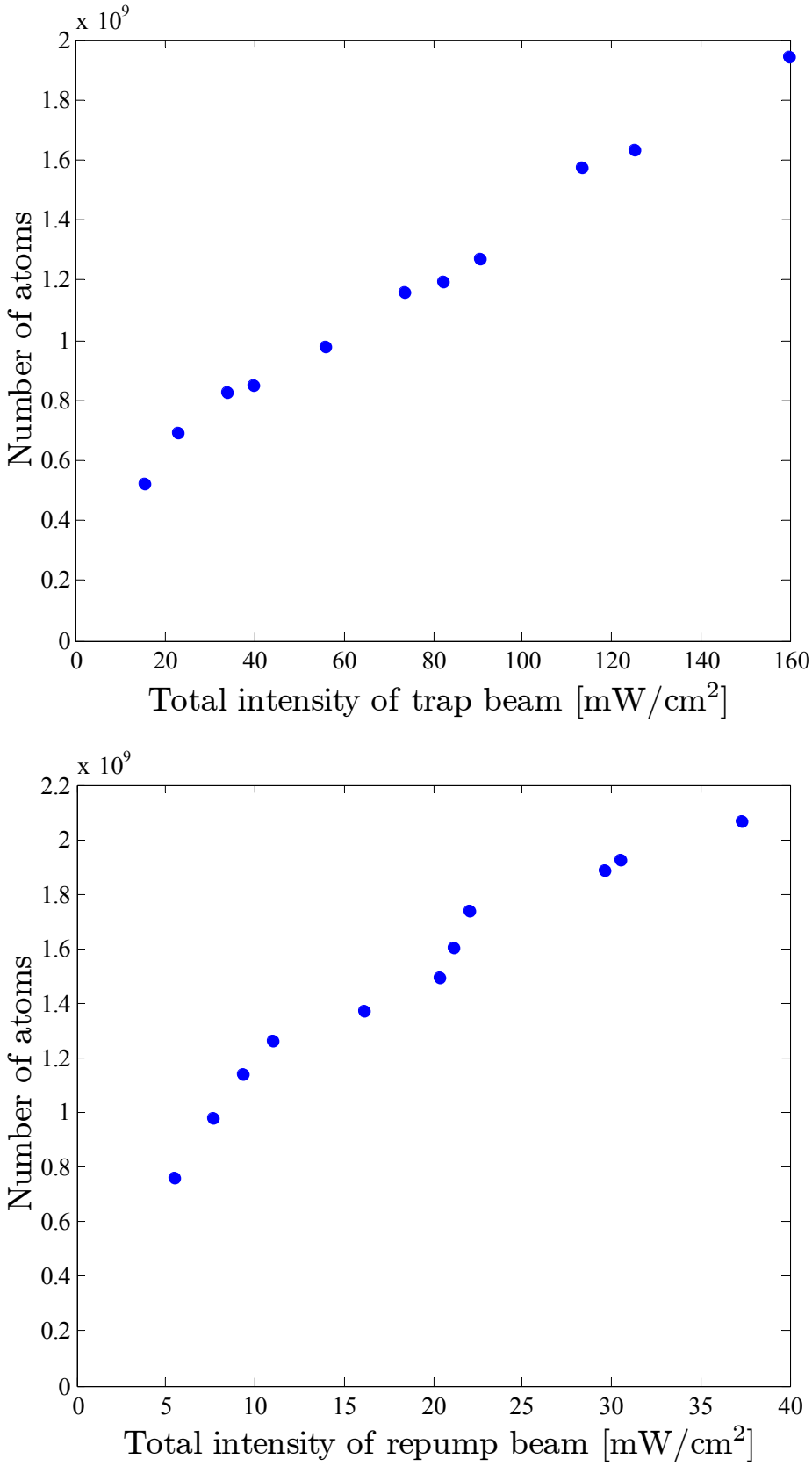

Figure 4.1 Number of atoms against intensity of trapping and repumping beam

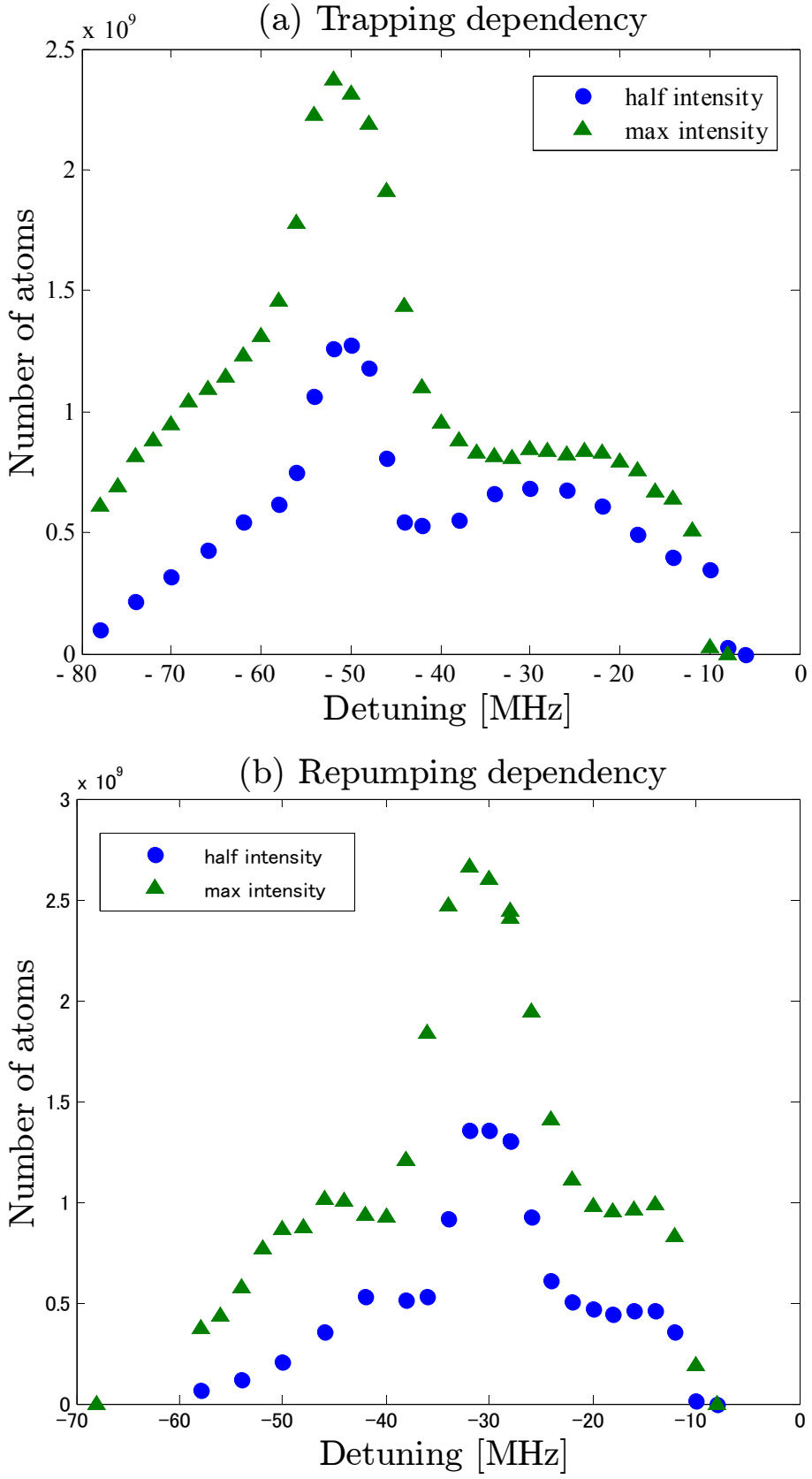

Figure 4.2 Number of atoms plotted against detuning of (a) trapping (b) repumping beam

As is clearly seen from figure 4.1, higher intensity of the MOT beam leads to larger number of atoms for both trapping and repumping laser. Though trapping laser often shows this tendency for other alkali atoms, it is unusual for repumping laser among other alkali atoms. We consider it to be caused by an unusual high

hyperfine pumping rate between ground state F=2 and F=1 levels as already suggested by [54]. It is noteworthy that number of atoms actually trapped in the MOT is comparable to that of other alkali atoms, which is probably due to our large beam diameter and large capture velocity of ^{39}K which can compensate the low friction force in our ^{39}K MOT.

A clear dependency on the detuning of the MOT light in figure 4.2 shows there is a good condition in number of atoms both for trapping and repumping light, though there is no real state in this region of the atomic structure. Though we have not investigated this behavior in detail here, we can see that the width of the peak in number of atoms decreases when the intensity of the MOT light is reduced. Later a similar behavior was observed also for ^{41}K, and we specified that this phenomenon occurs when trapping and repumping laser satisfies a Raman condition that connects ground state F=2 and F=1 levels. Actually the width of the peaks in number of atoms in figure 4.2 well coincides with the linewidth of the corresponding Raman transition. Although this kind of behavior has not yet reported for other atomic species, previous experimental works for potassium atoms have probably used this resonance to enhance number of atoms and the theoretical calculation [62] seems to have suggested this phenomenon.

4.1.2 Properties of the 2nd MOT

Before detailed characterization and optimization of the push beam, we briefly studied the properties of the 2nd MOT. The situation is quite different from the 1st MOT: room temperature hot atoms are captured in the 1st MOT, while the 2nd MOT captures laser cooled atoms accelerated by a resonant laser. Here we changed only the intensity of the MOT laser and did not change the detuning since the laser source is the same as the 1st MOT. Figure 4.3 shows number of atoms in the 2nd MOT measured against the intensity of the 2nd MOT laser. It is clear that high intensity is not necessary for the 2nd MOT to trap atoms from the 1st MOT. This means that even accelerated atoms have the velocity within the capture range of moderate intensity. We can see that a large capture range of ^{39}K which is already reported in [54] is advantageous to a double MOT configuration.

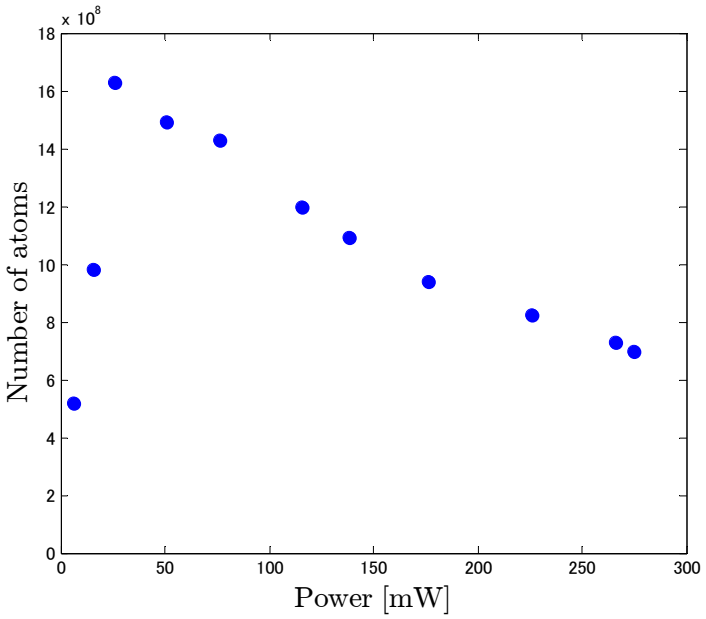

Fig.4.3 Number of atoms in the 2nd MOT against MOT beam power

For estimation of the minimum diameter required to trap atoms at the 2nd MOT, we measured number of atoms against the beam diameter of MOT light. The beam diameter is changed by inserting an iris into the

MOT beam. Knowledge on a minimum diameter for the MOT was necessary to design and make a magnetic trap which was used to cool atoms evaporatively to make a condensate. Figure 4.4 shows the change in number of atoms when the diameter of all 6 MOT beams is changed equally. On the other hand, figure 4.5 shows the change in number of atoms when the diameter of one of 6 MOT beams is changed. The experimental configuration of figure 4.5 is explained in figure 4.6.

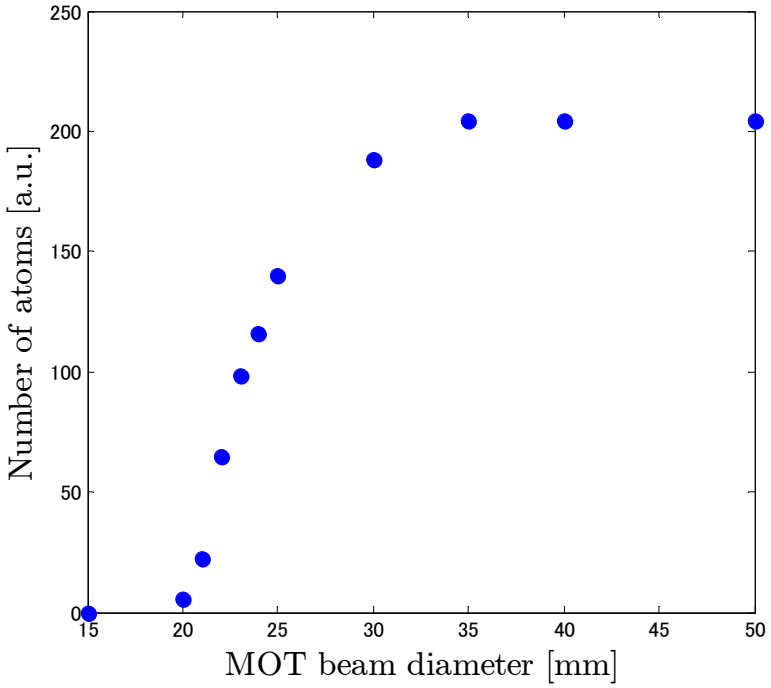

Fig.4.4 Number of atoms against the beam diameter of the MOT light

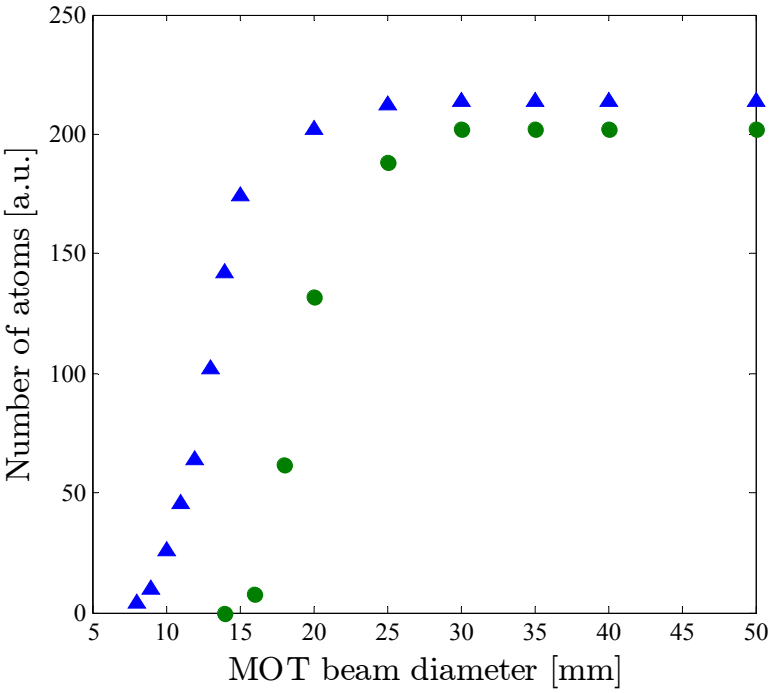

Fig.4.5 Number of atoms against the diameter of the MOT beam
Green circle points indicate the decelerating beam is modified and blue triangle points indicate the beam not relevant to deceleration is modified.

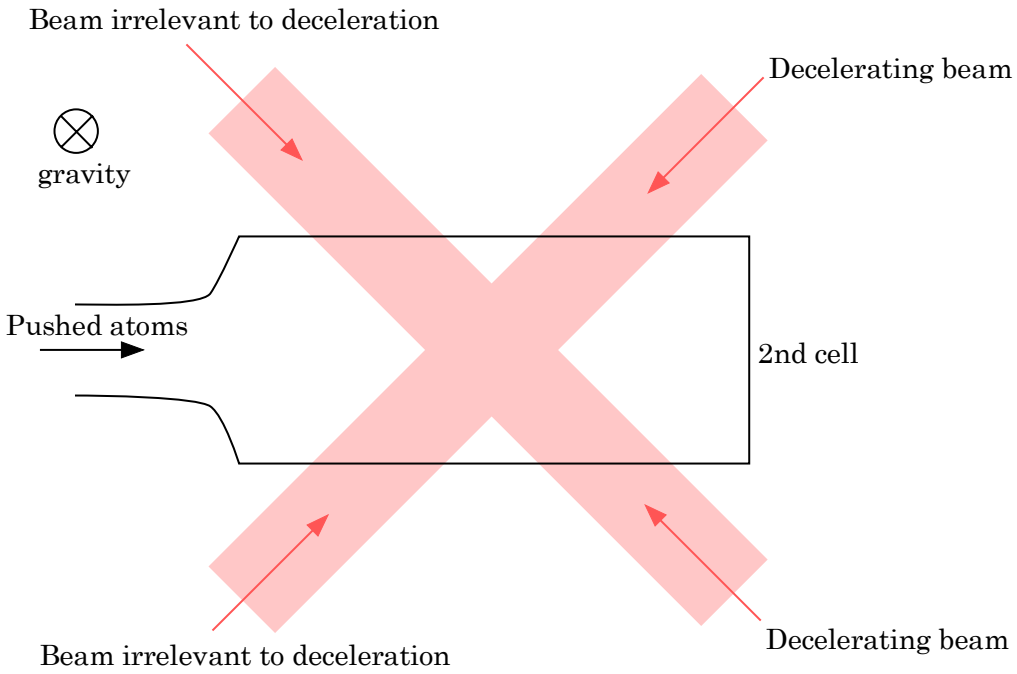

Fig.4.6 Experimental configuration of figure 4.5

The two left beams are not relevant to deceleration of pushed atoms, while two right beams contribute to deceleration. Figure 4.5 shows the beam diameter of the right beams is important to efficiently catch atoms.

Figure 4.4 shows that the beam diameter of around 30mm is sufficient to capture atoms at the 2nd MOT. We can confirm from Figure 4.5 that this minimum diameter is mainly determined by the decelerating beam, and thus other 4 beams could have a smaller diameter around 15mm.

4.1.3 Efficiency of transferring atoms

We have performed detailed investigations on a double MOT configuration of potassium atoms since there are so far limited reports on it. Here the problem is that atoms confined in a MOT have comparatively high temperature around mille Kelvin as reported in [61]. This reduces the efficiency of transferring atoms from the 1st MOT to the 2nd MOT since the atomic beam spread out at the 2nd MOT if the transverse temperature of the atomic beam is high. Actually they reported that a temporal cooling process at the 1st MOT before transfer improves the transfer efficiency by one order. It is noteworthy that we first tried continuous pushing scheme which gave a reasonable efficiency, while Prevedelli et al. mentioned that pulsed pushing is more efficient than continuous one. We have also tried pulsed pushing but it did not give a good result. Our difference from them probably lies in the focus point of the push beam: we usually focus the push beam to the center of the 1st MOT, while they focus it to the center of the 2nd MOT.

We first define a loading rate L of a MOT as follows:

$$L = \frac{N}{T}$$

where N denotes a final number of atoms in the MOT and T denotes the exponential time constant of the MOT loading. This value is later used as a measure of the efficiency of capturing atoms both in the 1st MOT and 2nd MOT. In the case of the 2nd MOT, it also represents the flux of atomic beam from the 1st MOT if we assume all the pushed atoms are captured at the 2nd MOT.

We have evaluated the velocity of atoms pushed by a resonant laser under various conditions. This is

accomplished by measuring a time lag between the time at which the push beam is turned on and the time at which number of atoms in the 2nd MOT begins to increase. Dividing the length between the 1st MOT and the 2nd MOT by the time lag, we can know the velocity of the fastest atoms directly. Figure 4.7 shows a typical result obtained in this way.

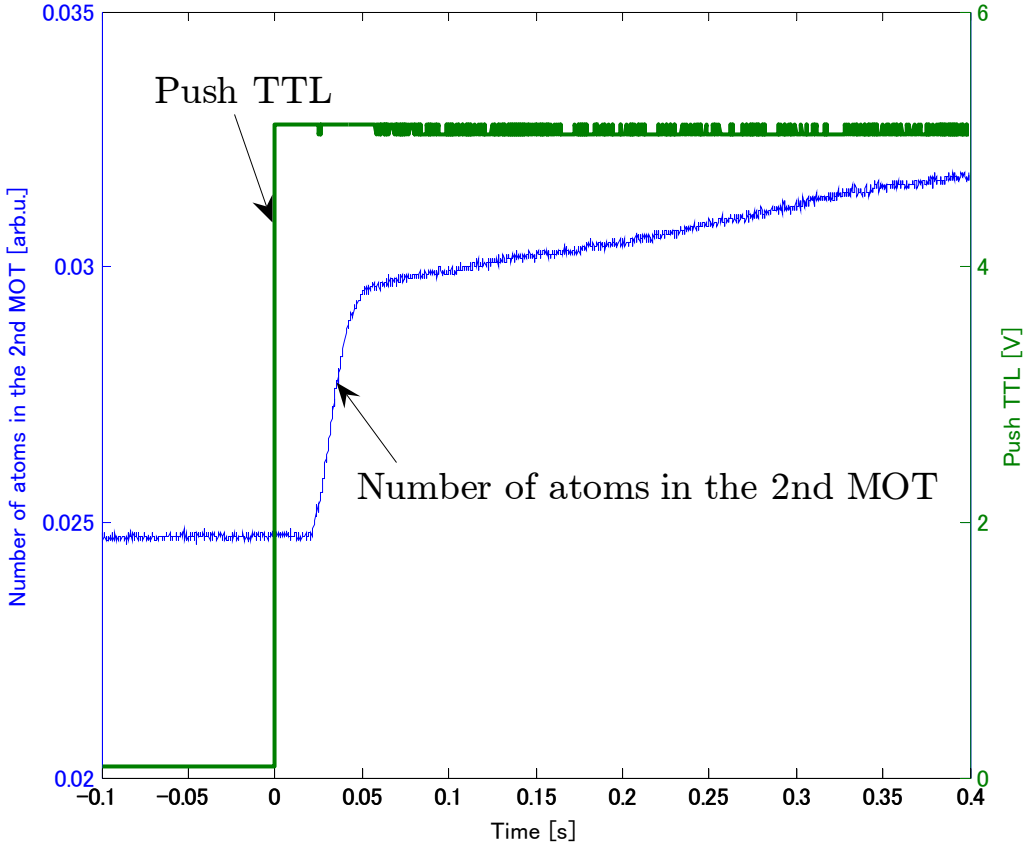

Fig.4.7 Typical result of the velocity measurement
There is a time lag between the time the push beam is turned on and the time number of atoms begins to increase.

Using the above method, we measured the velocity of atoms and the loading rate of the 2nd MOT against the power and the detuning of the push beam both for a colinear push beam and a focused push beam at the 1st MOT. Here we have employed repumping light as a push beam and not trapping light, since trapping light did not give an efficient transfer. Figure 4.8 and 4.9 show the detuning dependency and power dependency of the velocity and the loading rate for a colinear beam whose diameter is 2mm, respectively.

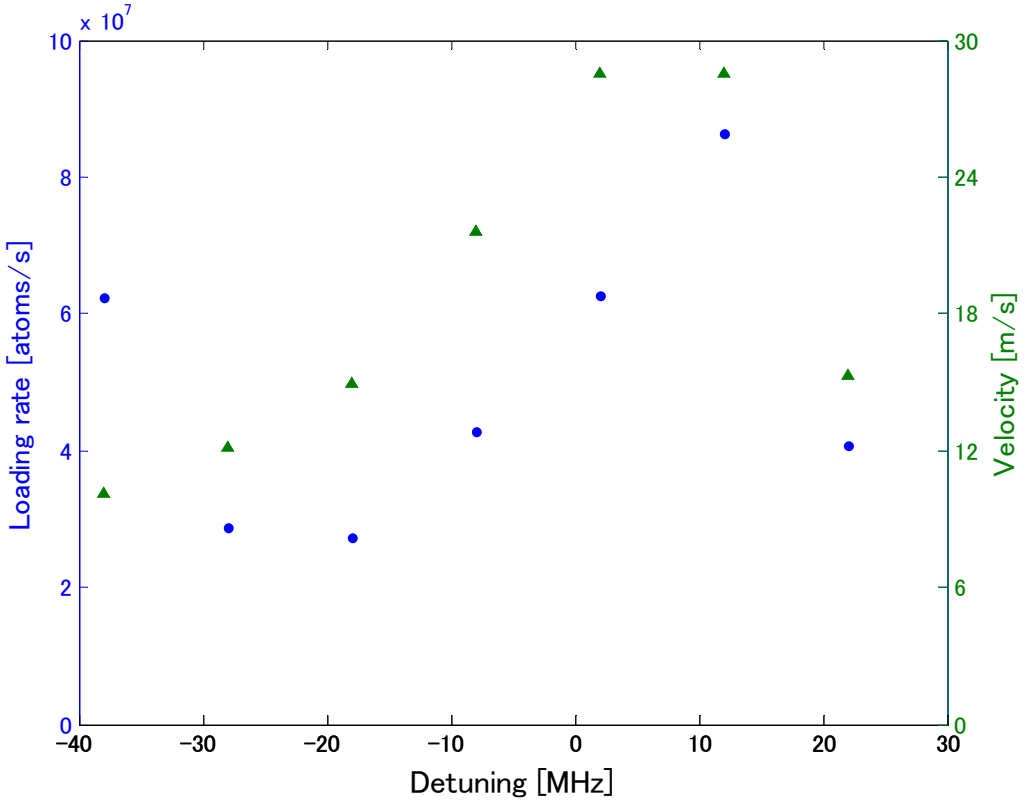

Fig.4.8 Velocity of pushed atoms (green triangles) and loading rate at the 2nd MOT against detuning of push beam (blue circles)

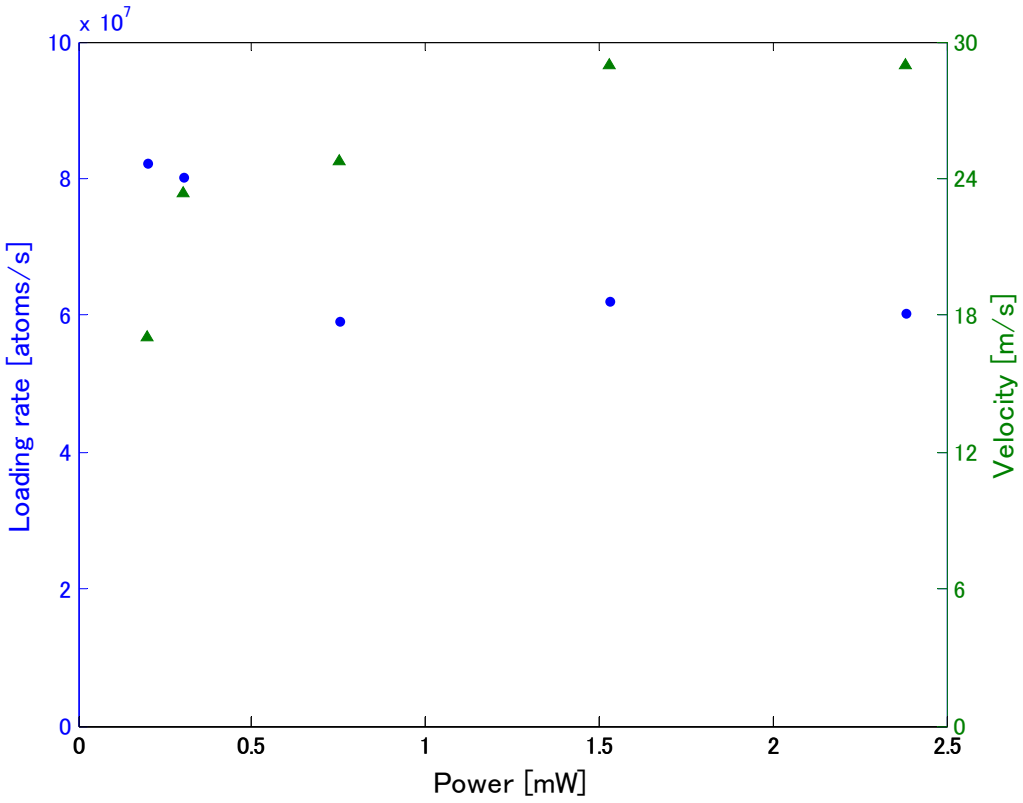

Fig.4.9 Velocity of pushed atoms (green triangles) and loading rate at the 2nd MOT against power of push beam (blue circles)

We can see following three things from these figures:

1. There is a general tendency that a nearly resonant push beam leads to a low loading rate, while there is a peak at a few tens of MHz detuning both to the red and to the blue. It is important that the peaks move toward a large detuning as the power increases. These facts can be interpreted as follows. A resonant light breaks the balance of the MOT light and thus reduces number of atoms and density in the 1st MOT, which leads to a low flux. If you detune the push beam from the resonance, number of atoms and density recovers. In this case, power broadening due to the high intensity of the push beam allows atoms in the MOT to be accelerated by absorbing the push beam. This is easily confirmed by considering the actual value of the power broadening. We can see that the peak shifts by about 10MHz when the power is increased from 1.28mW and to 2.75mW. These two values of the beam power correspond to around $24I_s$ and $52I_s$, respectively. These values give the difference of about 7MHz, which is consistent with the observed shift.
2. A loading rate increases as the velocity of the atoms increases except the push power is too low. This is because the transverse spread of the atoms at the 2nd MOT is small when they get there. Too low power of the push beam leads to a high loading rate due to its small effect on the beam balance of the MOT light.
3. A blue detuned light gives higher velocity and loading rate than a red detuned light. This is easily understood as follows. If a red detuned light is shone to the atoms, they are accelerated to become off resonance due to their Doppler shift. However, accelerated atoms become close to the resonance in the case of a blue detuned light. Thus a blue detuned light can push atoms more than a red detuned light. Here the acceleration stops when atoms come out of the MOT light and undergo hyperfine pumping to the F=2 state by the push beam which did not affect F=2 atoms.

The conclusion from the above arguments is that a light detuned to the blue by about 40MHz with the power of around 3mW is the best for a colinear push beam.

Next the results of the similar experiment for a focused beam whose diameter is 0.15mm at the 1st MOT is presented. Figure 4.10 and 4.11 show the detuning dependency and power dependency of the velocity and the loading rate, respectively, while figure 4.12 shows the detuning dependency of the loading rate for two different values of the beam power.

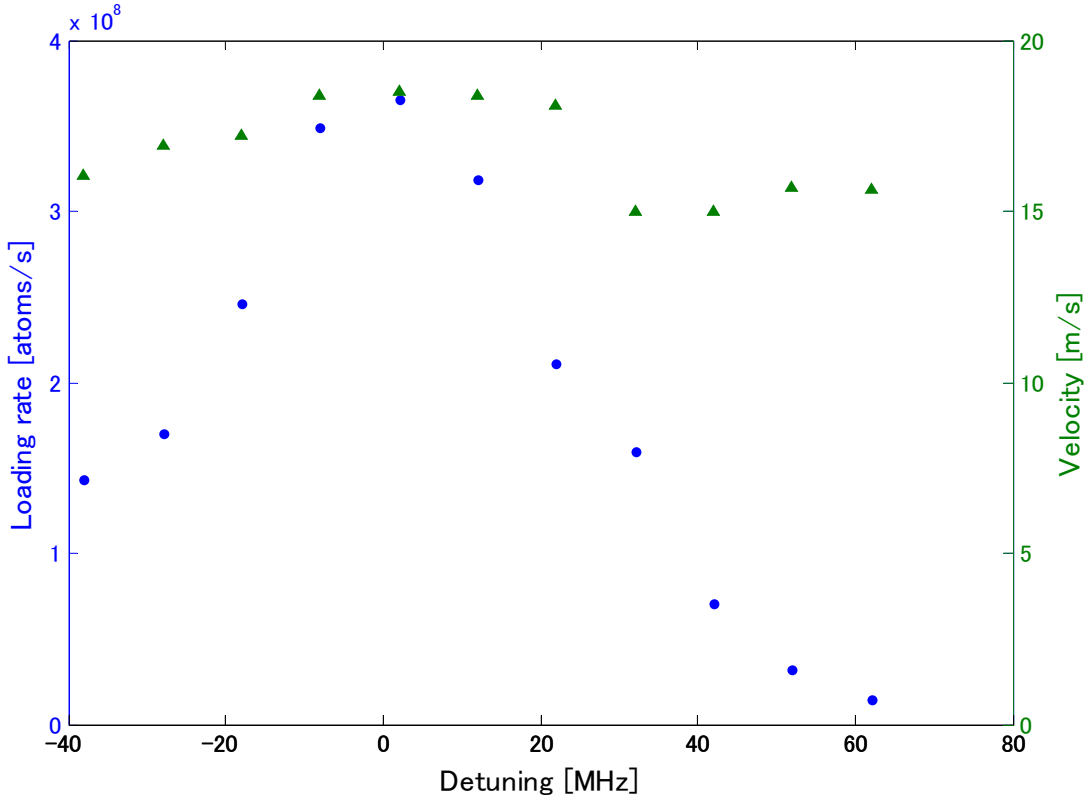

Fig.4.10 Velocity of pushed atoms and loading rate at the 2nd MOT against detuning of push beam Here the push beam is focused to the 1st MOT. The power of push beam is kept to be 0.5mW.

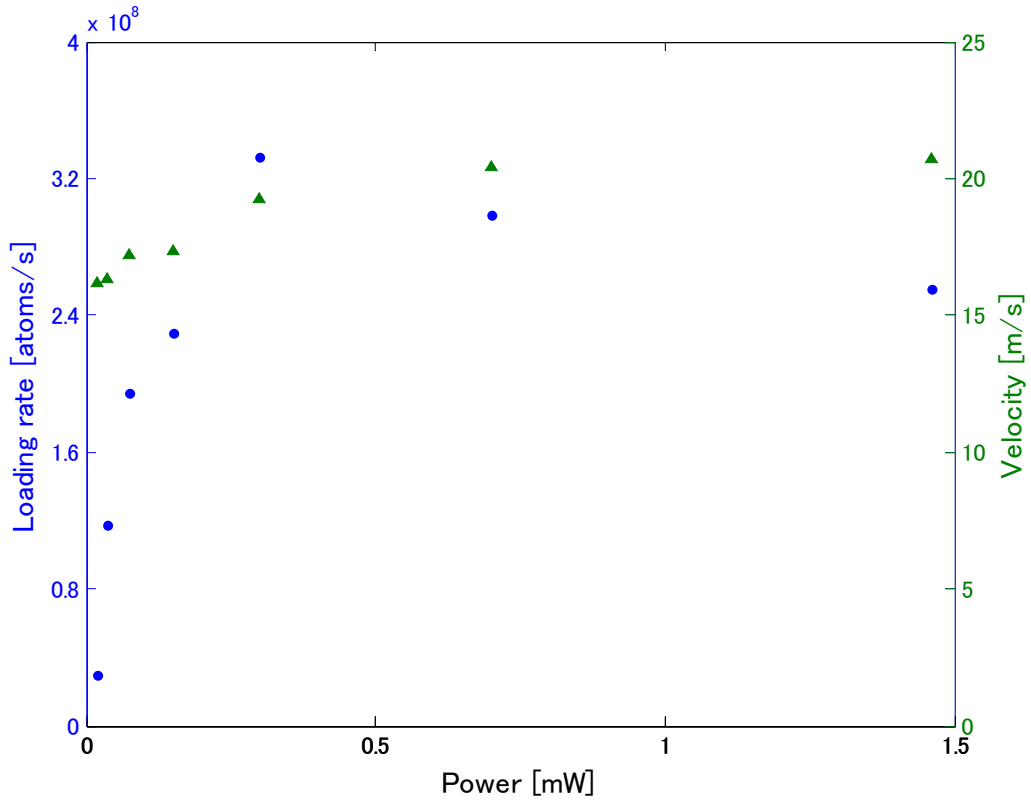

Fig.4.11 Velocity of pushed atoms and loading rate at the 2nd MOT against power of push beam Here the push beam is focused to the 1st MOT. The detuning of the push beam is

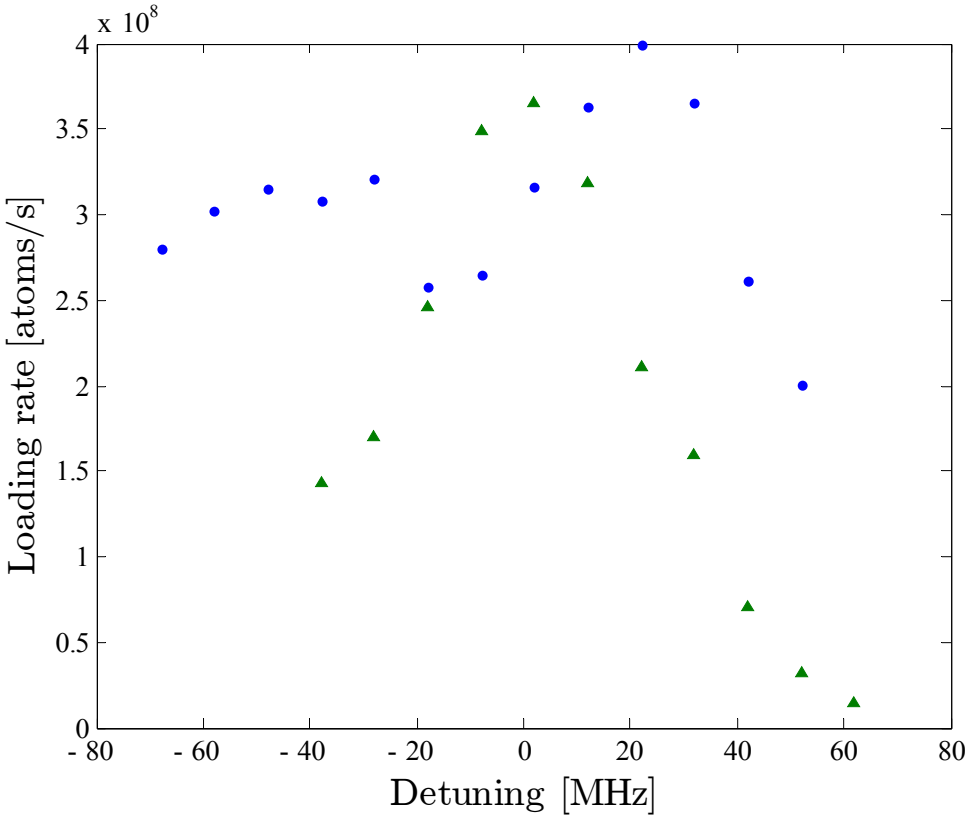

Fig.4.12 Dependence of loading rates on detuning for two different powers
Green triangles and blue circles indicate the beam power of 0.5mW and 2.0mW, respectively.

Though a tendency similar to the previous result is observed, the observed values are different from the previous results: the loading rate is higher and the velocity is lower. The low velocity seems to suggest that atoms are moving in the transverse direction when they are accelerated, and thus higher velocity is obtained with the larger diameter of the push beam. The high loading rate is due to its small effect on the balance of the MOT light.

Based on the above results, we have decided to adopt a focused beam for pushing atoms. We use a blue detuned light by 20MHz with a moderate power around 2mW for later experiments. The polarization of the push beam did not cause a significant change in the above results.

Here we define another nondimentional index which represents the efficiency of pushing atoms:

$$P = L_2 / L_1$$

where L_1 and L_2 denotes the loading rate of the 1st MOT and the 2nd MOT, respectively. If this value reaches unit, all the atoms collected at the 1st MOT are transferred and captured at the 2nd MOT. Of course, this situation is unreal and the P value is usually ranged in 0.1~0.4. Since it also reflects the alignment of the push beam, hereafter we have used this factor as an index of the efficiency of the push beam. Figure 4.13 shows the linearity of L_1 and L_2 against the loading rate of the 1st MOT. Here the alignment of the push beam was kept unchanged and only the amount of the background potassium atoms was changed by increasing the dispenser current.

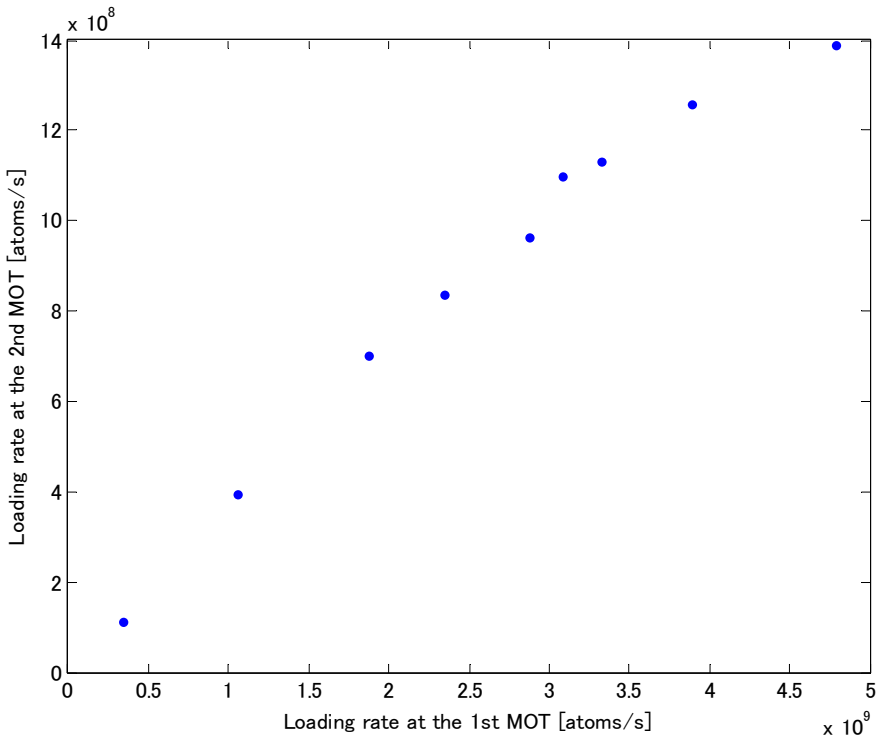

Fig.4.13 Comparison of the loading rates at the 1st and 2nd MOT
The slope gives the efficiency of pushing atoms. The efficiency depends on alignment, power and detuning of the push beam. Here the slope is kept constant around 0.3 over wide range.

We checked the dependence of P on the push beam diameter as shown in the figure 4.14. We can see that smaller diameter is advantageous. We employed the diameter of 0.35mm for later experiments.

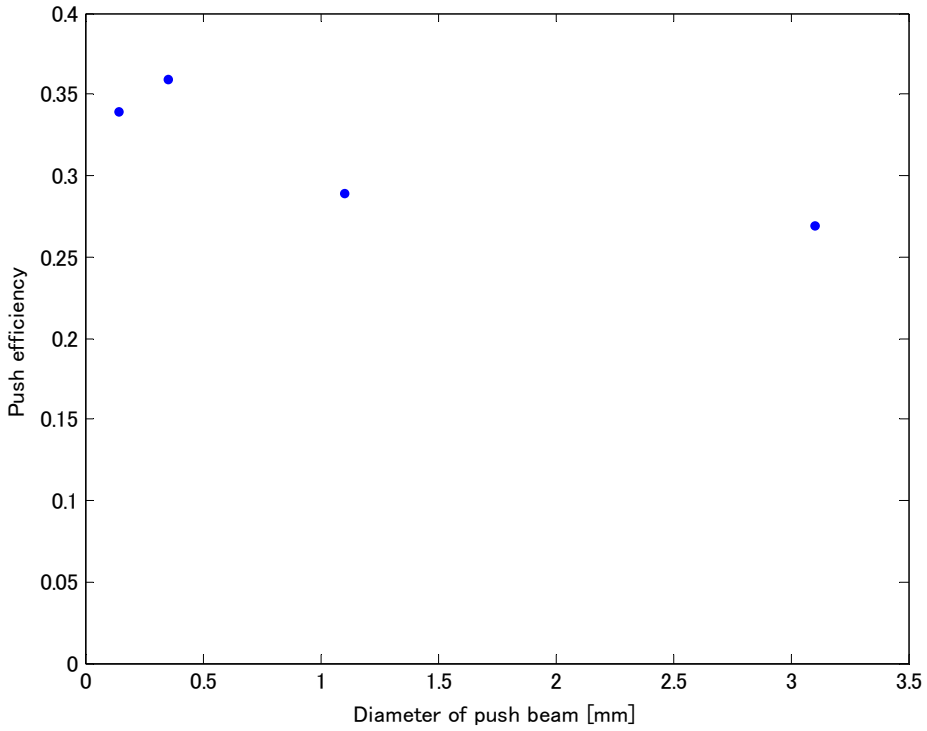

Fig.4.14 Push efficiency against the diameter of push beam at the 1st MOT

Next we investigated the transverse distribution of the pushed atoms, which is important for designing the differential pumping tube inserted between the 1st MOT and the 2nd MOT. The differential tube should have a smaller diameter for obtaining a higher vacuum at the 2nd MOT, though it might limit the number of atoms captured at the 2nd MOT if the spread of the atomic beam is comparable to the inner diameter of the tube. Thus it was necessary to measure the spatial profile of pushed atoms, which is performed with a configuration illustrated in figure 4.15.

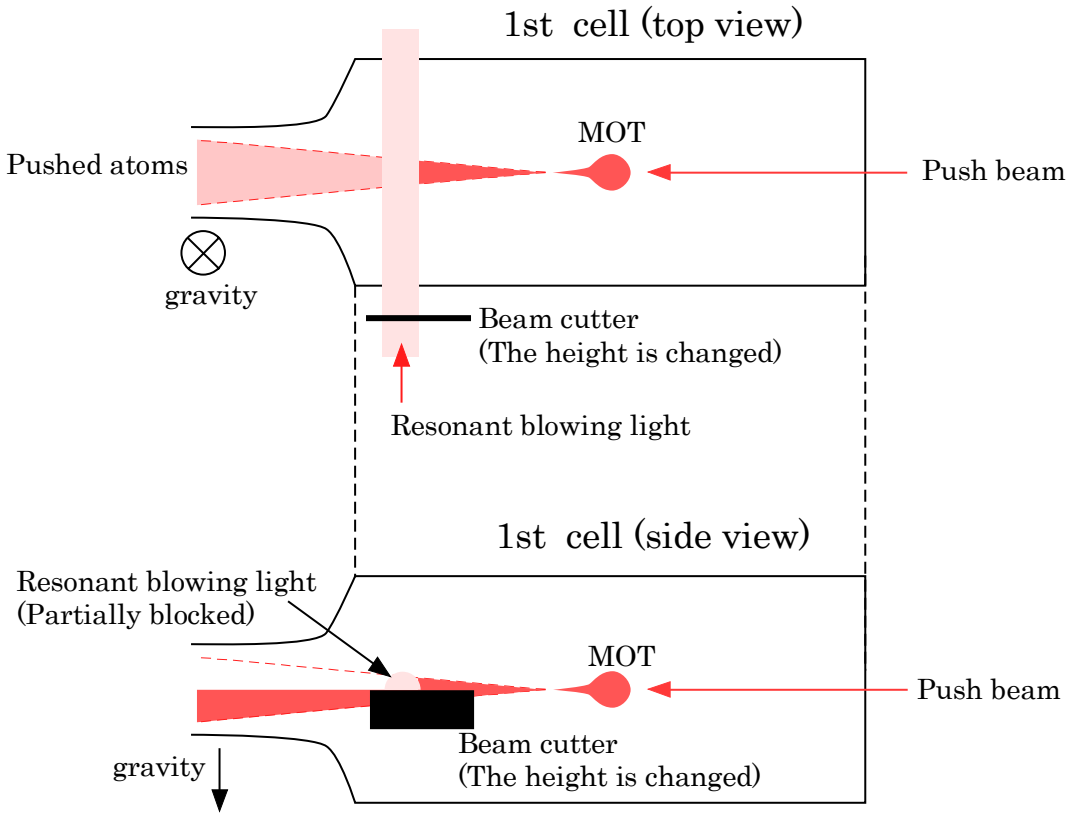

Fig.4.15 Configuration to measure the spatial distribution of pushed atoms
The beam cutter blocks a part of the blowing light. Only atoms which pass through the region where blowing light does not exist can reach the 2nd cell. Thus number of atoms captured at the 2nd MOT reflects the atomic flux in the blocked region. Changing the height of the beam cutter, the spatial distribution is obtained.

First pushed atoms are completely blown out by a resonant beam which has a large diameter of around 15mm. At this time, there are no atoms in the 2nd MOT. Then a part of the blowing beam is blocked by a black paper. This enables atoms which pass through the region where the blowing beam is absent to reach the 2nd MOT. Measuring the number of atoms in the 2nd MOT yields the integrated distribution of the pushed atoms. Actually we block the atomic beam by blocking the lower side of the blowing beam. Figure 4.16 shows the measured results of the number of atoms collected in the 2nd MOT when the height of the blocking paper is gradually increased. We performed experiments at two different distances near the 1st MOT, as there is no window to introduce the blowing beam near the tube. From the two observed distribution, we can estimate the transverse spread of the atoms.

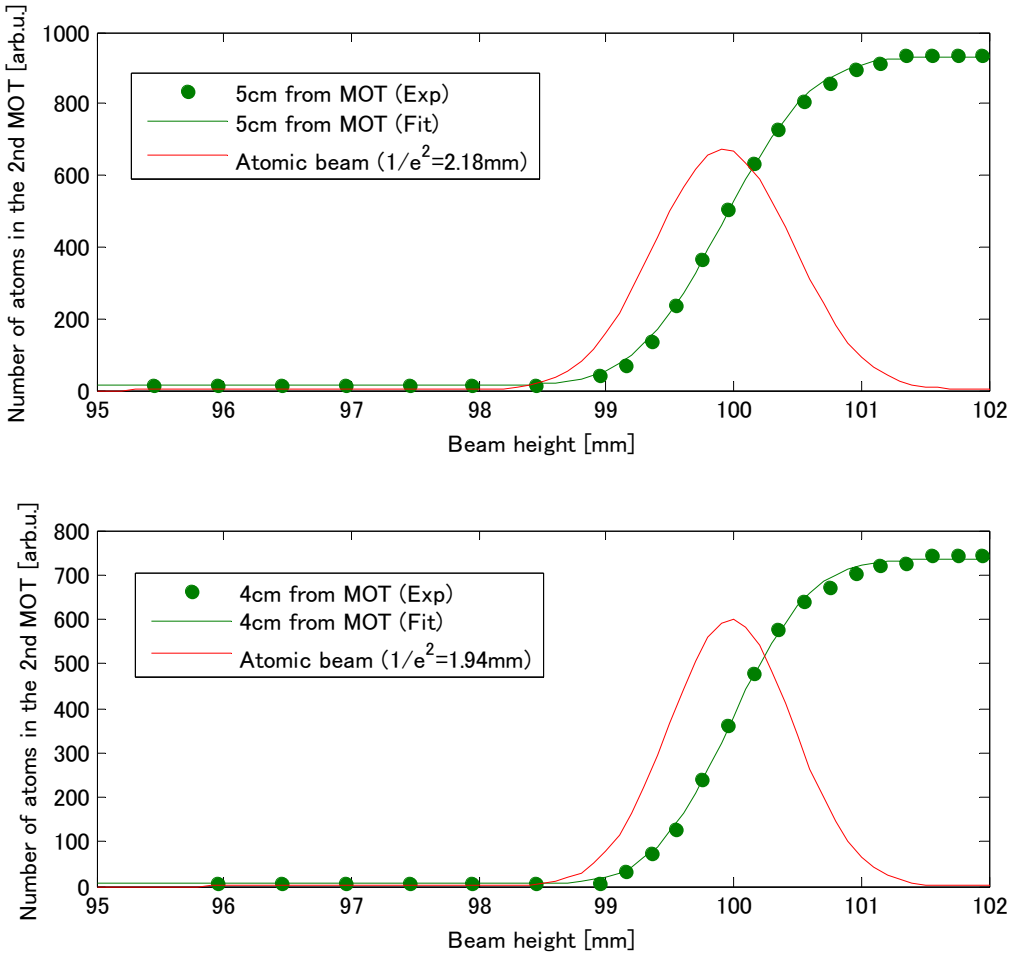

Fig.4.16 Measured and fitted spatial distribution of pushed atoms

If we assume a Gaussian distribution for pushed atoms, the resulting curve is an error function. We fitted the experimental results with an error function and obtained the width of $1/e^2$ radius of atomic beam. Since the experiments are performed for the two different distances from the 1st MOT, the transverse temperature of atoms could be estimated from the difference in the width. We deduced it as around 230 μK, which is consistent with the temperature of an ordinary MOT. However, it is not consistent with [61]. They reported that the temperature of the 1st MOT of ^{39}K exceeds 1mK, and thus a temporal cooling is effective to improve the flux of atoms. We have not yet ascertain this unexpected low transverse temperature, but there is a possibility that atoms are cooled at the low intensity region of the MOT light when they are accelerated.

The above results enable us to estimate the width of the atomic beam at the 2nd MOT to be around 15mm. Based on these values, we determine the diameter of the differential pumping tube and the size of the 2nd cell.

4.2 Laser cooling of ^{41}K at E1

4.2.1 Number of atoms measured with fluorescence

We have measured number of atoms in the MOT of ^{41}K against frequency of MOT light, intensity of MOT light, magnetic field gradient and frequency of the push beam as done for ^{39}K. The results are shown in figure 4.17 to 4.20. We measured only frequency dependence for the 1st MOT. All parameters related to the 1st MOT are optimized to have a large number of atoms in the 2nd MOT. Though there are no detailed measurements, the maximum push efficiency obtained is around 0.1, which is much lower than the case for ^{39}K. This seems to indicate that the transverse temperature of pushed atoms of ^{41}K is higher than that of ^{39}K.

In the frequency measurements, we can see a similar tendency as previously observed for ^{39}K. There is a peak where number of atoms is large. This frequency again corresponds to a Raman condition where the trapping and repumping light hit the same energy level.

The main difference from the previous ^{39}K experiments lies in the intensity dependence of number of atoms. Figure 4.19 shows higher intensity leads to larger number of atoms even at the highest intensity. This behavior is quite different from that of ^{39}K, where maximum number of atoms is obtained at low intensity. This suggests that the velocity capture range of ^{41}K is small compared to that of ^{39}K. We consider that it is a result of a higher hyperfine pumping rate between the ground state F=1 and F=2 due to even smaller hyperfine splitting of the excited states of ^{41}K compared to ^{39}K.

The subsequent figures are used to optimize number of atoms in the 2nd MOT. These results for ^{41}K show nearly the same tendency to ^{39}K. The optimum magnetic field gradient which gives maximum number of atoms largely depends on the optical alignment. A better alignment leads to shift the peak of number of atoms to lower magnetic field gradient. Typical our value of magnetic field gradient is 10G/cm for the 1st MOT, whereas as low as 3G/cm for the 2nd MOT.

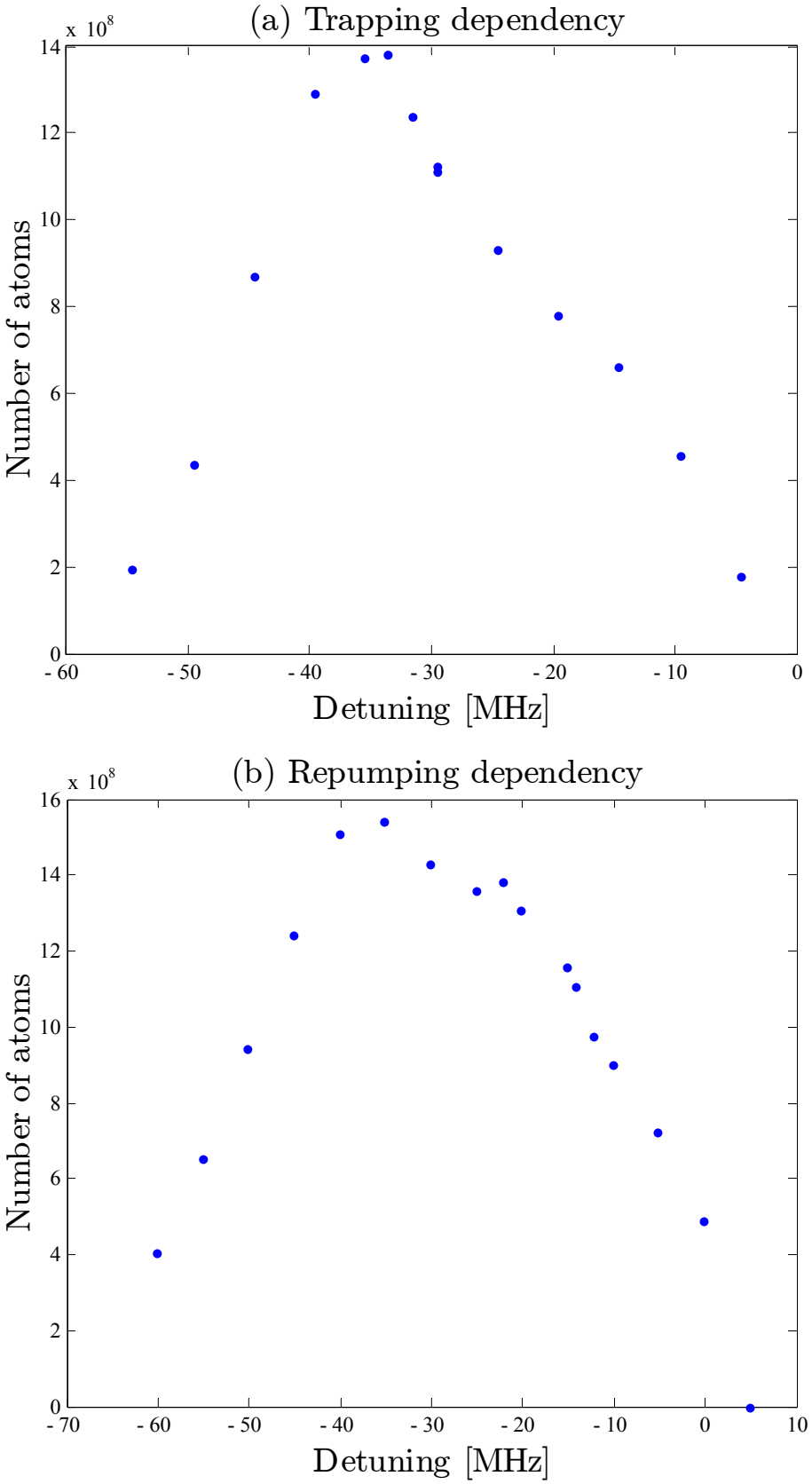

Fig.4.17 Number of atoms in the 1st MOT against detuning of (a) trapping (b) repumping The repumping frequency is fixed at a detuning of -22MHz in (a) while the trapping frequency is fixed at a detuning of -32MHz in (b).

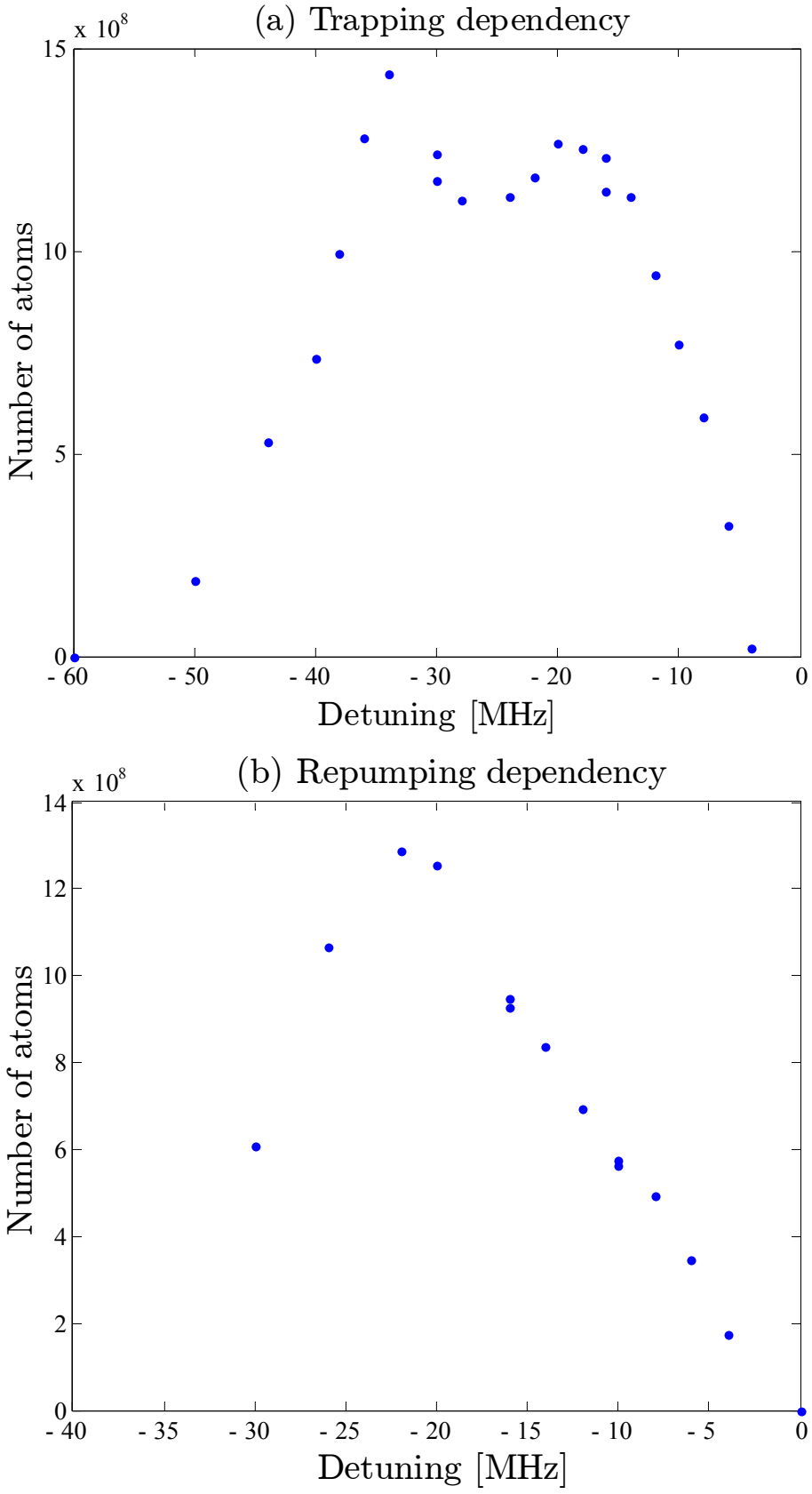

Fig.4.18 Number of atoms in the 2nd MOT against detuning of (a) trapping (b) repumping The repumping frequency is fixed at a detuning of -20MHz in (a) while the trapping frequency is fixed at a detuning of -16MHz in (b).

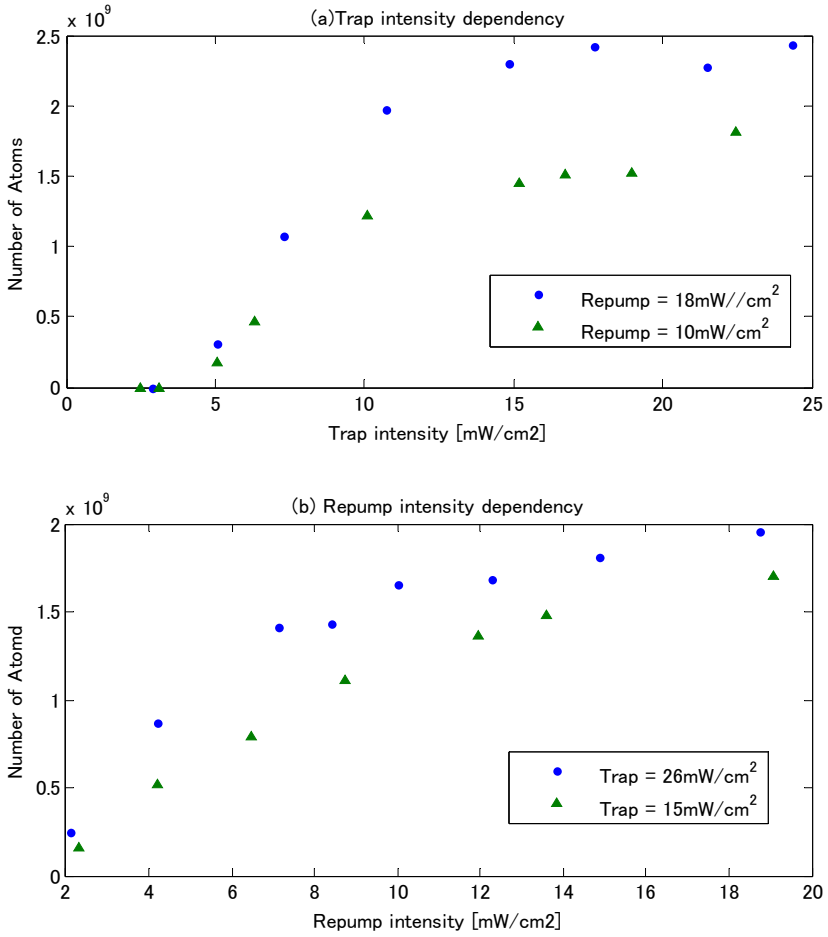

Fig.4.19 Number of atoms in the 2nd MOT against intensity of (a) trapping (b) repumping

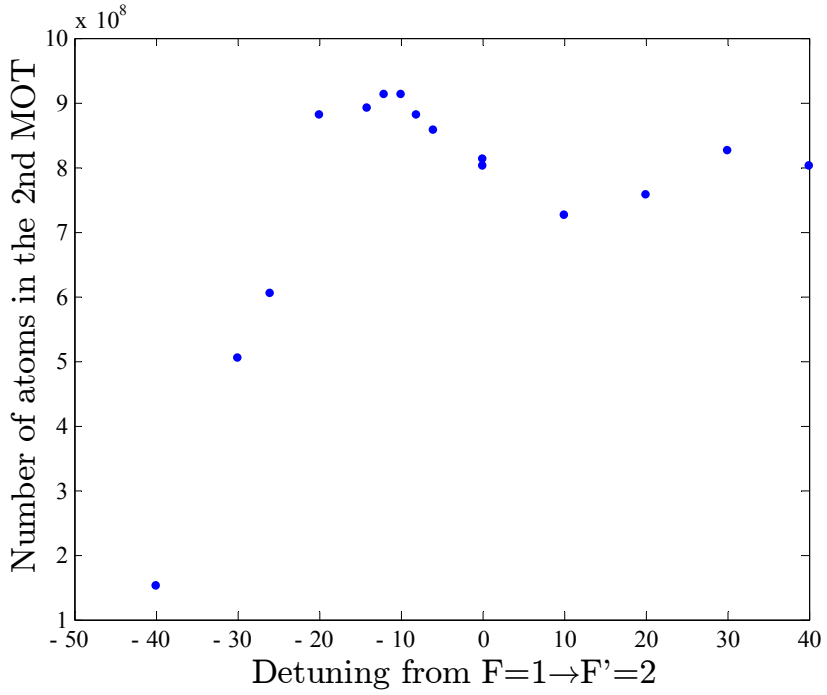

Fig.4.20 Number of atoms in the 2nd MOT plotted against detuning of push beam
Here number of atoms in the 2nd MOT reflects the atomic flux from the 1st MOT.

4.2.2 Characterization with absorption imaging

For subsequent experiments, we required data on the temperature and density of atomic clouds as well as number. We utilized an absorption imaging to measure these properties. It is noteworthy that the measurements of temperature and density with the fluorescence image of a MOT focused to the CCD did not give a good result, since it required shining MOT lasers to the atomic clouds intense enough to record an image on the CCD. In our setup, this process has an effect on the atomic cloud: the laser necessary to obtain a fluorescence image inevitably cools and confines atoms. Thus we did not use the fluorescence imaging in the later experiments.

As a preparation, we have checked the resonance of the cycling transition F=2→F'=3 for a correct imaging. OD is measured against the frequency of the probe beam and shown in figure 4.21. The width of the peak well coincides with the atomic natural width, which means that our imaging is correct. The fitted center of the peak is defined to be the resonance and used in the later experiments.

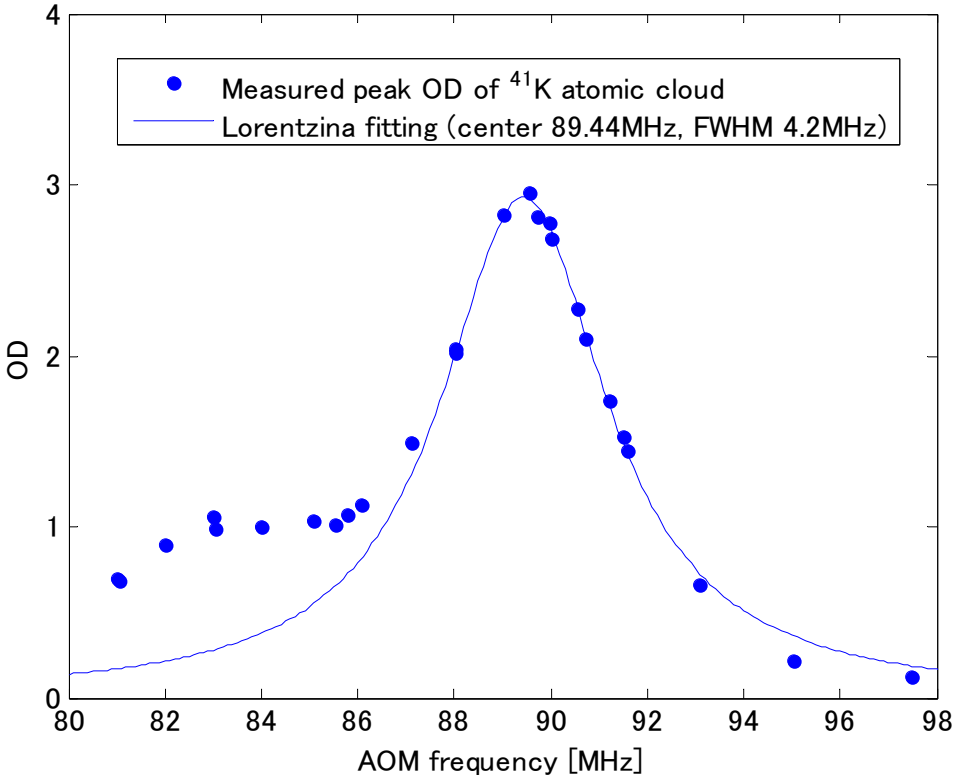

Fig.4.21 Optical depth against probe frequency
The resonant frequency is obtained by fitting the absorption spectrum with Lorenzian shape. The small peak near 83MHz corresponds to F=2→F'=1,2 transition.

We investigated the properties of the ^{41}K MOT in the steady state since temperature seemed to be too high and the density seemed to be too low. The results are shown in figure 4.22 to 4.25. In any condition, the temperature is very high compared to other atomic species, while the density is very low. The resulting phase space density of the order of 10^{-10} is much lower than other species by more than three orders. This means that ^{41}K is not suitable for a condensate experiment, as it needs a high phase space density at the stage of laser cooling to reach quantum degeneracy.

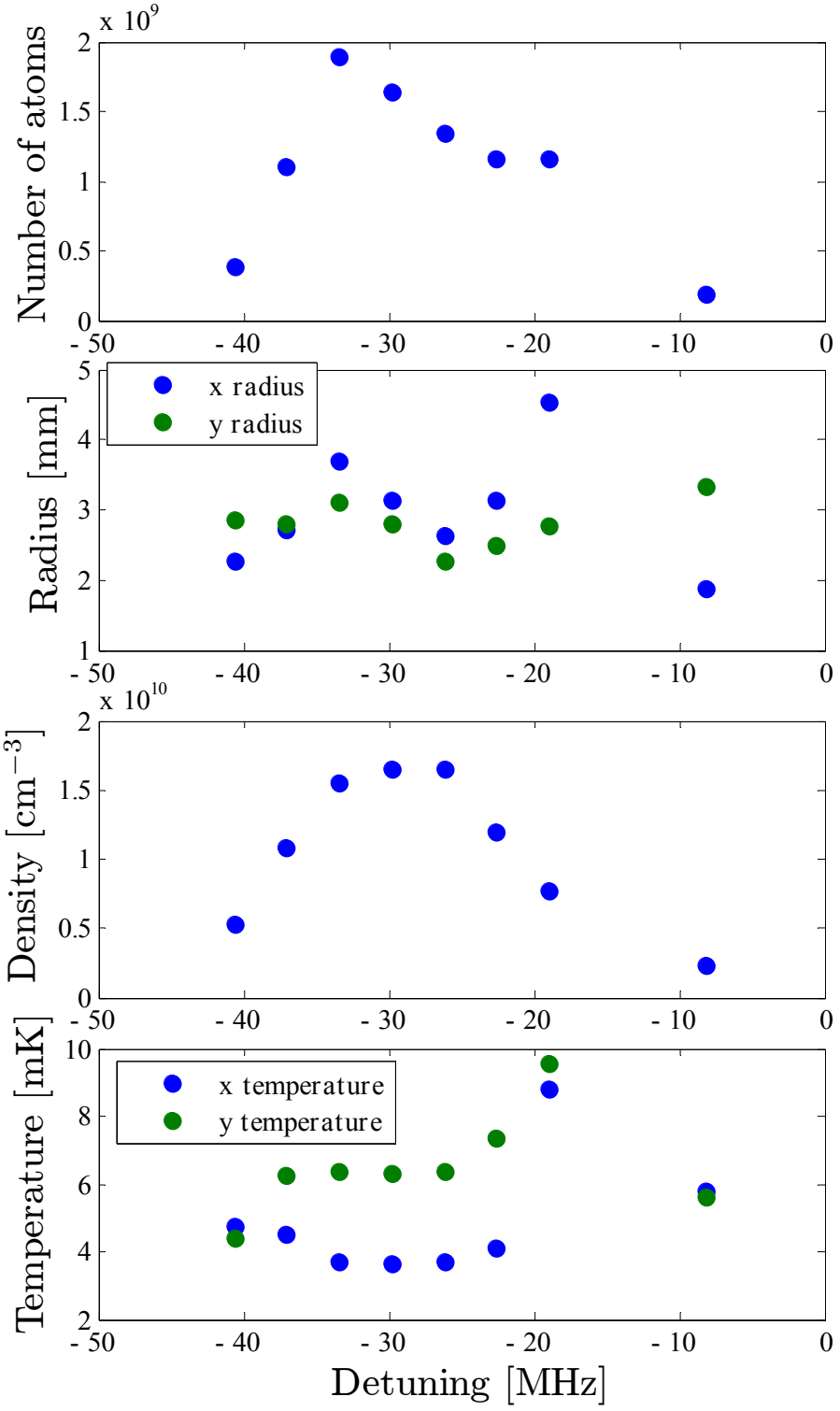

Fig.4.22 Number, radius, density and temperature of atoms against trapping detuning

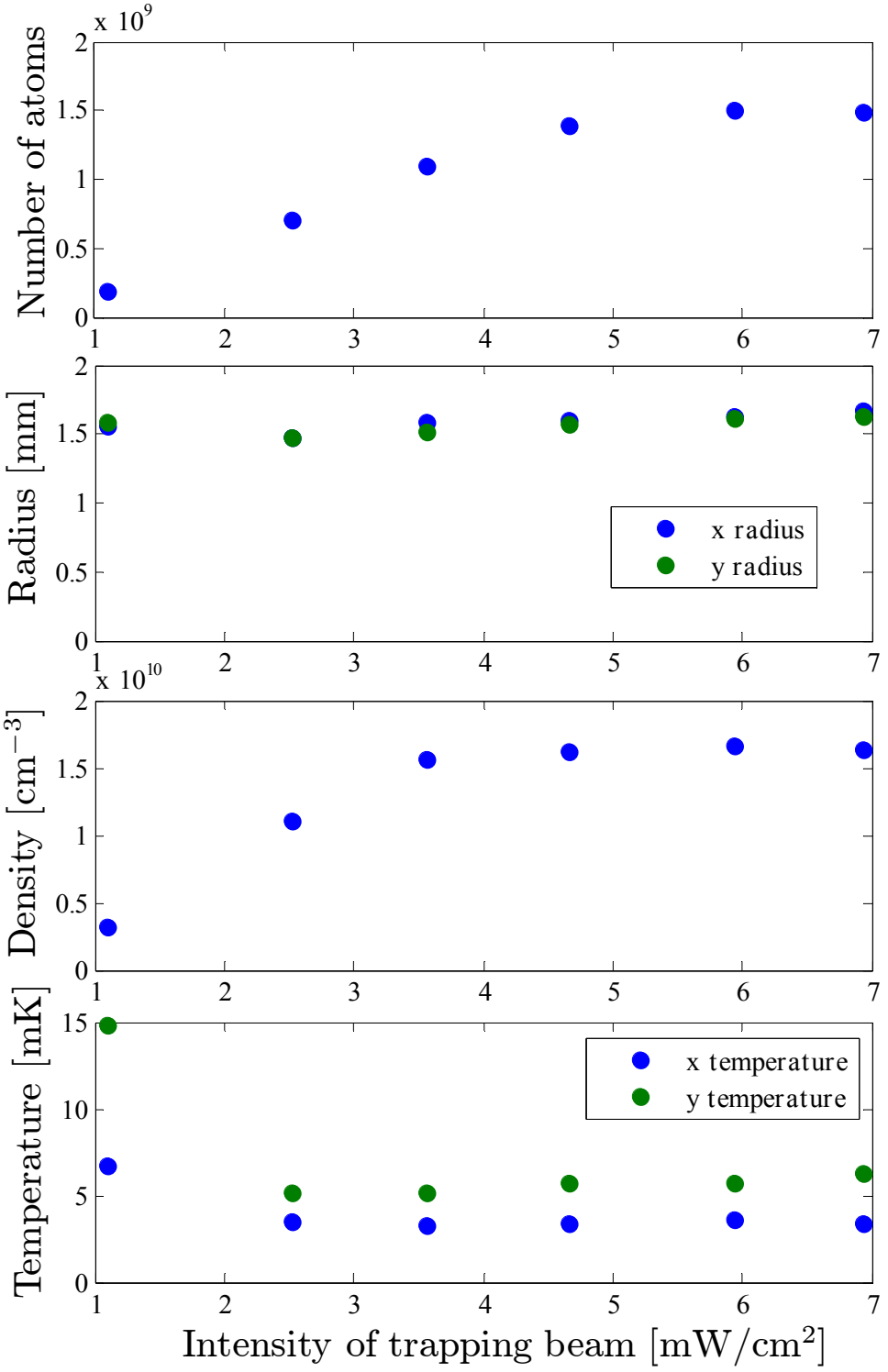

Fig.4.23 Number, radius, density and temperature of atoms against trapping intensity

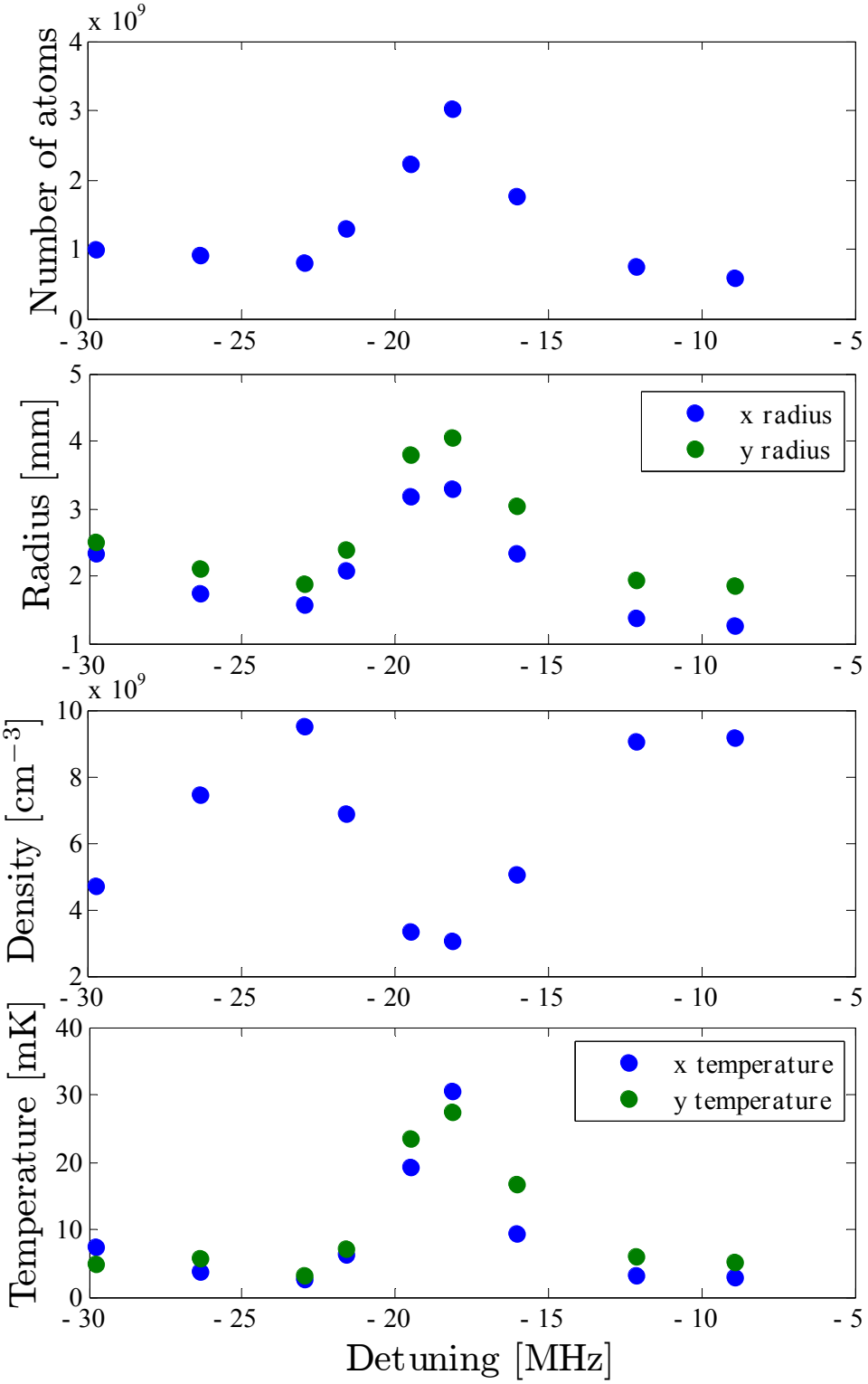

Fig.4.24 Number, radius, density and temperature of atoms against repumping detuning

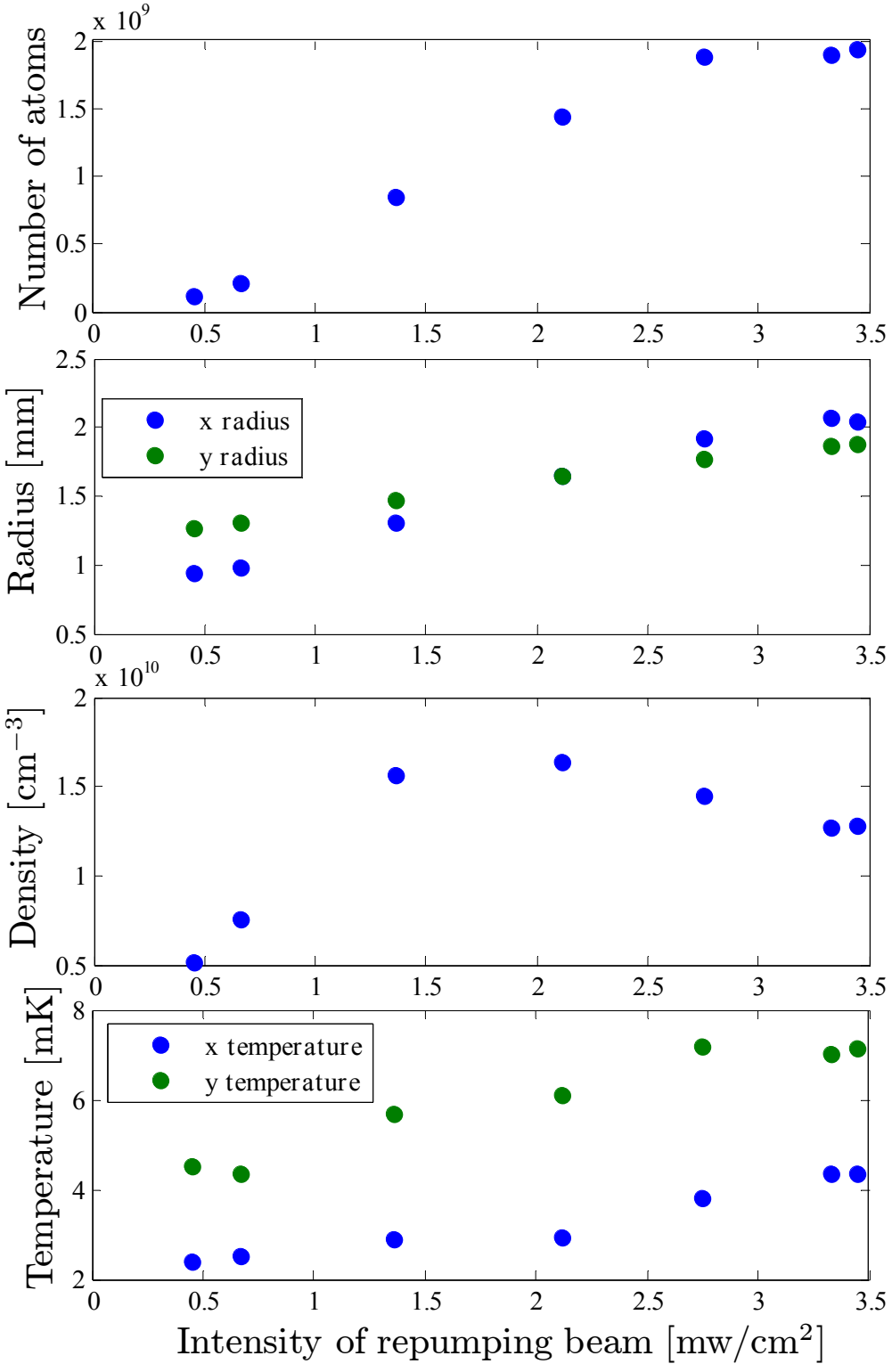

Fig.4.25 Number, radius, density and temperature of atoms against repumping intensity

The notable feature observed in the frequency experiments is the peak ranged in the repumping detuning of around 20MHz and trapping detuning of around 20MHz. Here the temperature exceeds 10mK and the density reaches down to around $10^9/cm^3$, while nearly tripled number of atoms is obtained compared to a normal condition. There are no atomic energy levels in this frequency range. As already mentioned above, this resulted from a Raman condition of the trapping and repumping laser. In practice, the peak in the experiment on the

detuning of trapping laser shifts when the detuning of repumping laser is shifted, and vice versa. An example of the image of atomic clouds at the Raman condition and at the normal condition is shown in figure 4.26. We can see that density at the center of the MOT is low at the Raman condition, which is quite a peculiar behavior among other atomic species.

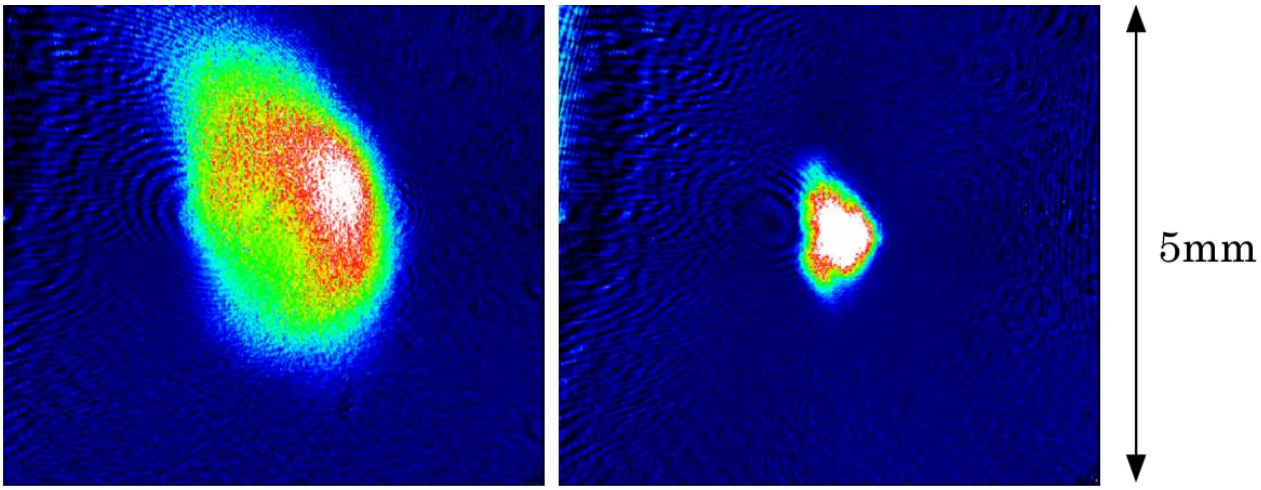

Fig.4.26 Images of atoms at Raman condition (left) and non-Raman condition (right)
These images are taken at the same condition except for the frequency of repumping light. It is clearly seen that atoms tend to escape from the center of the MOT at Raman condition.

We have tried to use this resonance to enhance number of atoms, but it leads to too high temperature and too low density which cannot be compensated in the subsequent experimental stage. Thus we decided to employ a non-Raman condition to obtain a higher phase space density. With this selection of the frequency, we can improve the phase space density by one order at the cost of number of atoms. The intensity of each beam is kept to be the maximum value as it is not so sensitive to the various properties of the MOT.

4.2.3 Time dependent MOT

The above results show that ^{41}K cannot be used for the subsequent condensate experiments directly since it is impossible to catch hot and low density atoms efficiently by another trap such as a magnetic trap or an optical trap. Thus we tried a time dependent MOT which is originally developed for Rb atoms and investigated for ^{39}K and ^{41}K atoms [61].

Our scheme consists of two stages: first atoms are compressed by raising the magnetic field gradient and then cooled by changing the detuning of both trapping and repumping laser close to the resonance and lowering the intensity of both trapping and repumping laser.

Optimization of each stage is carried out by changing one of the many parameters (intensity, frequency and magnetic field gradient) to obtain a higher phase space density one by one. Thus we achieved an improvement in the phase space density by two orders. Figure 4.27 shows experimental time sequence for the achieved best condition. Figure 4.28 shows comparison of images between the steady state MOT and time dependent MOT for different time of flight. We can clearly see the effect of compression and cooling: images with 0.1ms TOF show original density distributions while images with 3ms include thermal expansion. The condition of atoms at each step including the steady state and the Raman condition is shown in the table 4.1.

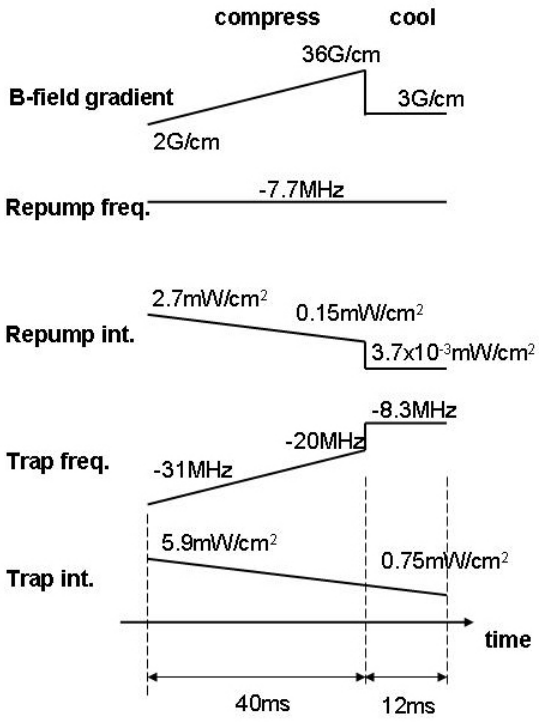

Fig.4.27 Experimental time sequences of TDMOT

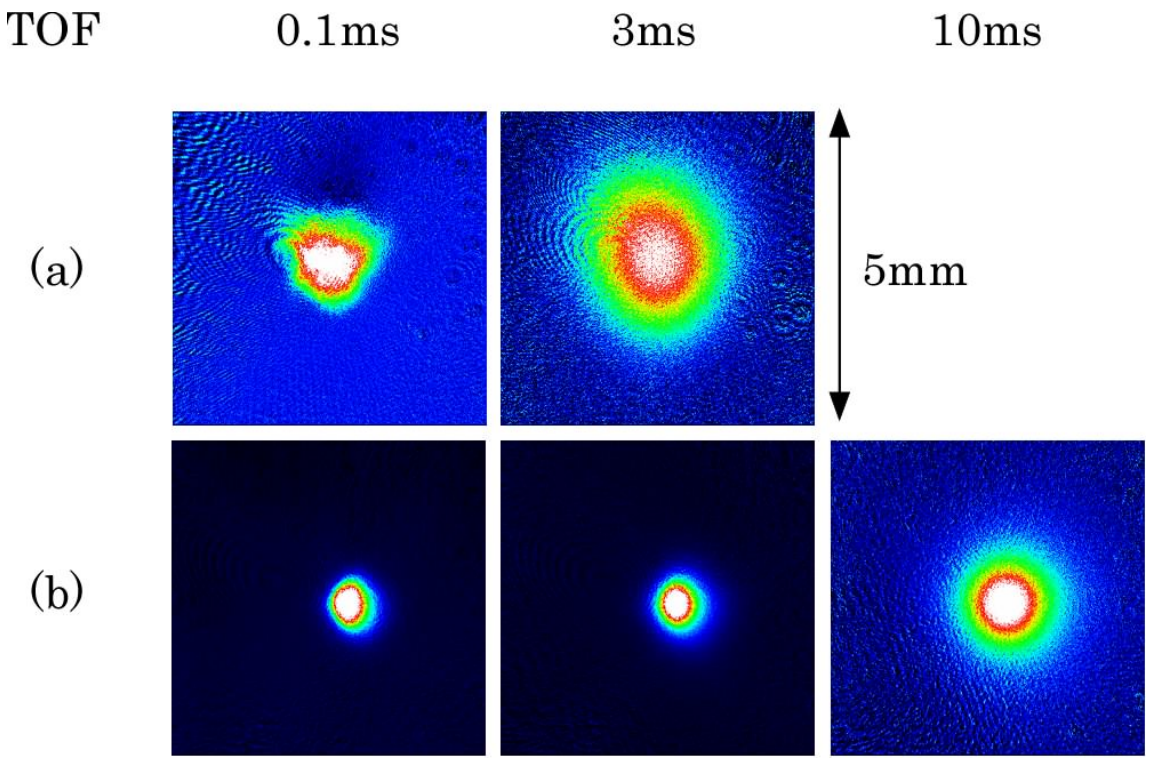

Fig.4.28 Images of atoms (a) after the steady state MOT and (b) after the time dependent MOT

The image of the steady state MOT after TOF of 10ms is not shown here since it is widespread. The images with TOF 0.1ms reflect the original density distribution while those with a long TOF are mainly determined by the temperature of the atomic cloud.

Table 4.1 Measured properties at each step

	Number [10^9]	Density [10^{10}cm^{-3}]	Temperature[mK]	Phase space density [10^{-7}]
Raman	3	0.3	30	0.012
Steady state	1.6	1.5	3	0.1
Compression	1.5	12	0.5	1.8
Cooling	1.1	5.1	0.1	11

Achieved phase space density after the cooling stage is comparable to that of other alkali species such as sodium or rubidium. We conclude that ^{41}K could be used for a condensate experiment if the conditions on the MOT light and magnetic field are changed from the steady state condition which collects a large number of atoms to the condition which compress and cool atoms within a sufficiently short time. Here the achieved temperature is lower than the Doppler limit of ^{41}K, 149 μ K. This suggests that the sub-Doppler cooling mechanism can work even when hyperfine pumping rate is high due to the small hyperfine splitting of excited states, which have already been suggested for the case of ^{39}K [62].

There are three important points to achieve the above condition.

1. Cooling is the most efficient at a small detuning. This is easily understood as a result of the Doppler cooling which is most effective at the detuning of $\Gamma/2$ (see expression 2.41). However, the sub-Doppler cooling seems to work for a sufficiently low intensity. This behavior is contrary to the case of Na, Rb and Cs for which the sub-Doppler cooling works well and the lowest temperature is obtained at a large detuning of around 60MHz.
2. The attainable minimum temperature seems to be limited by large number of atoms. In the last cooling stage, both trapping and repumping lasers are close to the resonance, which means that most of the light are scattered by the atoms located near the outer surface of the MOT. Thus the atoms located in the center of the MOT do not feel any cooling force, which leads to high temperature. It is important to fall atoms to the dark state (F=1) by lowering the intensity of the repumping laser at the last cooling stage. We confirmed that more than 90% of atoms are in the dark F=1 state after the cooling stage, but even such a low population of F=2 can cause decay of cooling force. It is possible to achieve even lower temperature for smaller number of atoms.
3. Atoms are very sensitive to the optical force in the last cooling stage because they feel the large force of nearly resonant light. If there is an imbalance between two counterpropagating MOT beams or the center of the magnetic field is not matched to the center of the MOT beams, atoms are easily blown up and disappear. The compensation coils for three axes are necessary to compensate the earth magnetic field and precisely tune the center of the magnetic filed. Even the best alignment could lose about 30% of atoms in our case.

4.3 Spectroscopy with REMPI at E2

4.3.1 Dual species MOT of ^{41}K and ^{87}Rb

Since number of molecules formed by photoassociation is proportional to the product of densities of ^{41}K and ^{87}Rb, it is crucial to achieve high density for both species to perform molecular spectroscopy with a high signal-to-noise ratio. Since we have already known the properties of the MOT of ^{41}K, we have measured how number and density of atoms in the MOT depend on the frequency and intensity of MOT light for Rb as done for ^{41}K. Figure 4.29 shows frequency dependence, while Figure 4.30 shows intensity dependence. Dependence on the frequency of the repumping light was not shown here since it is small. We fixed the repumping frequency to F=1→F'=2 transition.

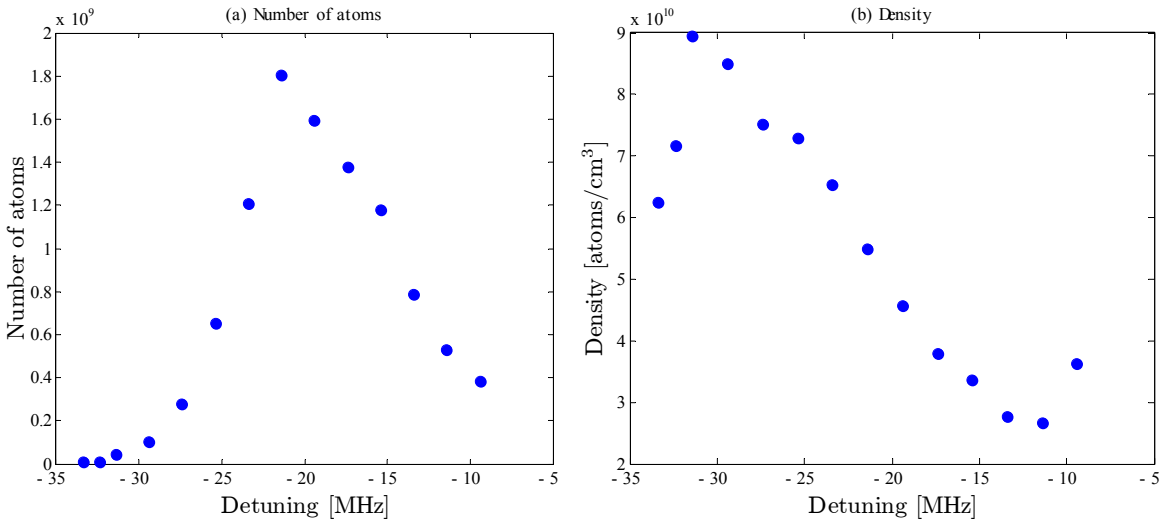

Fig.4.29 Frequency dependence of (a) number and (b) density for ^{87}Rb cooling light

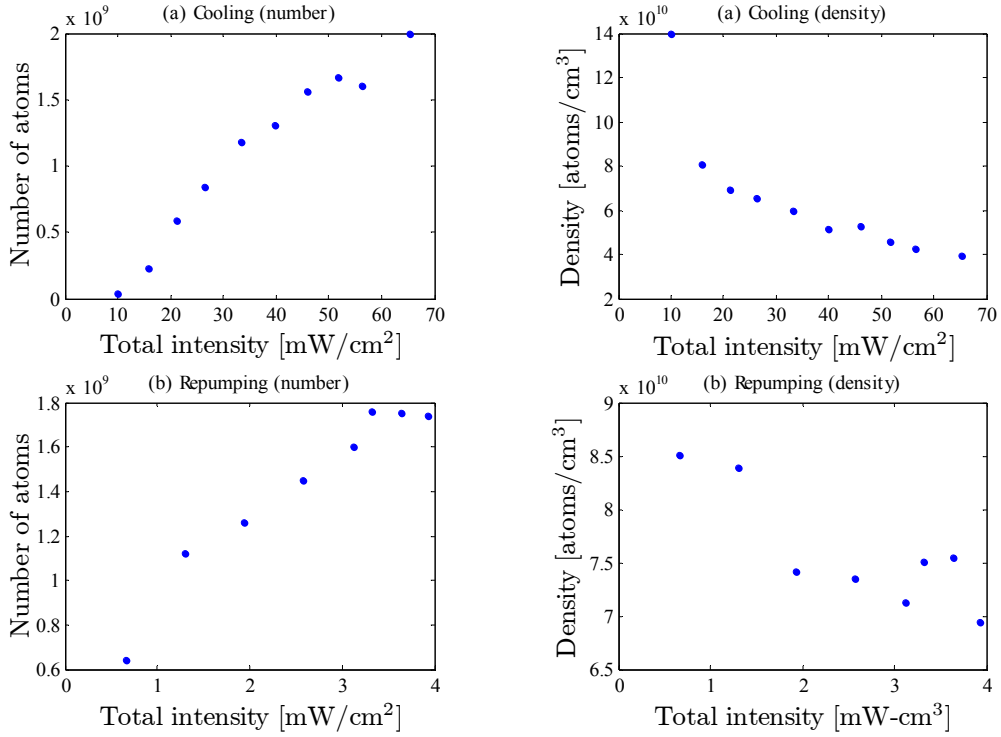

Fig.4.30 Intensity dependence of the MOT of ^{87}Rb for (a) cooling and (b) repumping

We can see clear differences between ^{41}K and ^{87}Rb: density of ^{87}Rb atoms is higher and much lower intensity suffices for repumping compared with ^{41}K. These differences result from the fact that ^{87}Rb can be regarded as a two level system while ^{41}K behaves as a three level system. Figure 4.31 shows level diagrams of ^{41}K and ^{87}Rb. In the case of ^{87}Rb, the large splitting between F'=3 and F'=2 relative to the atomic natural width (~6MHz) allows us to treat F=2→F'=3 transition to be a two level system.

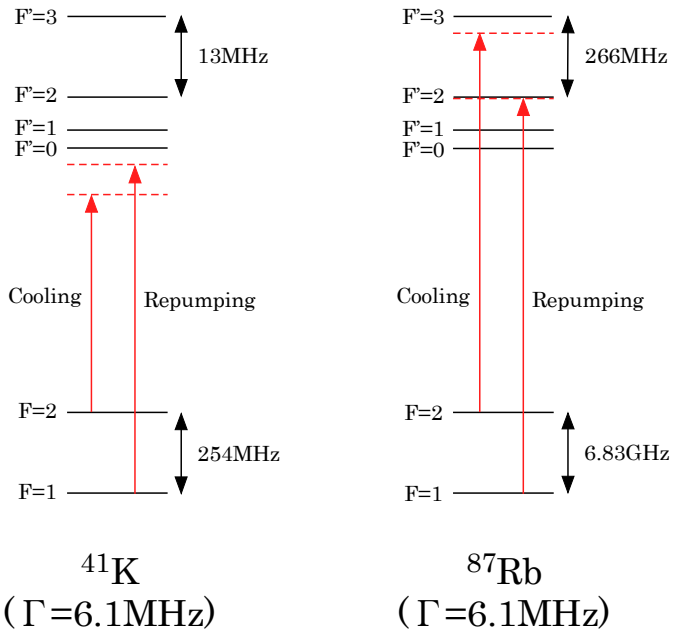

Fig.4.31 Level diagram of ^{41}K and ^{87}Rb

For ^{41}K we avoided Raman condition mentioned above to achieve high density. Intensity is kept to the maximum value for both trapping (50mW/cm^2) and repumping (33mW/cm^2) to obtain a large number of atoms. For ^{87}Rb we had a large detuning of 30MHz for trapping laser to achieve high density while repumping light is resonant. Intensity per each beam is around 8mW/cm^2 for trapping and 0.5mW/cm^2 for repumping.

Although we did not observe a loss of ^{87}Rb atoms due to coexistence with ^{41}K atoms, we observed a small loss of ^{41}K atoms due to coexistence with ^{87}Rb atoms as observed for ^{39}K and ^{85}Rb [116]. According to their work, the main loss mechanism of K-Rb system at low intensity regime is heteronuclear hyperfine changing collision and is not radiative escape or fine structure changing collision.

4.3.2 Ionization and detection of atoms and molecules

We observed ionized atoms and molecules with time-of-flight (TOF) mass spectroscopy. A typical TOF spectrum is shown in figure 4.32. This data was taken without shining the photoassociation laser and turning off the MOT laser and magnetic field. The first large signal is due to the pulse laser scattered at the glass window and the internal surface of the chamber. Though each peak should have more complicated structure just after the MCP due to variation in the arrival time, we obtained an integrated single peak for each species because all signals passed through a low pass filter. It is clearly seen that K^+, Rb^+ and Rb_2^+ are separately detected at the delay time proportional to square root of the mass. We confirmed that each peak appears only when the MOT light for the corresponding atomic species is irradiated. There are no background atoms or molecules. We also confirmed that Rb_2^+ peak exists even when the MOT light is turned off 300 μ s before a pulse laser is irradiated. This ensures that we have detected ground state molecules. These molecules are supposedly formed by the trapping laser of ^{87}Rb.

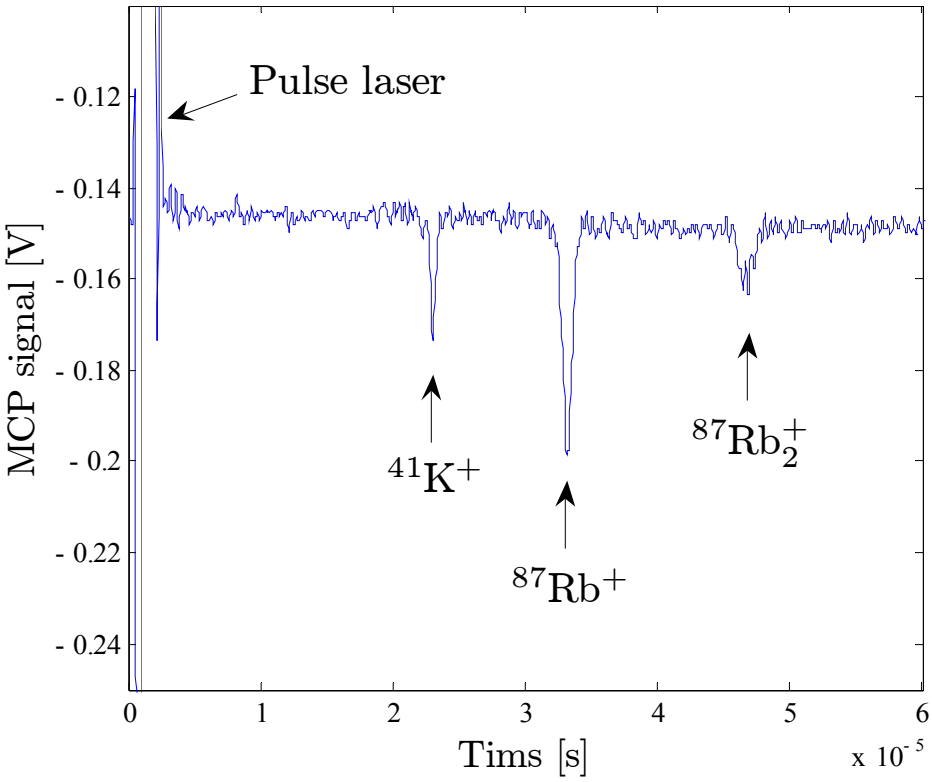

Fig.4.32 Time-of-flight spectrum of laser-cooled K, Rb and Rb_2.
The first signal is caused by the scattered pulse laser. The subsequent three peaks correspond to K^+, Rb^+ and Rb_2^+, respectively. This signal is obtained without photoassociation laser.

Observed relative ratios between three peaks are

$$t_{Rb}/t_K = 1.44$$
$$t_{Rb_2}/t_{Rb} = 1.42$$

These values well coincides with square root of actual mass ratios [117]

$$\sqrt{m_{Rb}/m_K} = 1.457$$
$$\sqrt{m_{Rb_2}/m_{Rb}} = 1.414$$

Though the TOF ratios are in good agreement with the mass ratios, the observed TOF's are much longer than we expected. If we assume that the elected field gradient between MCP and an atomic cloud is constant, TOF is estimated to be

$$t = \sqrt{\frac{2m(a+b)b}{eV}}$$

where a is distance between an atomic cloud and the surface of the chamber opposite to the MCP, b is distance between atomic cloud and the MCP, e is charge of electron and V is the voltage applied between the MCP and the chamber. This expression gives TOF time of 3.4 μ s for ^{41}K, 4.9 μ s for ^{87}Rb and 6.9 μ s for $^{87}Rb_2$. These values are much smaller than actually observed. This unexpected behavior seems to indicate that the actual electric field gradient is rather small near the atomic cloud due to the proximity to the chamber surface.

Here we give considerations on how atoms and molecules are ionized. In the above experiment, the pulse laser was operated at around 602.6 nm which is used in previous works on Rb_2 [35, 118, 119, 120, 121, 122] and KRb [43, 123, 124, 125]. The wavelength 602.6 nm is near resonant with two-photon transitions connecting the ground state atoms to the Rydberg state Rb(16D) and K(8D) and thus they are finally ionized with absorbing an additional photon. This means that atoms are ionized with three photon transitions. The intermediate state at the first two-photon process is far away from the atomic transition for both K and Rb and thus the whole ionization efficiency is expected to be small for both species. The situation is quite different for Rb_2 molecule. The wavelength 602.6nm lies in the Rb_2 diffuse band [126, 127] which is connecting the ground state $a^3\Sigma_u^+$ to the excited $(2)^3\Pi_g$ and the ground state $X^1\Sigma_g^+$ to the excited $(2)^1\Sigma_u^+$ as shown in figure 4.3.6. Using $(2)^3\Pi_g$ and $(2)^1\Sigma_u^+$ as an intermediate state, Rb_2 are ionized to $(1)^2\Sigma_g^+$ of Rb_2^+ potential. It is clear that Rb_2 molecules are ionized with two photon transitions in contrast to atoms. Here the intermediate state is nearly resonant to a vibrational level and has a significant overlap between both the ground state and the excited ionized state as seen from figure 4.33. Thus the whole ionization efficiency is expected to be large. These differences in the ionization process give a qualitative explanation to the counterintuitive results that observed numbers of atoms and molecules are of the same order: molecules formed by photoassociation are much less than atoms in a MOT but ionization efficiency is much higher for molecules than for atoms.

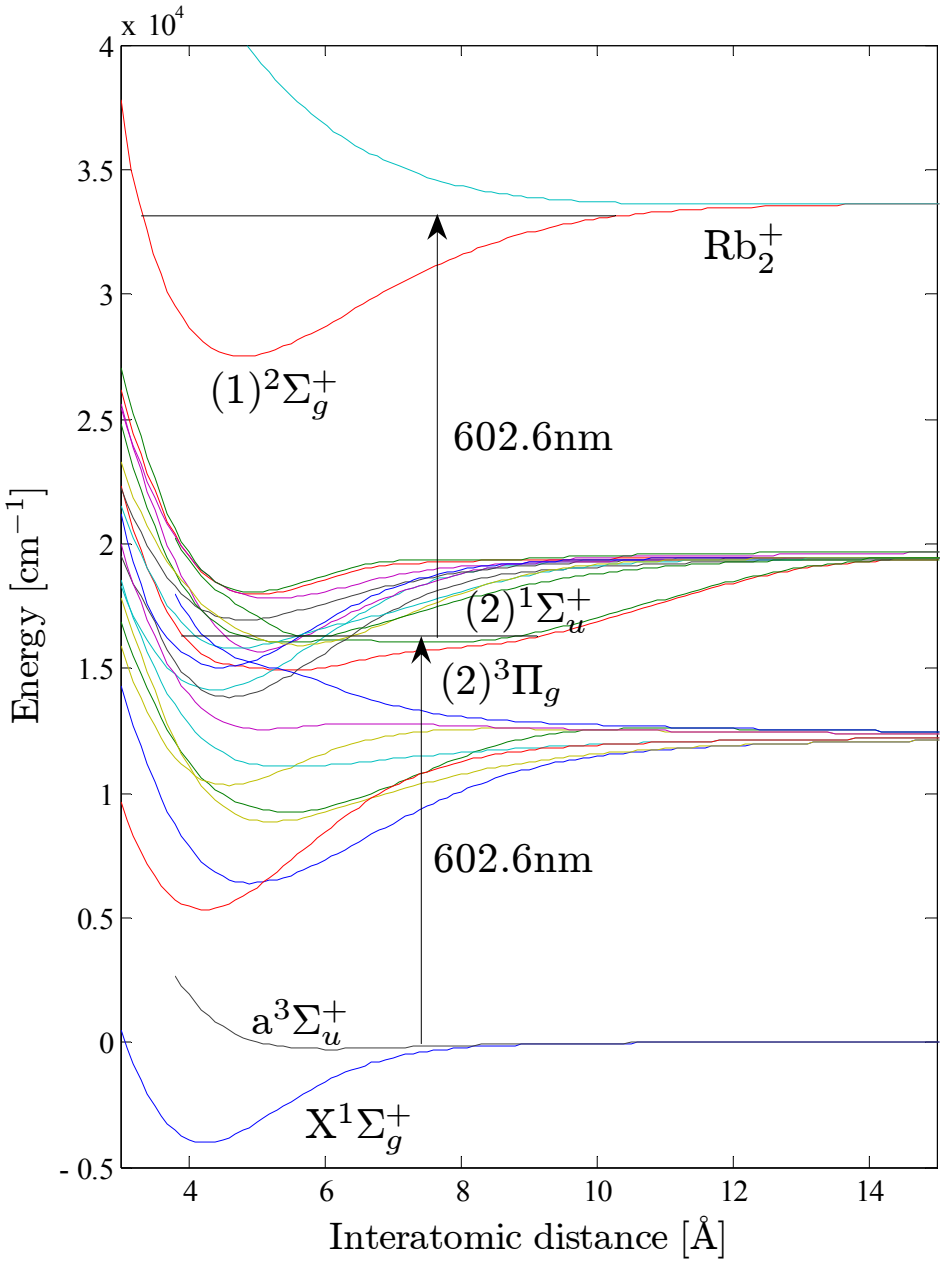

Fig.4.33 Potential energy curves of Rb_2 and Rb_2^+ molecule. Rb_2 potentials are calculated with MOPLRO and only 18 states dissociating to 5S+5S, 5S+5P and 5S+4d are shown. Here Δ states are omitted. Rb_2^+ potentials are taken from [128].

Although we have not yet succeeded in observation of KRb molecules, we give a consideration on how KRb molecules are ionized. Figure 4.34 shows the interatomic potentials of KRb [107] and KRb^+ molecule [129]. When the pulse laser of the wavelength 602.6 nm is irradiated, the ground state singlet molecules are ionized to form loosely bound Rb_2^+ through the intermediate $(4)^1\Sigma^+$ state. This process is expected to work well since there is a significant overlap between the ground and the intermediate states and also between the intermediate and the excited ionized states as in the case of Rb_2. In contrast, triplet molecules are considered to be ionized

with lower efficiency since both intermediate states $(4)^3\Sigma^+$ and $(3)^3\Pi$ have a relatively small overlap between the ground states and the ionized states. In practice, it is reported that detection of triplet KRb molecules with the wavelength of 602.6 nm requires higher laser intensity [125].

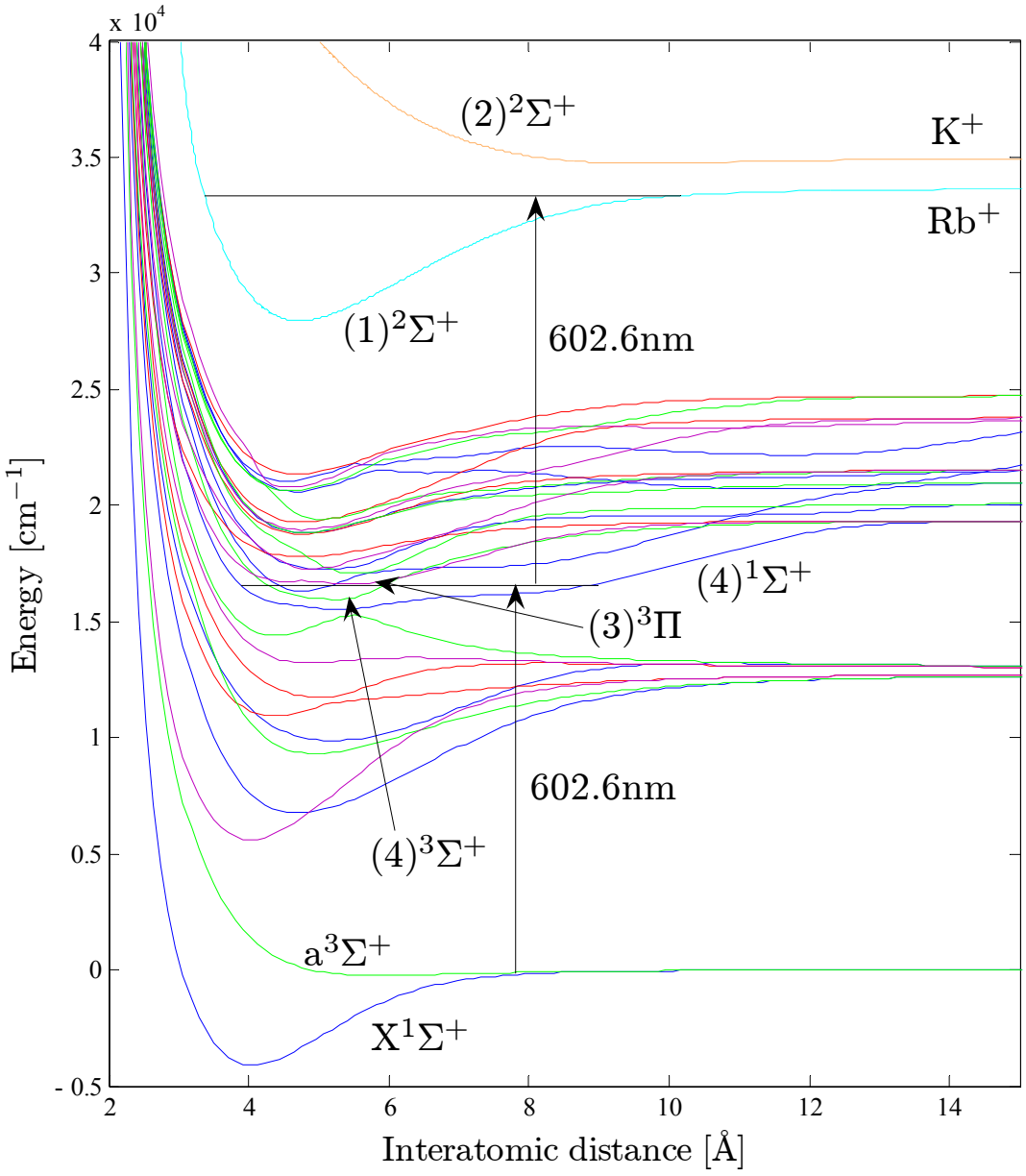

Fig.4.34 Potential energy curves of KRb and KRb^+. KRb potentials are taken from [107] while KRb^+ potentials are taken from [129]. Blue, green, red and purple lines indicate $^1\Sigma^+$, $^3\Sigma^+$, $^1\Pi$ and $^3\Pi$, respectively. Here Δ states are omitted.

We have also tried ionization of atoms and molecule at the pulse laser wavelength of 532nm which is separated from the doubled Nd:YAG laser but we did not detect any molecule and observed only K and Rb atoms. This fact is attributed to the low ionization efficiency due to the poor overlap of wavefunction between the ground and intermediate and also the intermediate and excited ionized state.

4.3.3 Photoassociation spectroscopy of Rb_2

We performed a photoassociation spectroscopy of Rb_2 molecules to confirm that our system has a capability to produce molecules with an additional photoassociation laser. Since we know that laser-cooled ^{41}K atoms have a high temperature and a low density at a steady state, we first tried photoassociation of ^{87}Rb which has been well studied so far. Our photoassociation laser is derived from a DFB laser which enables us to scan a wide frequency range without a mod hop. 2mW of DFB laser is amplified to 200mW through a slave laser and a tapered amplifier. The photoassociation laser is focused at the center of MOT to a diameter of around 450 μ m. This corresponds to an intensity of 320W/cm^2.

We had not been able to detect any molecule at a steady state in the presence of a photoassociation laser. This means that molecules which had been observed previously is formed by the MOT laser and not by the pulse laser since the pulse laser is irradiated in both cases. Supposedly the non-resonant photoassociation laser pumps molecules formed by the MOT laser back to atoms.

To enhance the molecule formation rate, we performed a compressed MOT (C-MOT) for Rb continuously. Figure 4.35 shows our experimental time sequences of C-MOT. The whole compression procedures shown below are synchronized to the pulse laser and repeated at 10Hz. This procedure increases the density of MOT for around 10ms by one order (2×10^{10}/cm^3→2×10^{11}/cm^3) and is expected to enhance the molecules formation rate by two orders.

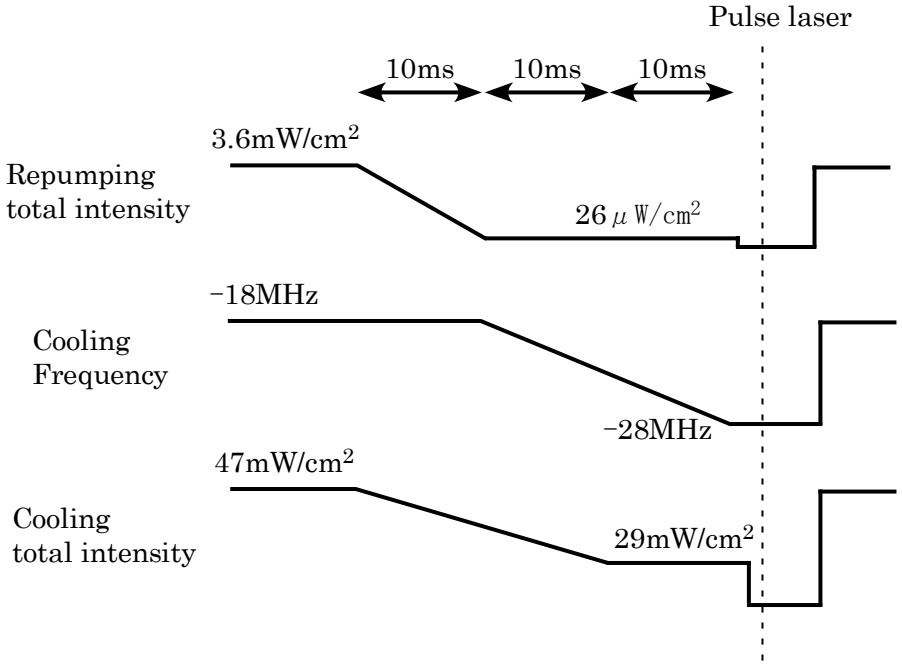

Fig.4.35 Experimental time sequences of Rb C-MOT

With a C-MOT, photoassociation spectra are easily observed. Figure 4.36 shows a typical spectrum. Observed linewidth of each peak is around 10MHz which probably reflects the linewidth of the DFB laser. The spectrum in figure 4.36 shows a clear rotational structure and does not show any complicated hyperfine structure. This means that this state has a symmetry of 0_g^- or 0_u^+. From this figure, we can see that the molecule formation rate is greatly enhanced only when the photoassociation laser is resonant to a molecular excited state.

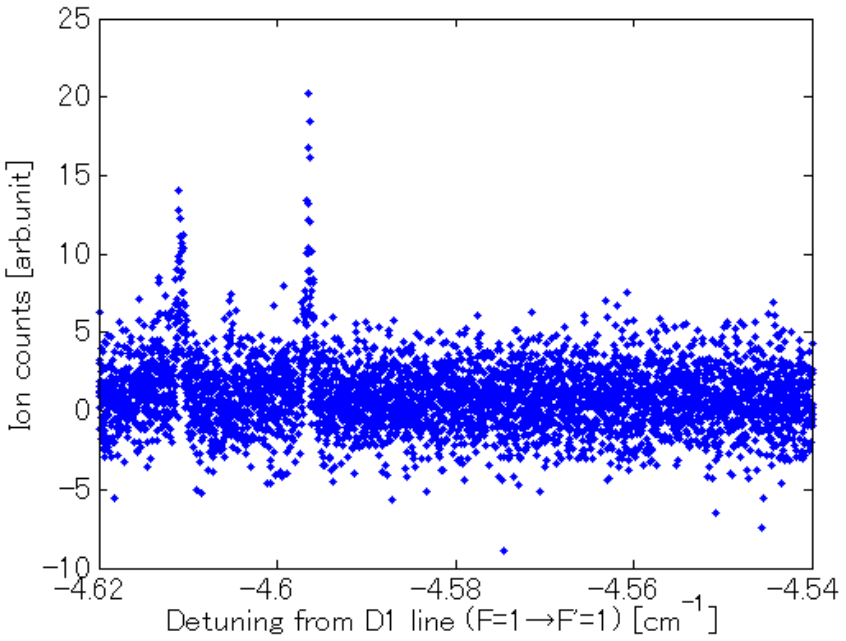

Fig.4.36 Photoassociation spectrum of Rb_2

Chapter 5 Conclusion and outlook

We have studied a double MOT system with ^{39}K atoms. Velocity of pushed atoms is measured directly with the time difference between the time when push beams are irradiated and the time when number of atoms in the 2nd MOT begins to increase. Measured velocity is ranged in 10~20m/s which is smaller than the capture velocity of MOT of ^{39}K. The transverse distribution of pushed atoms is measured by blowing out a part of atoms with a resonant light. The atomic distribution measured at two different points revealed that the transverse temperature is 230 μ K. This transverse temperature enables us to estimate the spread of atomic beam at the 2nd MOT is 15mm. These data on longitudinal and transverse velocity of atoms indicate that most of pushed atoms are captured at the 2nd MOT in our double MOT system. A focused beam with a diameter of 0.3mm is the most suitable for pushing atoms from the 1st MOT since it does not affect the 1st MOT seriously. Though the ratio between the loading rate of the 2nd MOT and that of the 1st MOT is ranged in 0.3~0.4, the lifetime of the 2nd MOT is longer than that of the 1st MOT by one order. Thus resulting number of atoms in the 2nd MOT is larger than that of the 1st MOT by a factor of 2~3.

We have investigated propertied of MOT of ^{39}K and ^{41}K atoms. For ^{39}K, we measured dependence of number of atoms on the detuning and intensity of MOT light with a fluorescence method. We showed that number of atoms increases as intensity increases. A large detuning is required to suppress hyperfine pumping to F=1 state. We found that number increases by a factor of three at a detuning of Raman condition for cooling and repumping light compared to an ordinary non-Raman condition. With a high intensity and a large detuning, we were able to trap more than 5×10^9 atoms.

For ^{41}K, we studied dependence of temperature and density on the detuning and intensity of MOT light with absorption imaging. As in the case of ^{39}K, number of atoms is enhanced at the Raman condition also for ^{41}K. 3 $\times10^9$ atoms are captured in a MOT at this condition. It is found that temperature of atomic cloud is quite high (~10mK) and density is quite low (~10^9 atoms/cm^3) at the Raman condition. We also found that temperature is lower (~3mK) and density is higher (~10^{10} atoms/cm^3) at a non-Raman condition. In this stage, phase space density of atomic cloud is relatively low (~10^{-10}) compared to other alkali atomic species. To achieve a higher phase space density, we have performed a time-dependent MOT. By increasing the magnetic field gradient, we were able to increase the density by a factor of 5. By lowering the detuning and intensity of MOT light, the temperature is reduced by a factor of 30. With this time-dependent MOT, the phase space density is improved by 3 orders. The resulting phase space density of 10^{-6} is comparable to other alkali species such as Na and Rb. We conclude that we have established a method of laser cooling of ^{41}K atoms. The next goal of this experiment is to make a condensate of ^{41}K and ^{87}Rb and to form loosely bound Feshbach molecules of ^{41}K^{87}Rb.

We built up another machine to perform spectroscopy on loosely bound heteronuclear molecules formed by photoassociation. A dual species MOT of ^{41}K and ^{87}Rb is constructed. Density and number of atoms are measured with absorption imaging for both ^{41}K and ^{87}Rb to maximize number of molecules formed by photoassociation. At a steady state condition, we have trapped 2×10^9 ^{87}Rb atoms with a density of $5\times$ 10atoms/cm^3 and 5×10^8 ^{41}K atoms with a density of 2×10^{10}atoms/cm^3. Shining an intense pulse laser to the dual species MOT, we observed K^+, Rb^+ and Rb_2^+ separately with a microchannel plate (MCP). Relative ratios between time-of-flights of K^+, Rb^+ and Rb_2^+ are in good agreement with the square root of their mass ratios. Observed number of each species is estimated to be around 100 for ^{41}K, 20 for ^{87}Rb and 2 for $^{87}Rb_2$. These figures mean that our apparatus is sensitive enough to detect even a few molecules. With this apparatus, we are able to perform a precise spectroscopy on loosely bound ^{41}K^{87}Rb molecules formed by photoassociation. We are going to search an optimum transition to transfer the loosely bound molecules to the lowest vibrational level of the ground state singlet potential with a two photon transition. Detecting a resultant few molecules is also possible with our sensitive machine.

Our final goal is formation of quantum degenerate heteronuclear molecules in their lowest vibrational level. Applying the optimum transition found in the spectroscopy experiment to Feshbach molecules of $^{41}K^{87}Rb$, we are going to achieve a stable Bose-Einstein condensate of heteronuclear molecules. Properties of dipolar condensates will be investigated in the presence of optical lattices. Tunability of intermolecular potential with microwave will be demonstrated. We are going to study an ordered phase of dipolar condensates in optical lattices by tuning interaction between molecules.

Appendix A Circuits

(1) Thermoelectric controller for a slave laser

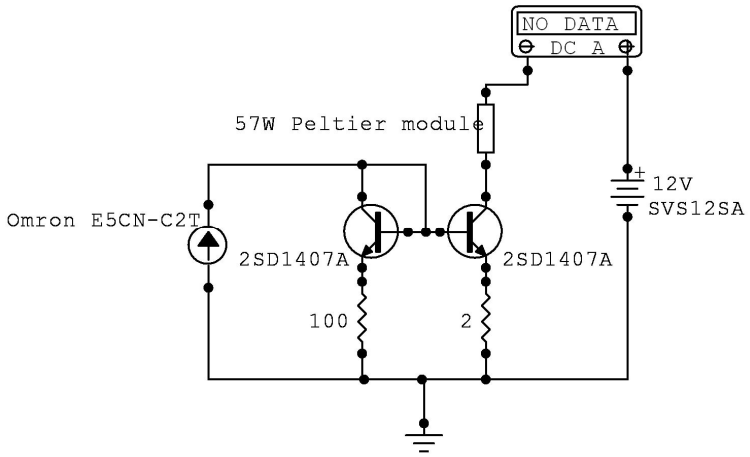

(2) Thermoelectric controller for a tapered amplifier

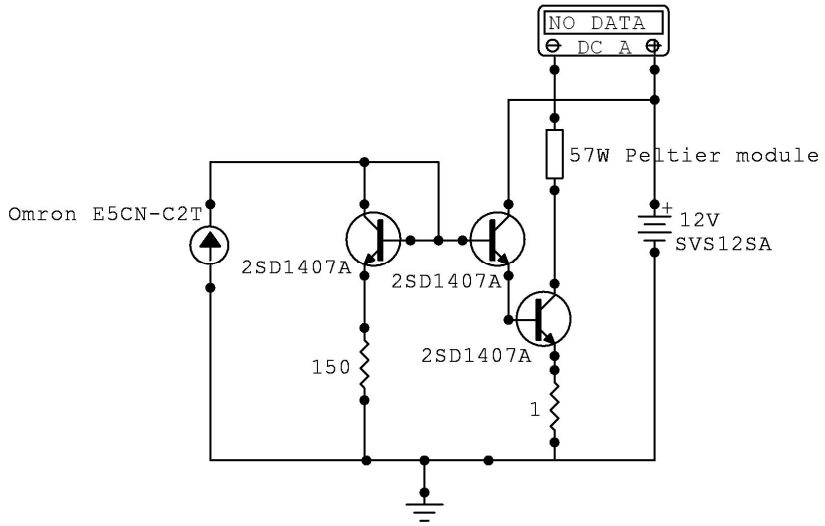

(3) AOM driver

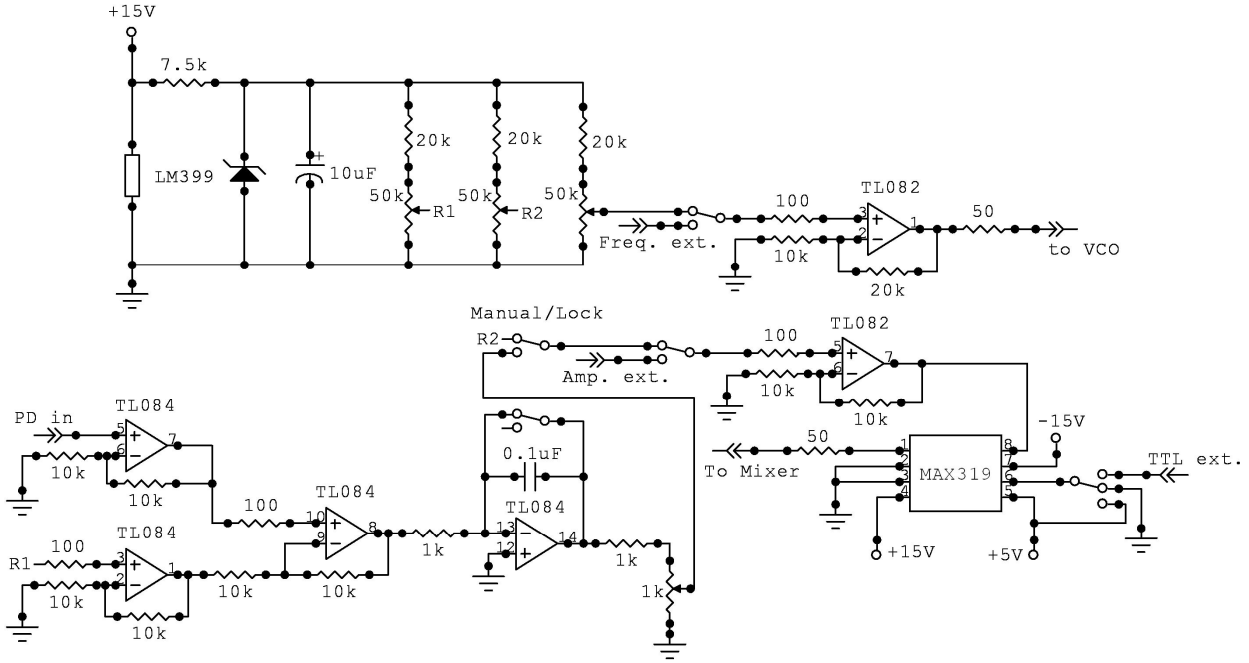

(4) High speed photo detector for locking

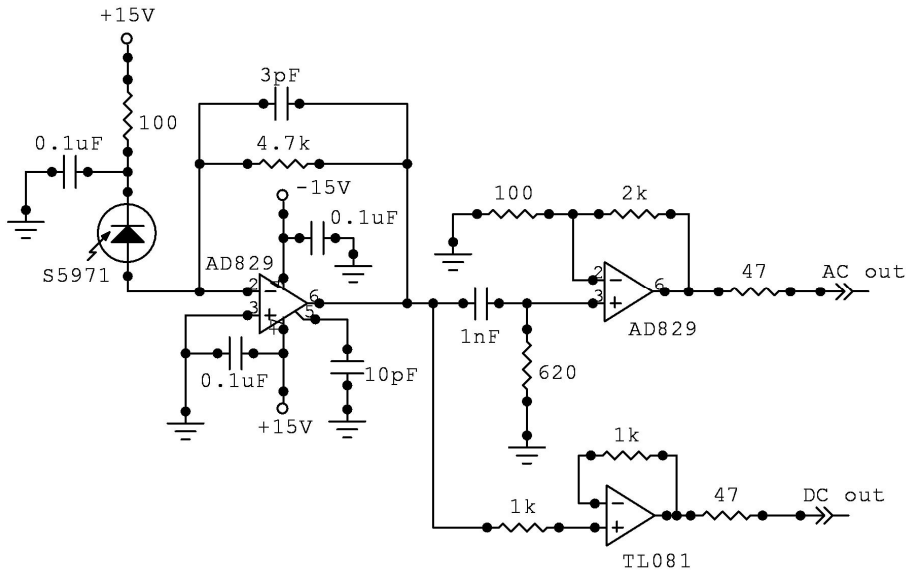

(5) Protection circuit for a laser diode

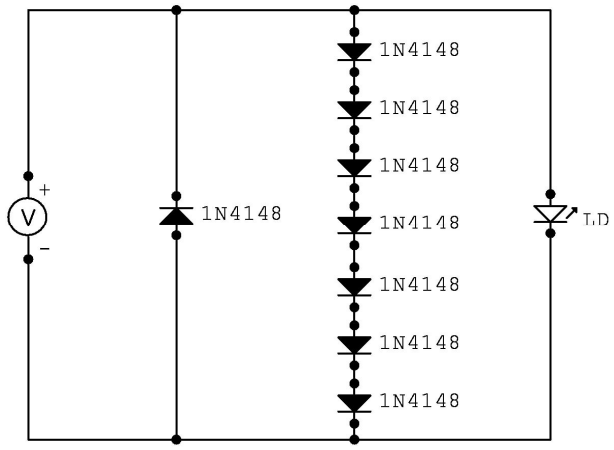

(6) Lock circuit

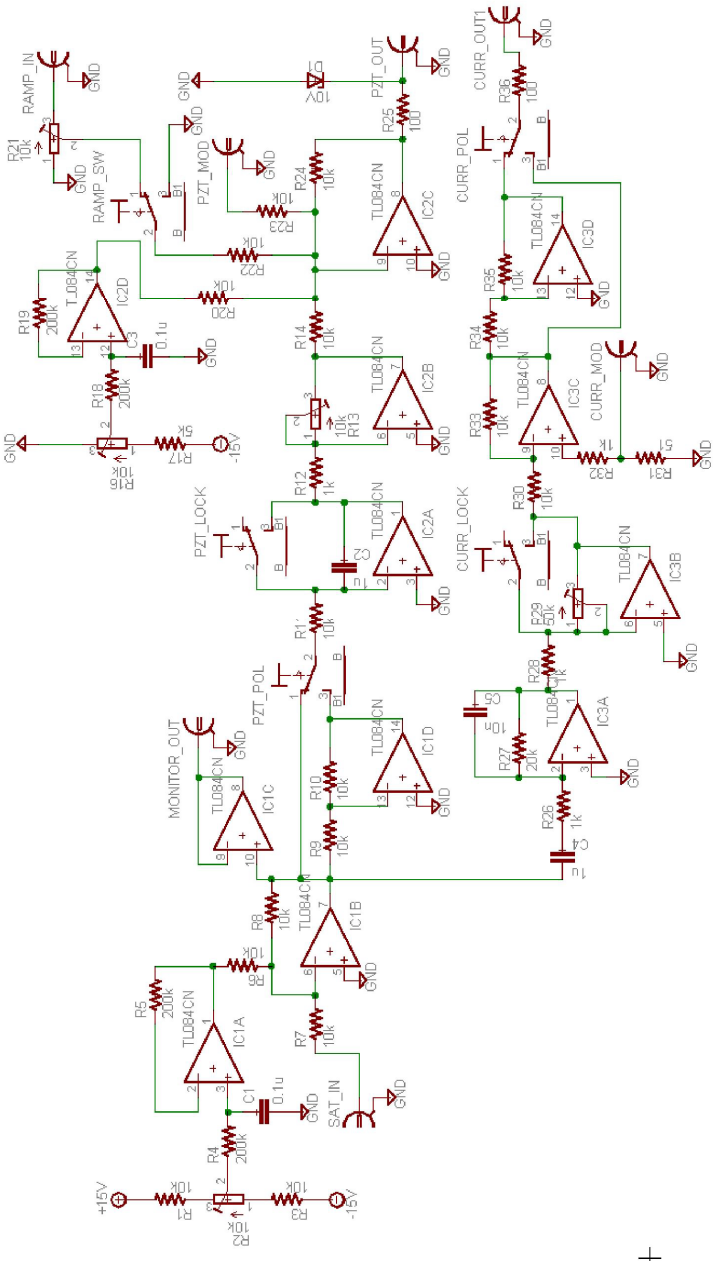

Appendix B　Box design

(1) Thermoelectric controller for a slave laser

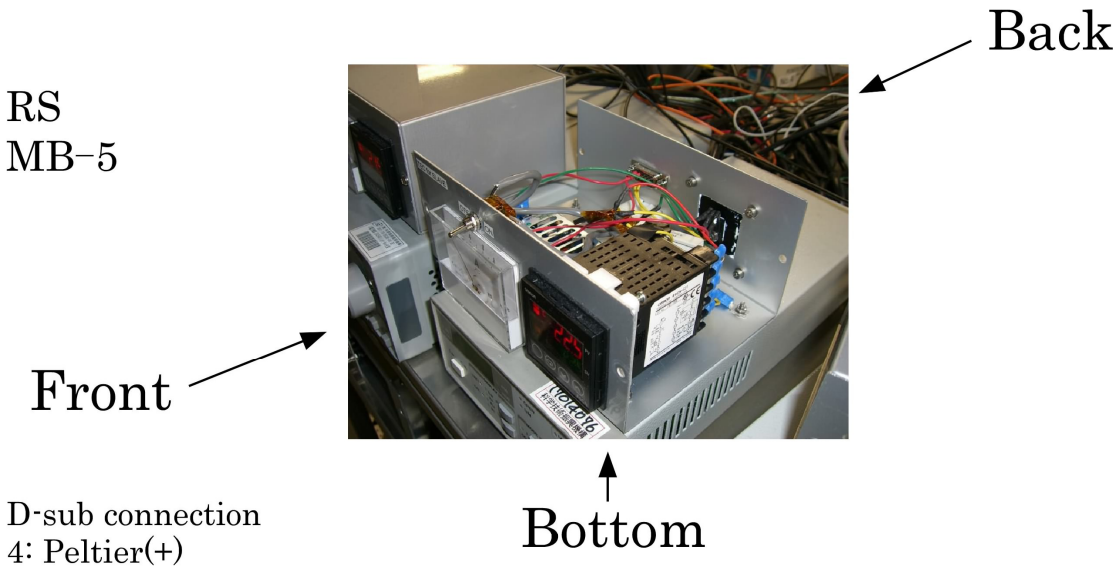

D-sub connection
4: Peltier(+)
5: Peltier(−)
6,7: Pt100

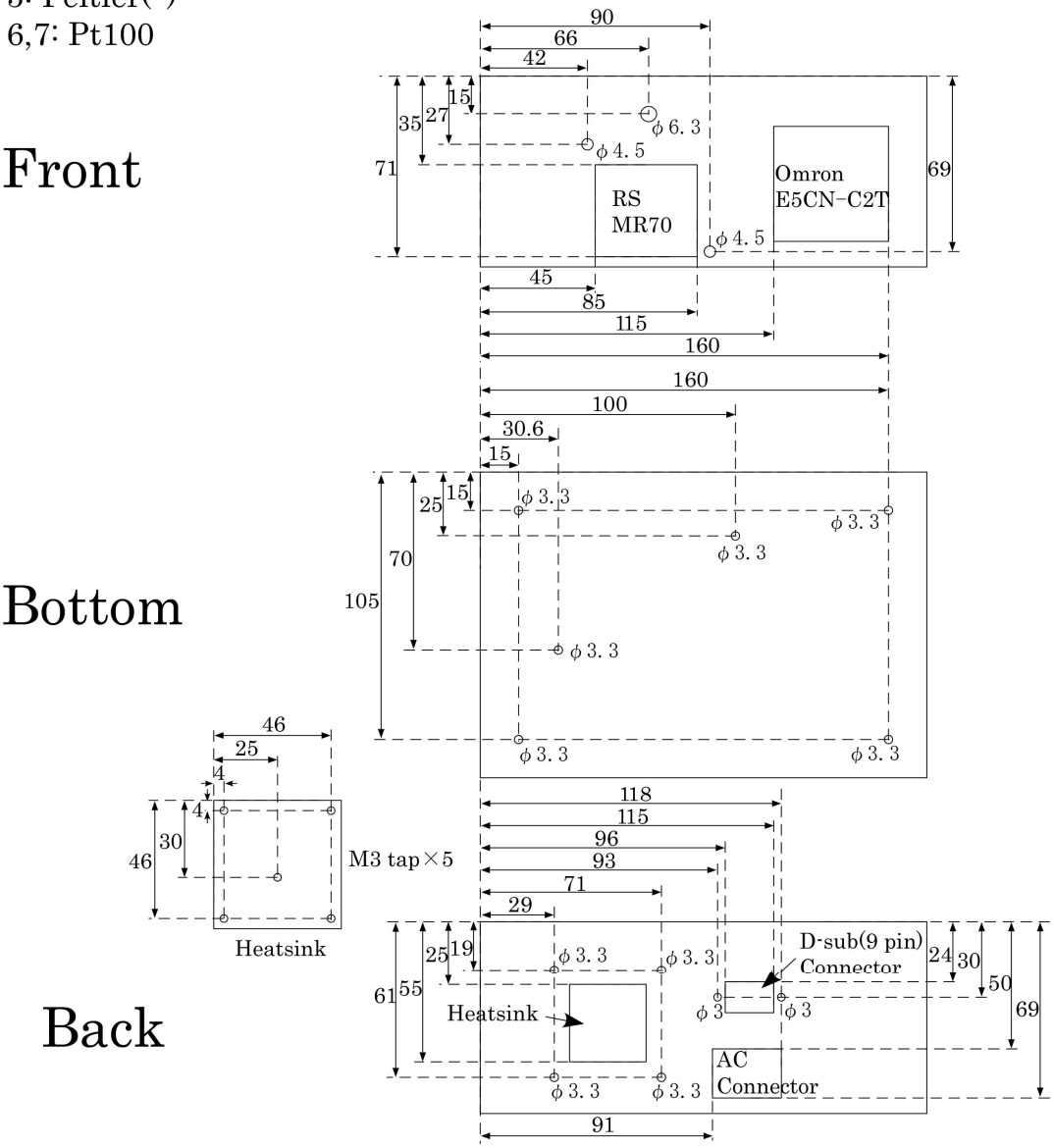

(2) Thermoelectric controller for a tapered amplifier

RS
MB−5

D-sub connection
4: Peltier(−)
5: Peltier(+)
6,7: Pt100

Front

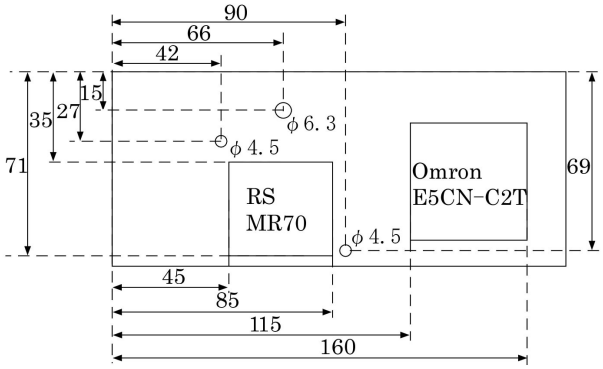

Bottom

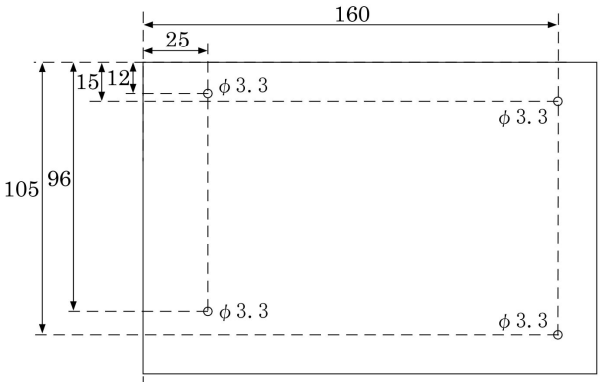

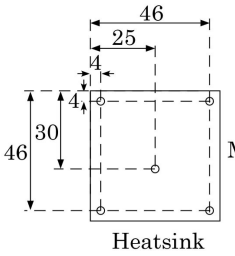

M3 tap×5

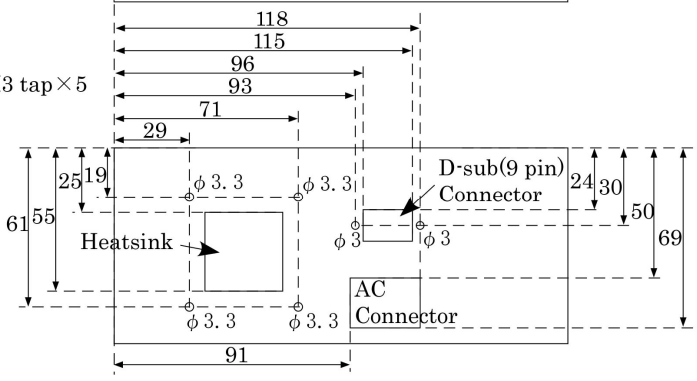

Back

(3) VCO and RF amplifier

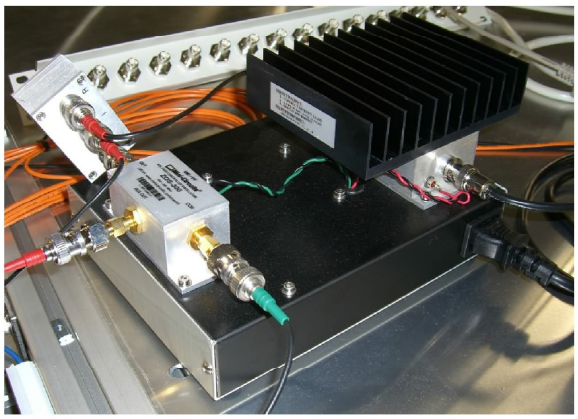

(4) AOM driver

Takachi
PLG case

Front →

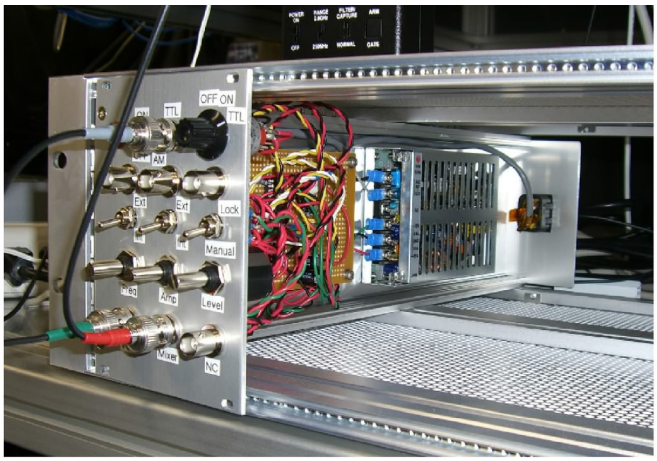

← Side

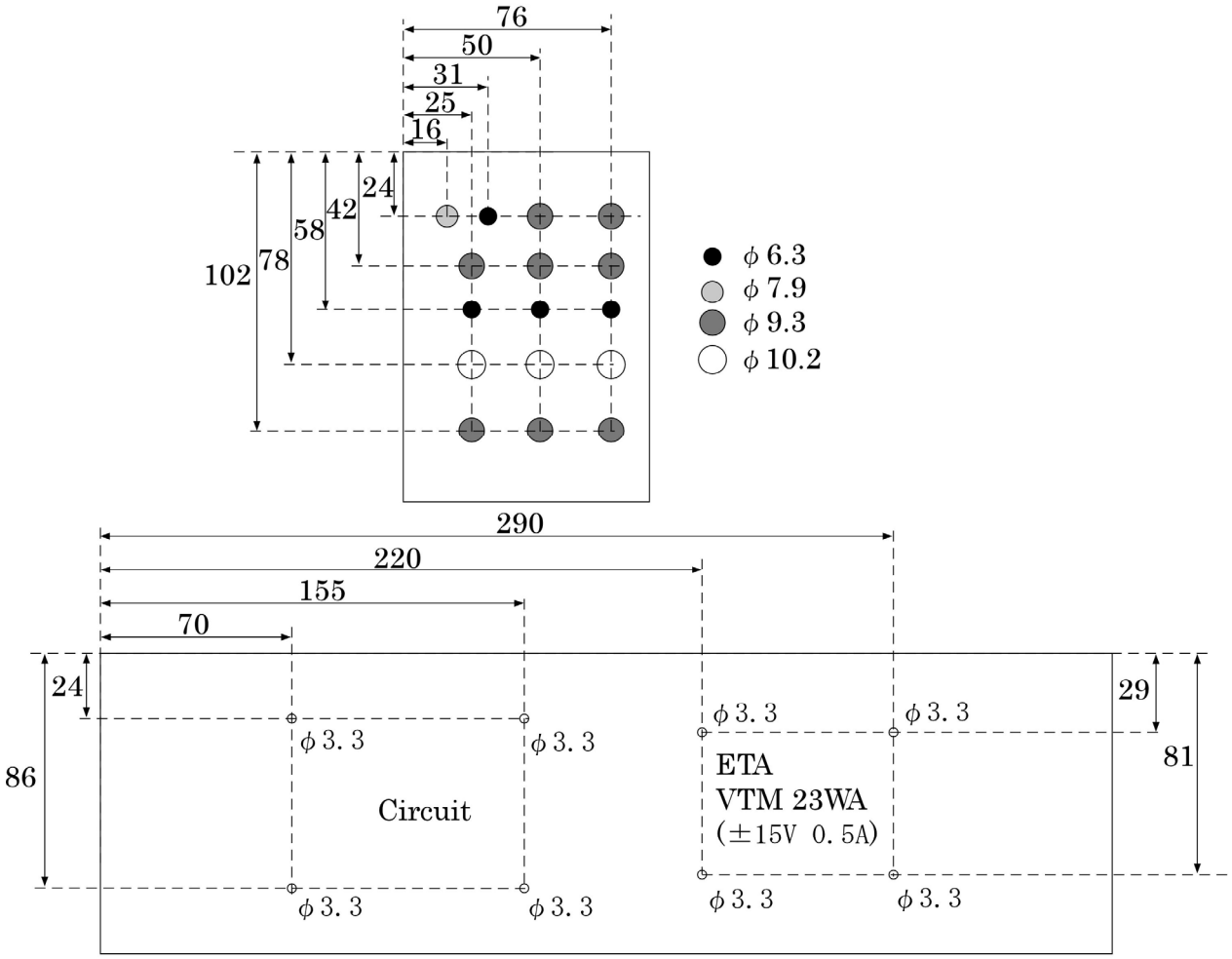

Appendix C Design of ECDL

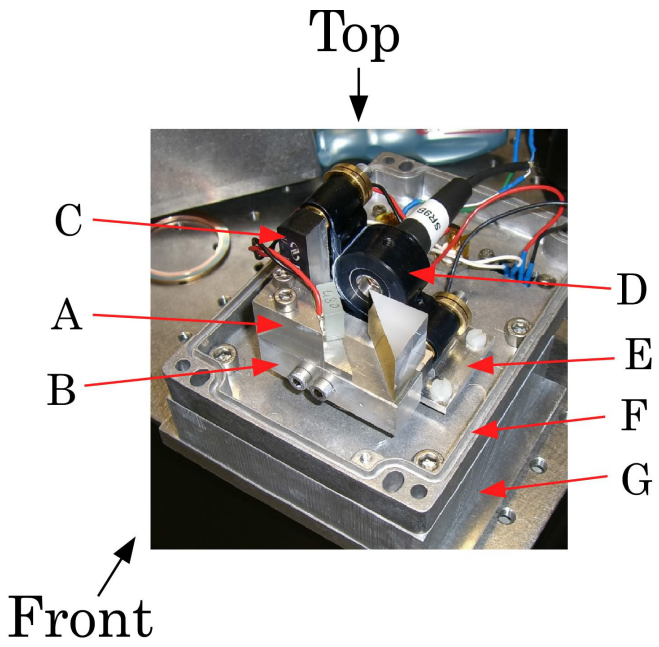

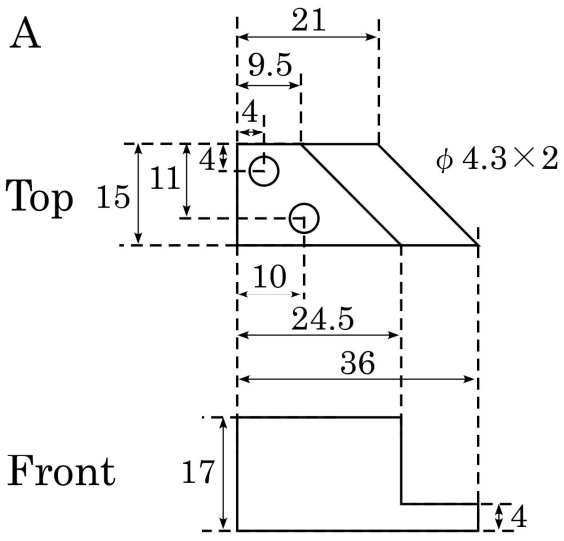

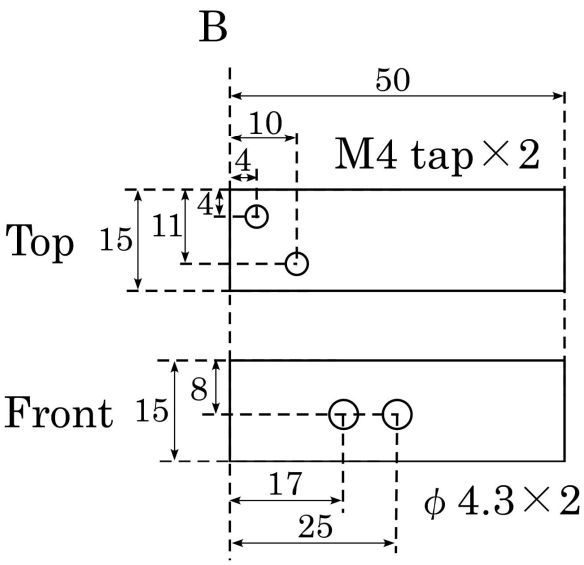

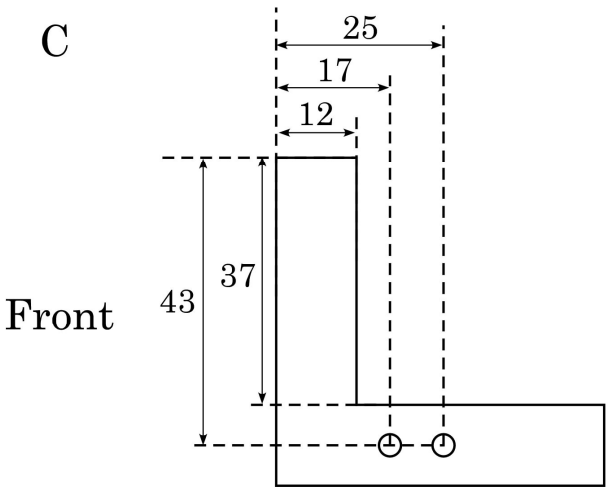

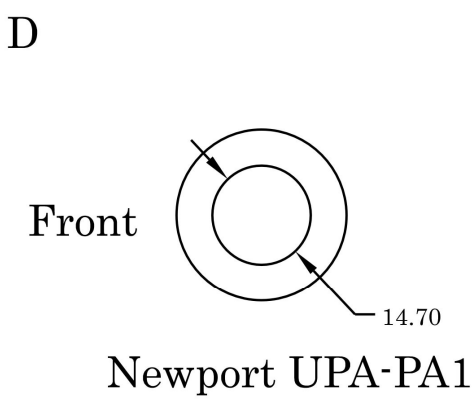

E

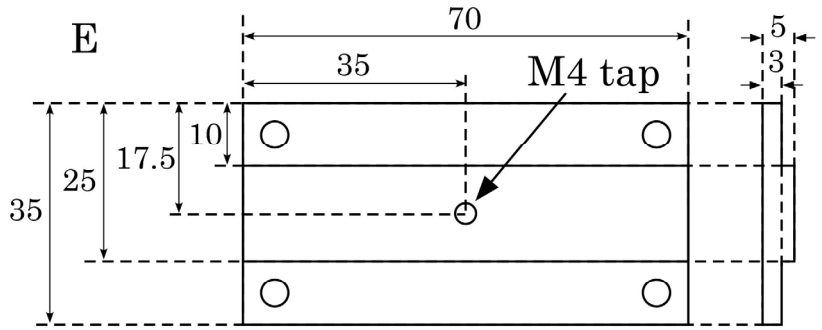

ϕ 4.3×4

Top Side

F

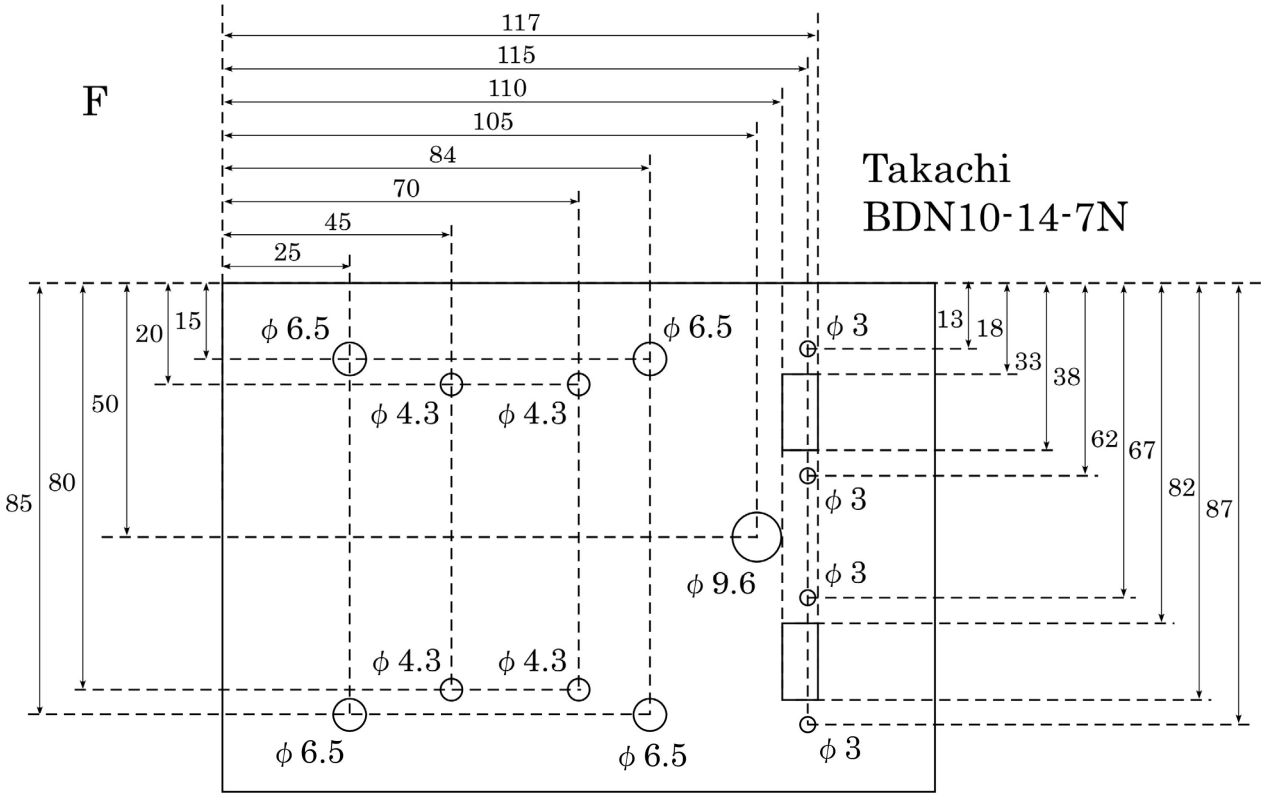

Top

G

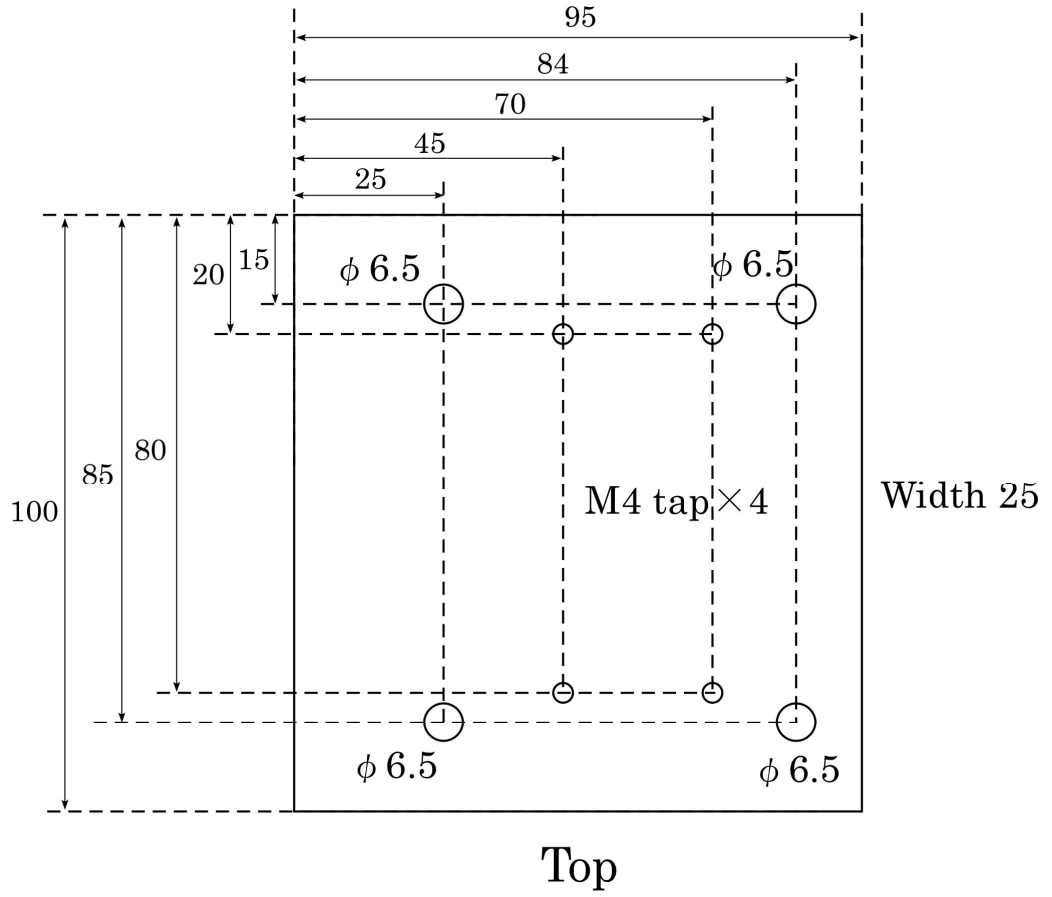
95
84
70
45
25
20
15
ϕ 6.5
ϕ 6.5
100
85
80
M4 tap×4
Width 25
ϕ 6.5
ϕ 6.5

Top

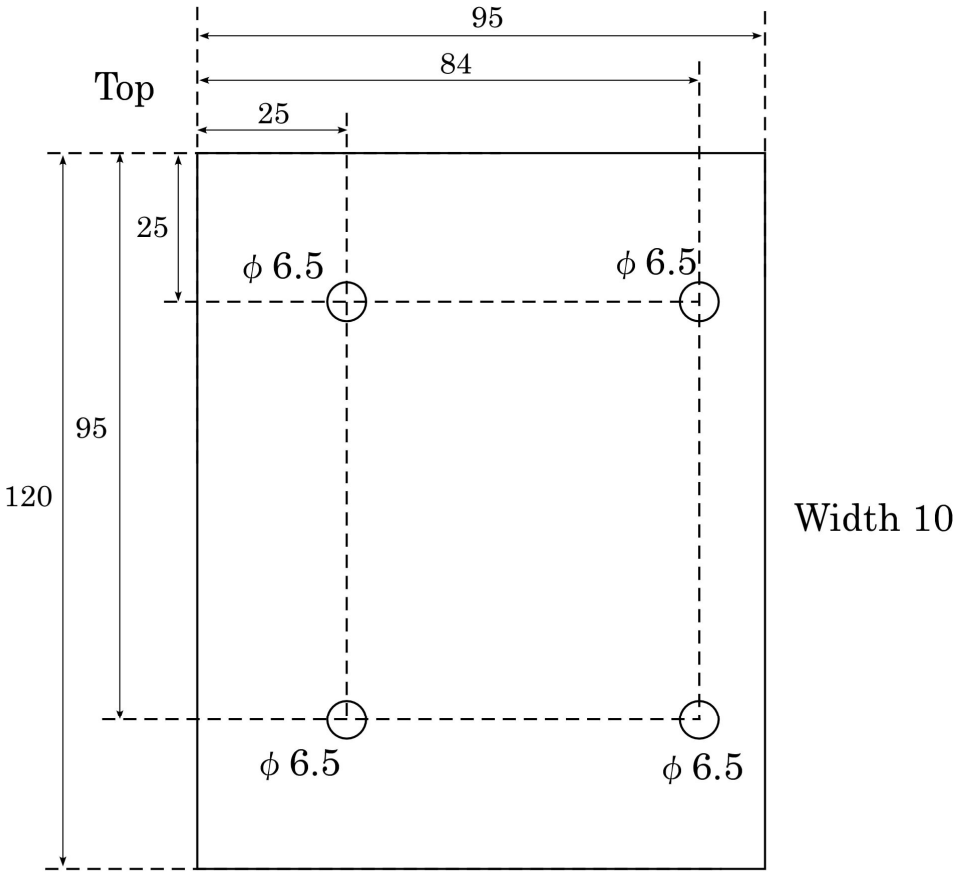
95
84
Top
25
25
ϕ 6.5
ϕ 6.5
95
120
Width 10
ϕ 6.5
ϕ 6.5

Top

Appendix D Design of slave laser

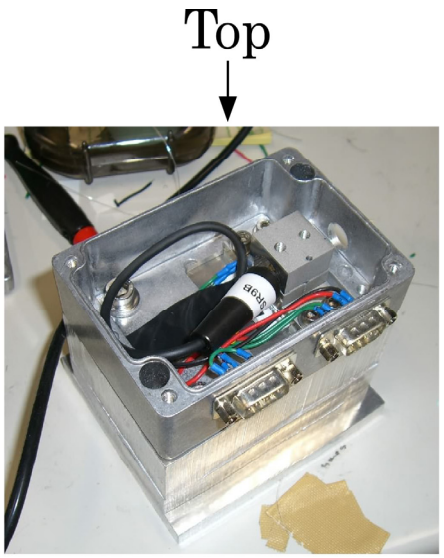

(a) Box

Takachi
BDN7-10-4N

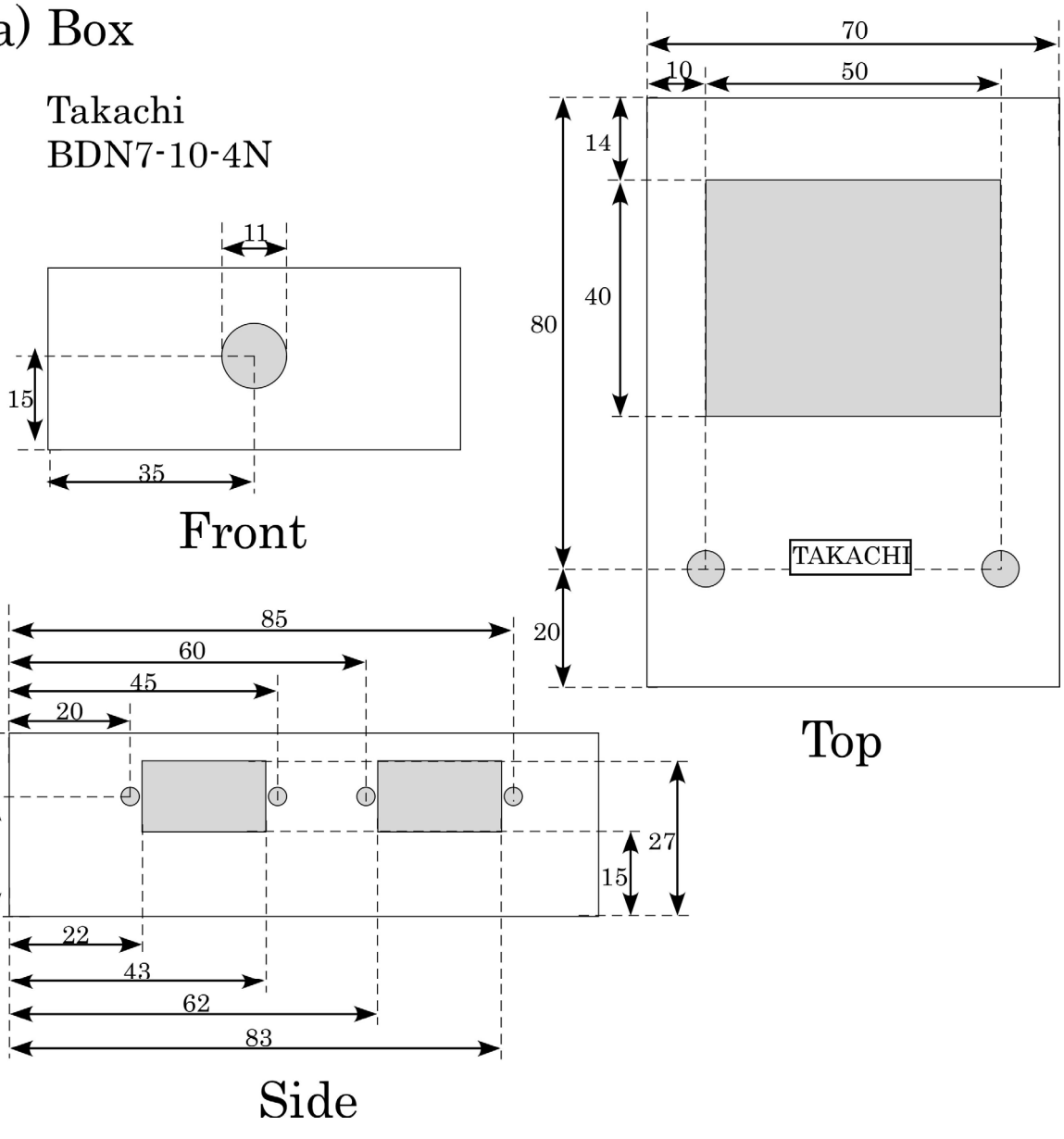

(b) LD holder & Pedestal

LD holder

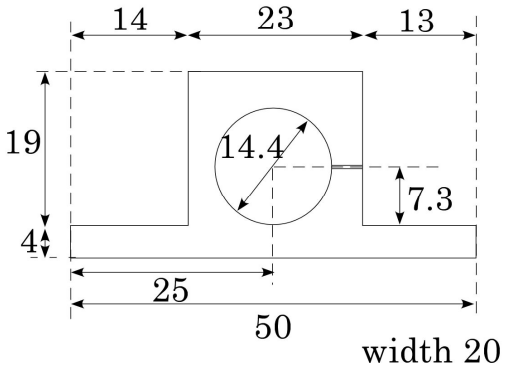

Pedestal

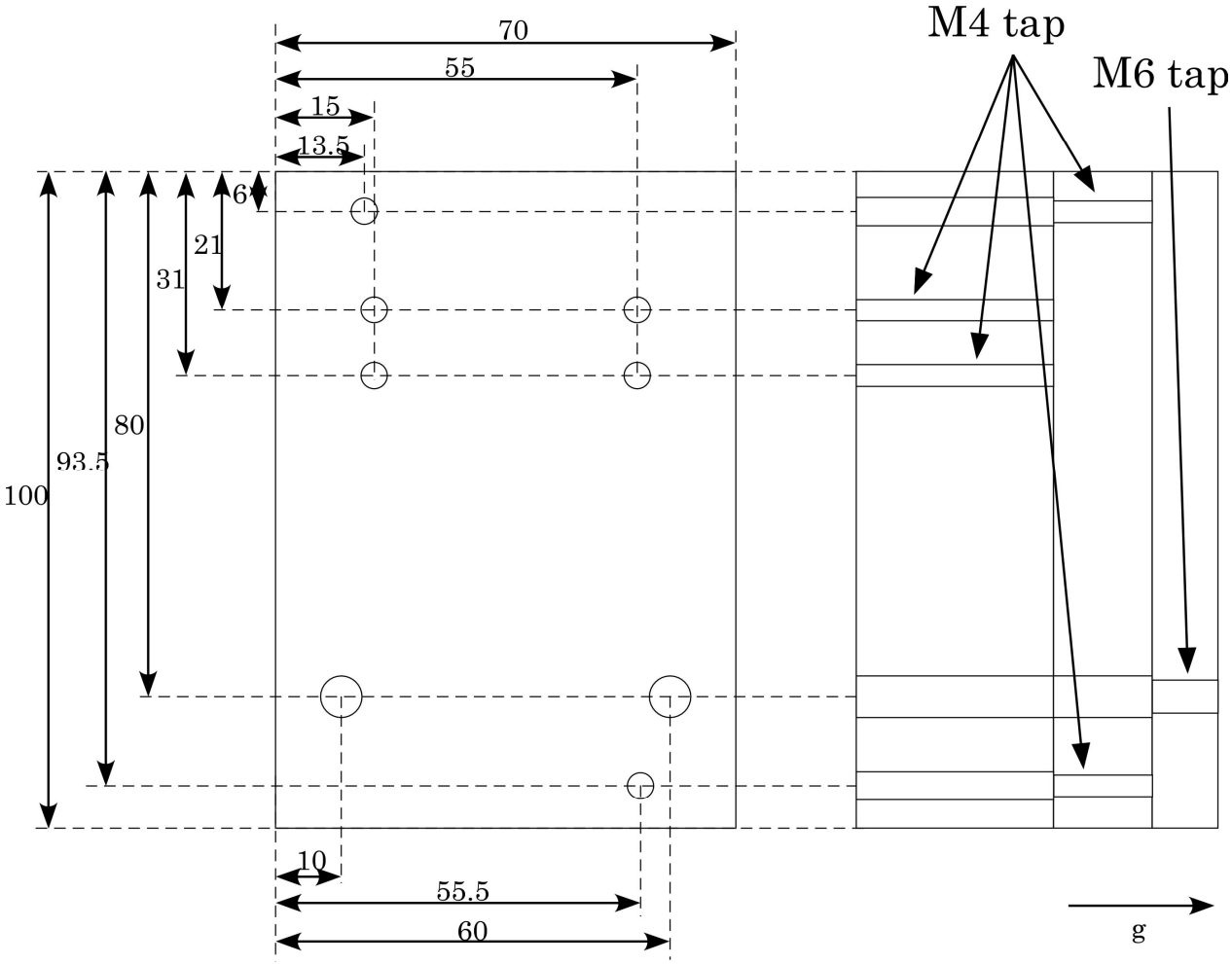

Appendix E Design of tapered amplifier

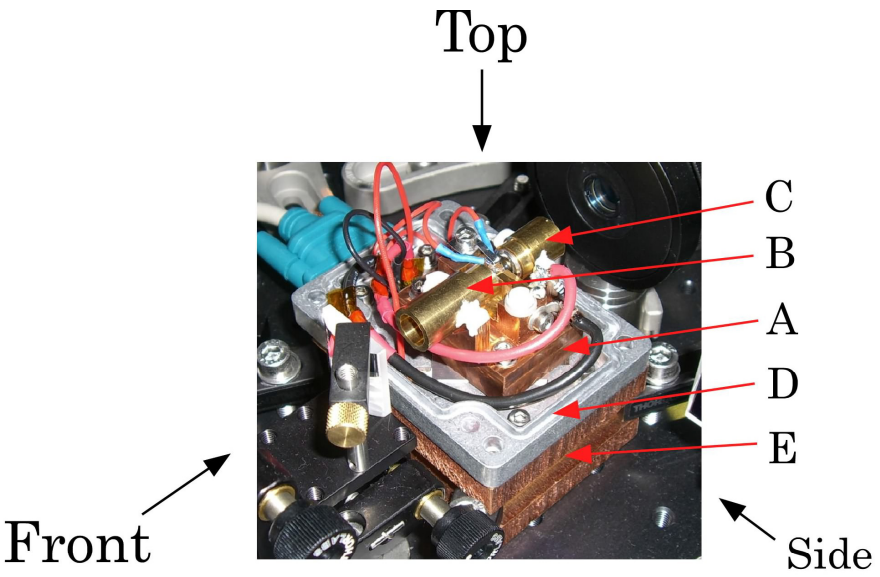

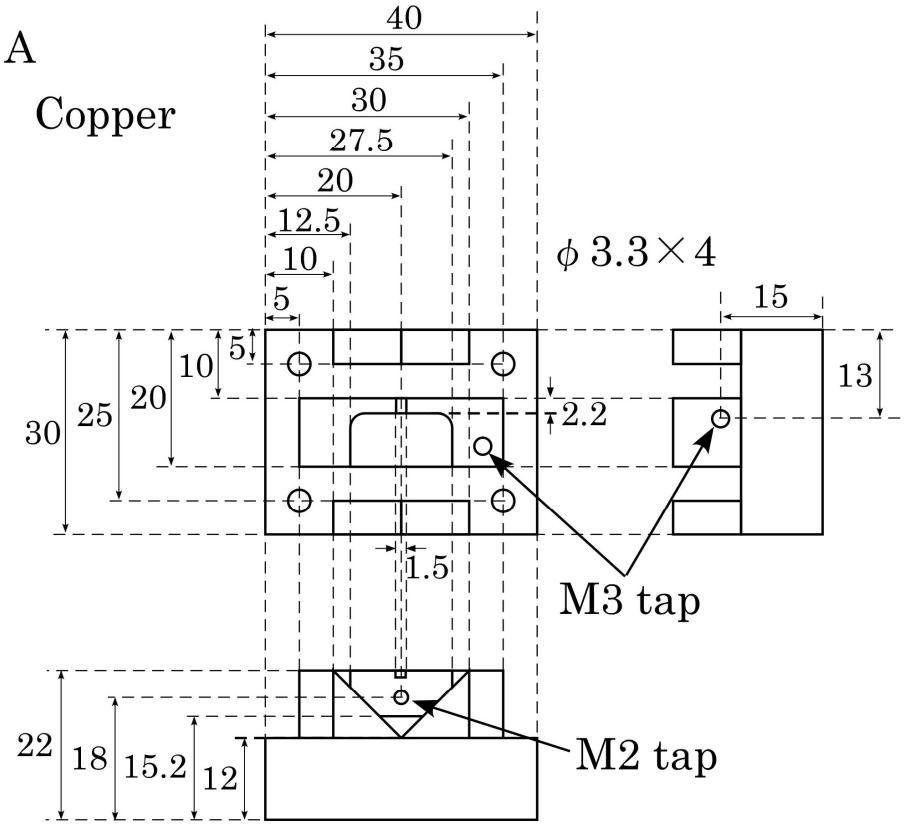

B

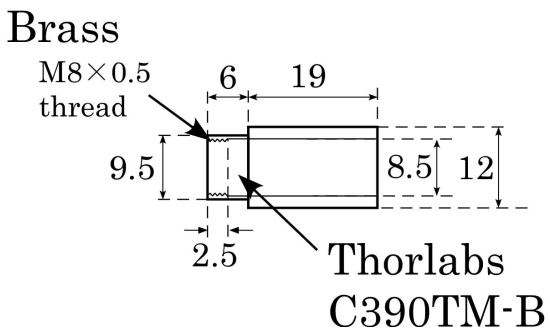

C

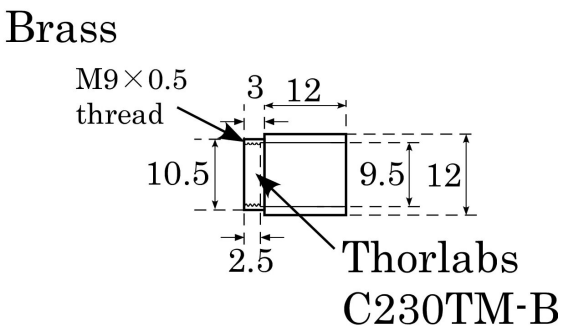

D

Takachi
BDN6-8-5N

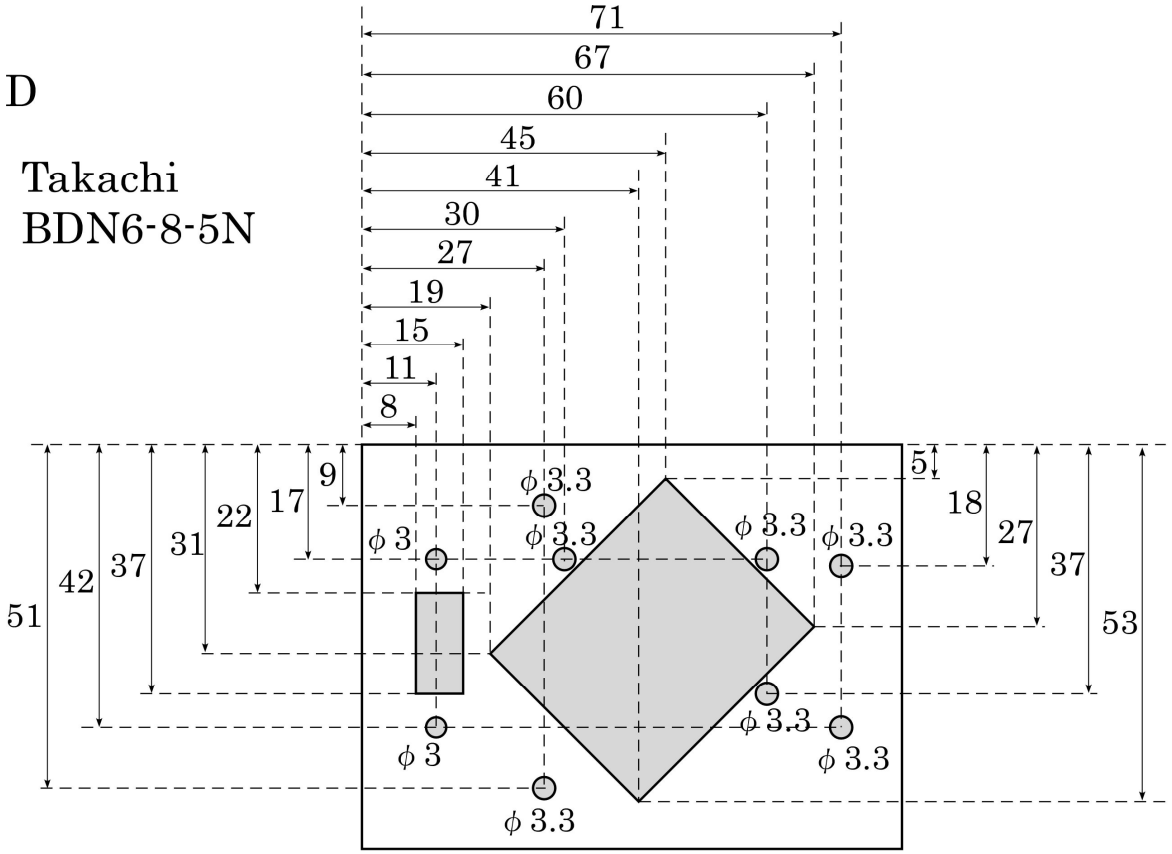

E

Copper

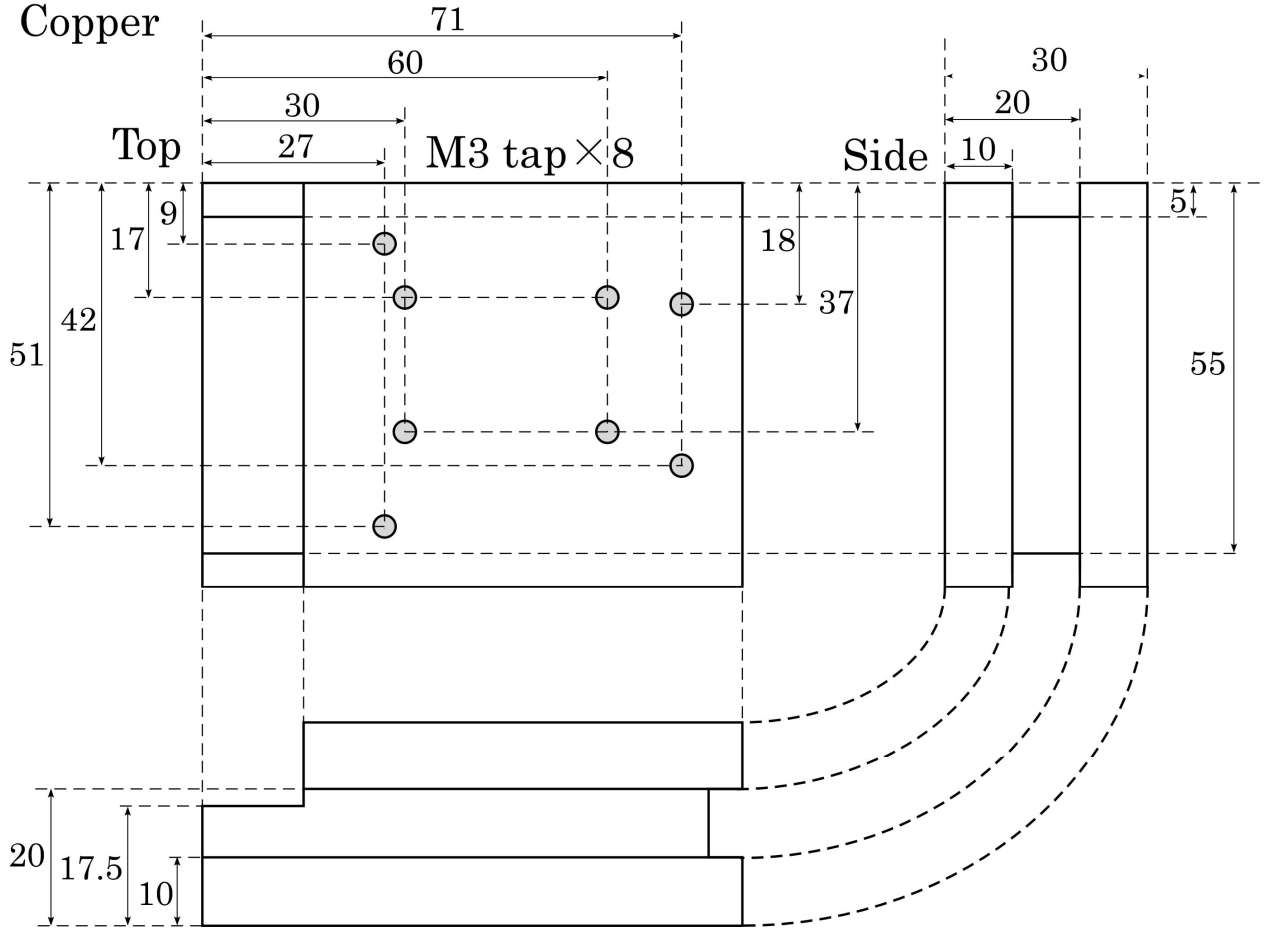

Appendix F　Matlab code for the 6 level model

Each code should be saved as an M-file. The values of *R*, *CE*, *f_lens*, *d_lens* and *distance* depend on an experimental condition. The code for ^{41}K differs from that for ^{39}K only in the detuning of each transition.

(a) ^{39}K

```
function y=slevel39(It,Ir,d1,d2,pdvoltage)
% about potassium39
hv=1.617                              % energy of one photon in eV
Is=1.77                               % saturation intensity in mW/cm2
gamma=6.09                            % natural linewidth in MHz/2pi
% about photodetector
R=200000                              % resistor of the photodetector in ohm
CE=0.42                               % conversion efficiency in A/W
Current=pdvoltage/(1000*R)            % current flowed from PD in A
Nphoton=Current*10^19/(CE*hv*1.6)     % observed number of photons in /s
% experimental configuration
i1=6*It/0.70882               % intensity of a trap beam measured by Thorlabs Power Meter in mW/cm2
i2=6*Ir/0.70882               % intensity of a trap beam measured by Thorlabs Power Meter in mW/cm2
det1=(d1-103.9)*2
det2=(116.1-d2)*2
f_lens=40                             % focal length of the lens
d_lens=25.4                           % diameter of the lens
distance=100                          % distance between the lens and the MOT
separation=(distance*f_lens)/(distance-f_lens)    % distance between the lens and the PD
tanc=(d_lens/2)/separation            % tangent of the angle
omega=(1-1/sqrt(1+tanc^2))/2          % solid angle
cell_loss=0.04                        % loss on the surface of the cell (1 path)
% atom number in 6 level model
b=[1 5/6 1/2 0;0 1/6 1/2 1]           % branching ratio matrix
c=[1/3 1 5/3 7/3;1/5 3/5 1 7/5]/3     % oscillator strength of the S1/2->P3/2 transition
Int=0
Int=[i2 i2 i2 0;0 i1 i1 i1]/Is        % intensity matrix
Det=0
Det=2*[det2-12.5 det2-9.3 det2 0;0 det1-30.3 det1-21.0 det1]/gamma % detuning matrix
R=0
R=(pi*gamma*10^6)*(b.*c).*(Int./(1+(Det.^2)))   % exitation-rate matrix
s1=0
s2=0
for F=1:4                             % sum over upper hyperfine states
    s1=s1+(R(2,F)+2*pi*gamma*10^6*b(2,F))*R(1,F)/(R(1,F)+R(2,F)+2*pi*gamma*10^6)
    s2=s2+(R(1,F)+2*pi*gamma*10^6*b(1,F))*R(2,F)/(R(1,F)+R(2,F)+2*pi*gamma*10^6)
end
p2ovp1=s1/s2                          % population ratio of the ground states
spFovp1=0
```

```
for F=1:4                              % sum over upper hyperfine states
    spFovp1=spFovp1+(R(1,F)+R(2,F)*p2ovp1)/(R(1,F)+R(2,F)+2*pi*gamma*10^6)
end
Pe=spFovp1/(1+p2ovp1+spFovp1)          % excited-state fraction
y=Nphoton/(2*pi*gamma*10^6*Pe*omega*(1-cell_loss)^2)  % number of atoms
```

(b) ^{41}K

```
function y=slevel41(It,Ir,d1,d2,pdvoltage)
% about potassium41
hv=1.617                               % energy of one photon in eV
Is=1.77                                % saturation intensity in mW/cm2
gamma=6.09                             % natural linewidth in MHz/2pi
% about photodetector
R=200000                               % resistor of the photodetector in ohm
CE=0.42                                % conversion efficiency in A/W
Current=pdvoltage/(1000*R)             % current flowed from PD in A
Nphoton=Current*10^19/(CE*hv*1.6)      % observed number of photons in /s
% experimental configuration
i1=6*It/0.70882                % intensity of a trap beam measured by Thorlabs Power Meter in mW/cm2
i2=6*Ir/0.70882                % intensity of a trap beam measured by Thorlabs Power Meter in mW/cm2
det1=(89.8-d1)*2
det2=(210.1-d2)*2
f_lens=50                              % focal length of the lens
d_lens=25.4                            % diameter of the lens
distance=75                            % distance between the lens and the PD
separation=(distance*f_lens)/(distance-f_lens)   % distance between the lens and the MOT
tanc=tan((d_lens/2)/separation)        % tangent of the angle
omega=(1-1/sqrt(1+tanc^2))/2           % solid angle
cell_loss=0.04                         % loss on the surface of the cell (1 path)
% atom number in 6 level model
b=[1 5/6 1/2 0;0 1/6 1/2 1]            % branching ratio matrix
c=[1/3 1 5/3 7/3;1/5 3/5 1 7/5]/3      % oscillator strength of the S1/2->P3/2 transition
Int=0
Int=[i2 i2 i2 0;0 i1 i1 i1]/Is         % intensity matrix
Det=0
Det=2*[det2-3.5 det2-3.4 det2 0;0 det1-17 det1-13.6 det1]/gamma % detuning matrix
R=0
R=(pi*gamma*10^6)*(b.*c).*(Int./(1+(Det.^2)))  % exitation-rate matrix
s1=0
s2=0
for F=1:4                              % sum over upper hyperfine states
    s1=s1+(R(2,F)+2*pi*gamma*10^6*b(2,F))*R(1,F)/(R(1,F)+R(2,F)+2*pi*gamma*10^6)
    s2=s2+(R(1,F)+2*pi*gamma*10^6*b(1,F))*R(2,F)/(R(1,F)+R(2,F)+2*pi*gamma*10^6)
end
p2ovp1=s1/s2                           % population ratio of the ground states
```

```
spFovp1=0
for F=1:4                              % sum over upper hyperfine states
    spFovp1=spFovp1+(R(1,F)+R(2,F)*p2ovp1)/(R(1,F)+R(2,F)+2*pi*gamma*10^6)
end
Pe=spFovp1/(1+p2ovp1+spFovp1)          % excited-state fraction
y=Nphoton/(2*pi*gamma*10^6*Pe*omega*(1-cell_loss)^2)  % number of atoms
```

Appendix G Properties of Potassium

(a) Vapor pressure

The vapor pressure $P_{vap}$of potassium at a temperature T is expressed as

$$P_{vap} = 760 \times 10^{A+B/T} \tag{G.1}$$

where A = 4.961 and B = -4646 for potassium [130]. Figure G.1 shows the formula (G.1).

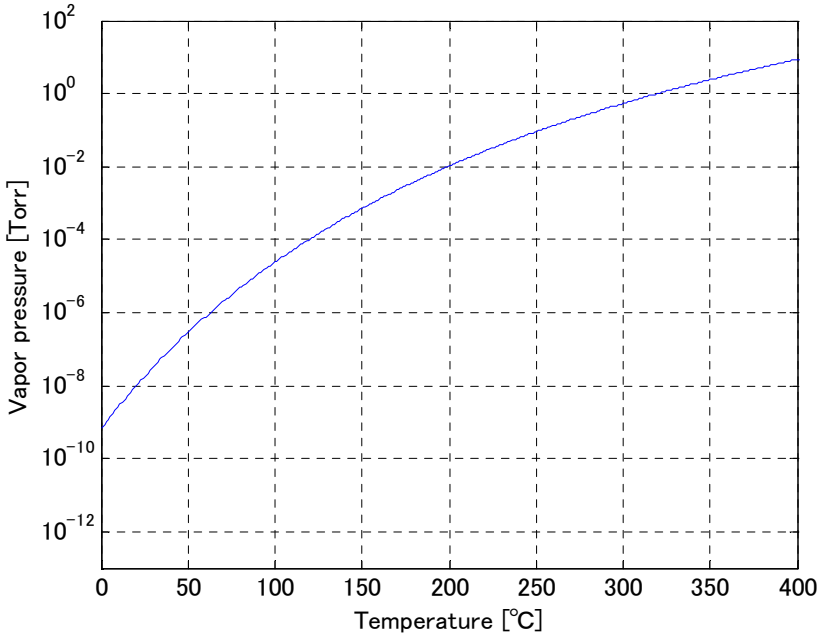

Fig G.1 Vapor pressure of potassium

(b) Fundamental physical properties

Table G.1 Fundamental Physical Properties of Potassium

Atomic number	Z	19	
Total Nucleons	$Z+N$	39, 40, 41	
Relative Natural Abundance	η	93.2581(44)% (39), 0.0117(1)% (40), 6.7302(44)% (41)	[130]
Nuclear Lifetime	τ_n	stable (39, 41), 1.26×10^{9} yr (40)	[130]
Atomic mass	m	38.9637069(3) u (39) 39.96399867(29) u (40) 40.96182597(28) u (41)	[130]
Density at 20℃	ρ_m	0.862 g/cm^3	[130]
Melting point	T_M	63.38 ℃	[130]
Boiling point	T_B	759 ℃	[130]
Specific Heat Capacity	c_p	0.757 J/g K	[130]
Molar Heat Capacity	C_p	29.600 J/mol K	[130]
Vapor pressure at 25℃	P_v	2×10^{-8} Torr	[130]
Nuclear Spin	I	3/2 (39, 41), 4(40)	
Ionization limit	E_I	35009.8140cm^{-1}	[131]

(c) Optical properties

Table G.2 Potassium D_2 ($4^2S_{1/2} \rightarrow 4^2P_{3/2}$) Transition Optical Properties

Frequency	ω_0	2π ・391.01617003(12) THz (39) 2π ・391.016296050(88) THz (40) 2π ・391.01640621(12) THz (41)	[132]
Wavelength (Vacuum)	λ	766.70092180(24) nm (39) 766.70067470(17) nm (40) 766.70045870(24) nm (41)	
Lifetime	τ	26.34(5) ns	[133]
Natural Line Width	Γ	2π ・6.042(11) MHz	
Recoil temperature	T_r	836.117 nK (39) 815.190 nK (40) 795.332 nK (41)	
Doppler shift (v = 1m/s)	$\Delta\omega_d$	2π ・1.30429 MHz	
Doppler Temperature	T_D	145 μ K	

Table G.2 Potassium D_1 ($4^2S_{1/2} \rightarrow 4^2P_{1/2}$) Transition Optical Properties

Frequency	ω_0	2π ・389.286058716(62) THz (39) 2π ・389.286184353(73) THz (40) 2π ・389.286294205(62) THz (41)	[132]
Wavelength (Vacuum)	λ	770.108385049(123) nm (39) 770.108136363(144) nm (40) 770.107919192(123) nm (41)	
Lifetime	τ	26.69(5) ns	[133]
Natural Line Width	Γ	2π ・5.963(11) MHz	
Recoil temperature	T_r	828.734 nK (39) 807.992 nK (40) 788.310 nK (41)	
Doppler shift (v = 1m/s)	$\Delta\omega_d$	2π ・1.29852 MHz	

(d) Hyperfine constants

Table G.3 Potassium D Transition Hyperfine Structure Constants

Magnetic Dipole Constant	$4^2S_{1/2}$	$A\ ^2S_{1/2}$	461.720 MHz (39) -1285.79 MHz (40) 254.014 MHz (41)	[134]
Magnetic Dipole Constant	$4^2P_{1/2}$	$A\ ^2P_{1/2}$	27.775(42) MHz (39) -34.523(25) MHz (40) 15.245(42) MHz (41)	[132]
Magnetic Dipole Constant	$4^2P_{3/2}$	$A\ ^2P_{3/2}$	6.093(25) MHz (39) -7.585(10) MHz (40) 3.363(25) MHz (41)	[132]
Magnetic Dipole Constant	$4^2P_{3/2}$	$B\ ^2P_{3/2}$	2.786(71) MHz (39) -3.445(90) MHz (40) 3.351(71) MHz (41)	[132]

Bibliography

[1] M.H.Anderson *et al.*, Science **269**, 198(1995)
[2] C.C.Bradley *et al.*, Phys.Rev.Lett. **75**, 1687(1995)
[3] K.B.Davis *et al.*, Phys.Rev.Lett. **75**, 3969(1995)
[4] M.Greiner *et al.*, Nature **415**, 39(2002)
[5] C.A.Regal *et al.*, Phys.Rev.Lett. **92**, 040403(2004)
[6] V.S.Letokhov *et al.*, JETP Lett. **7**, 272(1968)
[7] C.Salomon *et al.*, Phys.Rev.Lett. **59**, 1659(1987)
[8] H.Feshbach *et al.*, Ann.Phys. **19**, 287(1962)
[9] E.Tiesinga *et al.*, Phys.Rev.A **46**, R1167(1992)
[10] E.Tiesinga *et al.*, Phys.Rev.A **47**, 4114(1993)
[11] A.J.Moerdijk *et al.*, Phys.Rev.A **51**, 4852(1995)
[12] J.M.Vogels *et al.*, Phys.Rev.A **56**, R1067(1997)
[13] H.M.J.M.Boesten *et al.*, Phys.Rev.A **54**, R3726(1996)
[14] S.Inouye *et al.*, Nature **392**, 151(1998)
[15] P.Courteille *et al.*, Phys.Rev.Lett. **81**, 69(1998)
[16] J.L.Roberts *et al.*, Phys.Rev.Lett. **81**, 5109(1998)
[17] S.Giorgini *et al.*, cond-mat/0706.3360 (2007)
[18] I.Bloch *et al.*, cond-mat/0704.3011(2007)
[19] K.Goral *et al.*, Phys.Rev.Lett. **88**, 170406(2002)
[20] H.P.Buchler *et al.*, Phys.Rev.Lett. **98**, 060404(2007)
[21] D.J.Heinzen *et al.*, Phys.Rev.Lett. **84**, 5029(2000)
[22] M.G.Kozlov *et al.*, J.Phys.B **28**, 1933(1995)
[23] D.DeMille, Phys.Rev.Lett. **88**, 067901(2002)
[24] A.Kantrowitz *et al.*, Rev.Sci.Instr. **22**, 328(1951)
[25] R.E.Smalley *et al.*, J.Chem.Phys. **61**, 4363(1974)
[26] H.LBethlem *et al.*, Nature **406**, 491(2000)
[27] J.van Veldhoven *et al.*, Phys.Rev.Lett. **94**, 083001(2005)
[28] J.D.Weinstein *et al.*, Nature **395**, 148(1998)
[29] S.Kotochigova *et al.*, Phys.Rev.A **68**, 022501(2003)
[30] J.M.Sage *et al.*, Phys.Rev.Lett. **94**, 203001(2005)
[31] A.Fioretti *et al.*, Phys.Rev.Lett. **80**, 4402(1998)
[32] J.P.Shaffer *et al.*, Phys.Rev.Lett. **82**, 1124(1999)
[33] C.Haimberger *et al.*, Phys.Rev.A **70**, 021402(R) (2004)
[34] A.N.Nikolov *et al.*, Phys.Rev.Lett. **82**, 703(1999)
[35] Gabbanini *et al.*, Phys.Rev.Lett. **84**, 2814(2000)
[36] R.Wynar *et al.*, Science **287,** 1016(2000)
[37] E.Donley *et al.*, Nature **417**, 529(2002)
[38] F.K.Fatemi *et al.*, Phys.Rev.A **66**, 053401(2002)
[39] K.Strecker *et al.*, Phys.Rev.Lett. **91**, 080406(2003)
[40] C.A.Regal *et al.*, Nature **424**, 47(2003)
[41] J.Herbig *et al.*, Science **301**, 1510(2003)
[42] K.Xu *et al.*, Phys.Rev.Lett. **91**, 210402(2003)
[43] M.W.Mancini *et al.*, Phys.Rev.Lett. **92**, 133203(2004)

[44] A.J.Kerman *et al.*, Phys.Rev.Lett. **92**, 153001(2004)
[45] C.Chin *et al.*, Phys.Rev.Lett. **94**, 123201(2004)
[46] S.D.Kraft *et al.*, J.Phys.B. **39**, S993(2006)
[47] C.Ospelkaus *et al.*, Phys.Rev.Lett. **97**, 120402(2006)
[48] J.J.Zirbel *et al.*, cond-mat/0712.3889(2007)
[49] F.Ferlaino *et al.*, Phys.Rev.A **73**, 040702(R)(2006)
[50] A.Pashov *et al.*, Phys.Rev.A **76**, 022511(2007)
[51] G.Modugno *et al.*, Phys.Rev.Lett. **89**, 190404(2002)
[52] W.C.Stwalley *et al.*, J.Chem.Phys. 108, 5767(1998)
[53] C.Klempt *et al.*, Phys.Rev.A **76**, 020701(2007)
[54] R.S.Williamson *et al.*, J.Opt.Soc.Am.B 12, 1393(1995)
[55] F.S.Cataliotti *et al.*, Phys.Rev.A **57**, 1136(1998)
[56] D.Wang *et al.*, Phys.Rev.A **53**, R1216(1996)
[57] W.Ketterle *et al.*, Phys.Rev.Lett. **70**, 2253(1993)
[58] M.H.Anderson *et al.*, Phys.Rev.A **50**, R3597(1994)
[59] C.Townsend *et al.*, Phys.Rev.A **53**, 1702(1996)
[60] W.Petrich *et al.*, J.Opt.Soc.Am.B, **11**, 1332(1994)
[61] M.Prevedelli *et al.*, Phys.Rev.A **59**, 886(1999)
[62] C.Fort *et al.*, Eur.Phys.J D **3**, 113(1998)
[63] H.J.Metcalf *et al.*, *Laser cooling and trapping*, Springer(1999)
[64] Gordon *et al.*, Phys.Rev.A **21**, 1606(1980)
[65] R.J.Le Roy *et al.*, J.Mol.Struc.(Theochem), **591**, 175(2002)
[66] J.A.Coxon *et al.*, J.Mol.Spectr., **235**, 235(2005)
[67] M.Marinescu *et al.*, Phys.Rev.A **49**, 982(1994)
[68] M.Marinescu *et al.*, Phys.Rev.A **52**, 311(1995)
[69] M.Marinescu *et al.*, Zeitschrift fur Physik D **36**, 239(1996)
[70] S.H.Patil *et al.*, J.Chem.Phys. **106**, 2301(1997)
[71] A.Derevianko *et al.*, Phys.Rev.Lett. **82**, 3589(1999)
[72] M.Marinescu *et al.*, Phys.Rev.A **59**, 390(1999)
[73] A.Derevianko *et al.*, Phys.Rev.A **63**, 052704(2001)
[74] S.G.Porsev *et al.*, J.Chem.Phys. **119**, 844(2003)
[75] B.M.Smirnov *et al.*, JETP **21**, 624(1965)
[76] G.Hadinger *et al.*, J.Mol.Spectr. **175**, 441(1996)
[77] D.Zemke *et al.*, J.Chem.Phys. **111**, 4962(1999)
[78] J.Y.Seto, University of Waterloo, Master thesis(2000), available at http://etd.uwaterloo.ca/jyseto2000.pdf
[79] R.Rydberg, Z.Physik **73**, 376(1931)
[80] O.Klein, Z.Physik **76**, 226(1932)
[81] R.Rydberg, Z.Physik **80**, 514(1933)
[82] A.L.G.Rees, Proc.Phys.Soc.(London) **59**, 998(1947)
[83] R.J.Le Roy, *A Computer Program Implementing the First-Order RKR Method for Determining Diatom Potential Energy Curves from Spectroscopic Constants*, University of Waterloo Chemical Physics Research Report CP-425 (1992); available at http://leroy.uwaterloo.ca/programs/.
[84] R.J.Le Roy *et al.*, Chem.Phys.Lett., **5**,42(1970)
[85] R.J.Le Roy *et al.*, J.Chem.Phys., **52**, 3869(1970)
[86] C.R. Vidal *et al.*, J.Mol.Spectr. **65**, 46(1977)

[87] MOLPRO, a package of ab initio programs designed by H.-J.Werner and P.J.Knowles, version 2002.1, R.D.Amos, A.Bernhardsson, A.Berning, P.Celani, D.L.Cooper, M.J.O.Deegan, A.J.Dobbyn, F.Eckert, C.Hampel, G.Hetzer, P.J.Knowles, T.Korona, R.Lindh, A.W.Lloyd, S.J.McNicholas, F.R.Manby, W.Meyer, M.E.Mura, A.Nicklass, P.Palmieri, R.Pitzer, G.Rauhut, M.Schutz, U.Schumann, H.Stoll, A.J.Stone, R.Tarroni, T.Thorsteinsson and H.-J.Werner.

[88] G.Herzberg, *Molecular spectra and molecular structure 1.spectra of diatomic molecules*, Krieger Publishing Company, Malabar, Florida(1950)

[89] T.Bergeman *et al.*, J.Chem.Phys. **117**, 7491(2002)

[90] D.R.Hartree, Rep.Prog.Phys. **11**, 113(1946)

[91] M.R.Manaa, Int.J.Quant.Chem. **75**, 693(1999)

[92] V.Kokoouline *et al.*, Phys.Rev.A **62**, 032716(2000)

[93] R.Ferber *et al.*, J.Chem.Phys. **112**, 5740(2000)

[94] M.Tamanis *et al.*, J.Chem.Phys. **117**, 7980(2002)

[95] M.R.Manaa *et al.*, J.Chem.Phys. **117**, 11208(2002)

[96] T.Bergeman *et al.*, Phys.Rev.A **67**, R050501(2003)

[97] T.Bergeman *et al.*, Eur.Phys.J. D **31**, 179(2004)

[98] P.Qui *et al.*, J.Chem.Phys. **127**, 044301(2007)

[99] H.Lefebvre-Brion, *Perturbations in the Spectra of Diatomic Molecules* (Academic, New York, 1986)

[100] R.J.Le Roy, LEVEL 8.0: *A Computer Program for Solving the Radial Schrodinger Equation for Bound and Quasibound Levels*, University of Waterloo Chemical Physics Research Report CP-663 (2007); available at http://leroy.uwaterloo.ca/programs/.

[101] R.J.Le Roy, LEVEL 7.7: *A Computer Program for Solving the Radial Schrodinger Equation for Bound and Quasibound Levels*, University of Waterloo Chemical Physics Research Report CP-663 (2001);

[102] F.Martin *et al.*, J.Chem.Phys. **115**, 4118(2001)

[103] W.Jastrzebski *et al.*, J.Mol.Spectr. **209**, 50(2001)

[104] A.Pashov *et al.*, Chem.Phys.Lett. **292**, 615(1998)

[105] A.Grochola *et al.*, Chem.Phys.Lett. **372**, 173(2003)

[106] W.C.Stwalley, Eur.Phys.J. D **31**, 221(2004)

[107] S.Rousseau *et al.*, J.Mol.Spec. **203**, 235(2000)

[108] C.E.Wiemann *et al.*, Rev.Sci.Instr., **62**, 1(1991)

[109] K.B.MacAdam *et al.*, Am.J.Phys., **60**, 1098(1992)

[110] A.S.Arnold *et al.*, Rev.Sci.Instr., **69**, 1236(1998)

[111] R.Drever *et al.*, Appl.Phys.B **31**, 97 (1983)

[112] B.DeMarco *et al.*, Rev.Sci.Instr., **70**, 1967(1999)

[113] R.S.Williamson, Ph.D. thesis (1997)

[114] *MCP Assembly Technical Notes* (Japanese), Hamamatsu Photonics K.K., Shizuoka, 2006

[115] E.Flaxer, Meas.Sci.Technol. **17**, N37(2006)

[116] L.G.Marcassa *et al.*, Phys.Rev.A **63**, 013413(2000)

[117] J.Emsler, *The Elements, Oxford Chemistry Guides* (Oxford Univ. Press, New York, NY, 1995)

[118] A.Fioretti *et al.*, Eur.Phys.J. D **15**, 189(2001)

[119] R.S.Freeland, Ph.D. thesis, The University of Texas at Austin (2001), available at http://www.ph.utexas.edu/~coldatom/pubs.html

[120] A.R.L.Caires *et al.*, Phys.Rev.A **71**, 043403(2005)

[121] J.Lozeille *et al.*, Eur.Phys.J. D **39**, 261(2006)

[122] A.Fioretti *et al.*, J.Phys.B. **40**, 3283(2007)

[123] D.Wang *et al.*, a Eur.Phys.J. D **31**, 165(2004)
[124] D.Wang *et al.*, Phys.Rev.Lett. **93**, 243005(2004)
[125] D.Wang *et al.*, Phys.Rev.A **72**, 032502(2005)
[126] G.Pichler *et al.*, J.Phys.B **16**, 4619(1983)
[127] R.Beuc *et al.*, J.Phys.B **17**, 739(1984)
[128] A.Jraij *et al.*, Chem.Phys. **290**, 129(2003)
[129] M.Korek *et al.*, Int.J.Quantum Chemistry **92**, 376(2003)
[130] David R.Lide (Ed.), *CRC Handbook of Chemistry and Physics*, 83rd ed. (CRC Press, Boca Raton, 2002)
[131] J.Sugar and C.Corliss, J.Phys.Chem.Ref.Data **14**, Suppl. 2(1985)
[132] S.Falke *et al.*, Phys.Rev.A **74**, 032503(2006)
[133] H.Wang *et al.*, Phys.Rev.A **55**, R1569(1997)
[134] E.Arimondo, M.Inguscio and P.Violino, Rev.Mod.Phys. **49**, 31(1977)